Electricity yield simulation of complex BIPV systems

Proefschrift

ter verkrijging van de graad van doctor
aan de Technische Universiteit Delft,
op gezag van de Rector Magnificus prof. ir. K. C. A. M. Luyben,
voorzitter van het College voor Promoties,
in het openbaar te verdedigen op donderdag 10 oktober 2013 om 12:30 uur
door

Wendelin SPRENGER
Magister rerum naturalium, Universiteit Innsbruck (Oostenrijk)
geboren te Hall i.T., Oostenrijk

Dit proefschrift is goedgekeurd door de promotor:
Prof. dr. ir. M. Zeman

Copromotor Dr. rer. nat. H.R. Wilson

Samenstelling promotiecommissie:

Rector Magnificus	voorzitter
Prof. dr. ir. M. Zeman	Technische Universiteit Delft, promotor
Dr. rer. nat. H. R. Wilson	Fraunhofer ISE, Germany, copromotor
Prof. Dr. R. Schindler	Fraunhofer ISE, Germany
Prof. A. Wagner	Karlsruhe Institute of Technology, Germany
Prof. dr. eng. J.A. Ferreira	Technische Universiteit Delft
Dr. R.A.C.M.M. van Swaaij	Technische Universiteit Delft
Prof. dr. ir. A. van Timmeren	Technische Universiteit Delft

Wendelin Sprenger
Electricity yield simulation of complex BIPV systems
Ph.D. thesis, Delft University of Technology, with summary in Dutch

Published and distributed by: Wendelin Sprenger
E-mail: wendelin.sprenger@ise.fraunhofer.de

Bibliographic information published by Die Deutsche Nationalbibliothek
Die Deutsche Bibliothek lists this publication in the Deutsche Nationalbibliografie; detailed bibliografic data is available in the Internet at <http://dnb.d-nb.de>.
ISBN: 978-3-8396-0606-3

Nobelstrasse 12, D-70504 Stuttgart
URL: http://verlag.fraunhofer.de

Chi disputa allegando l'alturità, non adopra lo 'ngegno,
ma più tosto la memoria.
Leonardo da Vinci, 1452-1519

Abstract

Although the research field of building-integrated photovoltaics (BIPV) has been growing fast during the last 10 years, no validated simulation program to calculate the BIPV electricity yield has been developed yet. Until now, commercially available computer programs to calculate the electricity yield have focused on free-standing PV plants; the extent to which the models applied by the programs, especially for the irradiance and the temperature simulation, can be extended to BIPV has not been investigated on a systematic basis yet. The present thesis fills this gap, including the analysis of complex, multifunctional BIPV elements.

To analyze the contribution of reflections from other buildings or the ground to the irradiance on a PV module, a ray-tracing procedure has been implemented. With this procedure, a common approach to consider the diffuse part of the irradiance on free-standing plants is validated for vertical module surfaces. For complex BIPV modules, the ray-tracing procedure has been extended to the optical simulation of the interior structure of the module. Furthermore, as the reflectivity of the PV module increases with larger incidence angles of the radiation, the impact of the larger proportion of radiation corresponding to large incidence angles for vertically installed PV modules has been analyzed.

Compared to existing commercial PV electricity yield simulation programs, the analysis of the PV cell temperature has been extended. Due to the complex layer composition of BIPV modules, such as those functioning as insulating glass units, the standard techniques (considering the three temperature transfer mechanisms heat conductance, radiation and convection) commonly applied for architectural glazing have been implemented. The approach offers the possibility to analyze the impact of wind speed on the electricity yield or to compare different module layer compositions. For BIPV systems consisting of solar cells of wafer-based technologies, the behavior at low light intensities and the temperature coefficients are simulated with the two-diode model. A simulation program for semiconductor devices, called ASA, has been applied to demonstrate that the results of the two-diode model are not valid for amorphous silicon solar cells, even when the effects of light soaking and annealing are neglected.

Because of its specific importance for BIPV, detailed investigations of the simulation of shading losses have been undertaken. Cell I–V characteristics have been determined for negative and positive values of the voltage and current. The DC power of the BIPV system is calculated by adding either the currents or the voltages of the calculated cell I–V characteristics and the blocking or bypass diodes, according to the circuit diagram. The resulting system I–V curve has to be calculated for every time step. The progress in calculation speed of computers now allows this calculation in a reasonable time scale.

The results of applying the methodology that has been developed in this PhD thesis are presented on the module as well as the system level. The possibilities for

quantitative dimensioning of bypass and blocking diodes to protect the PV cells from being heated up have been analyzed. Furthermore, the dependence of the I–V curve of a complex BIPV module on the incidence angle has been validated.

A roof-top PV system in Bad Krozingen that consists of PV modules based on monocrystalline silicon allowed a detailed validation of the shading simulation. The agreement of the simulated and measured time-dependent DC power was excellent, resulting in an R^2 of 97.98%. The statistical measures applied within this PhD thesis are defined in appendix A. A more complicated shading structure has been analyzed for a saw-tooth roof BIPV system, which was also monitored for many years. Although the PV modules that are based on polycrystalline silicon showed a relatively high variation in the STC module I–V characteristics, the agreement between the simulated and measured system DC power still reached an R^2 of 93.55%. With a third PV system, based on a-Si:H solar cells, the effects of light soaking and annealing have been quantified by comparing the measurement of the system DC power with the results of the simulation. A fourth, building-applied PV system was used to analyze electrical mismatch when vertically installed PV modules of different orientations are connected. Finally, the simulation of the inverter efficiency according to different versions of the Schmidt-Sauer model shows nearly perfect agreement with the measurement results, including the losses due to a restricted voltage range, for all monitored inverters that have been analyzed.

Samenvatting

Hoewel het onderzoek op het gebied van “building-integrated photovoltaics” (BIPV) sterk gegroeid is in de afgelopen 10 jaar, is er nog geen gevalideerd simulatieprogramma ontwikkeld waarmee de BIPV electriciteitsopbrengst kan worden uitgerekend. Tot nu toe hebben commercieel beschikbare computerprogramma’s waarmee de electriciteitsopbrengst kan worden uitgerekend zich gericht op losstaande PV installaties; de mate waarin de modellen die worden gebruikt door de programma’s, in het bijzonder voor de instraling- en temperatuursimulatie, kunnen worden uitgebreid naar BIPV is nog niet op een systematische manier bestudeerd. Dit proefschrift vult dit gat, inclusief de analyse van complexe, multifunctionele BIPV elementen.

Een “ray-tracing” procedure is geïmplementeerd om de bijdrage van reflecties van andere gebouwen of de grond aan de instraling van een PV module te analyseren. Met deze procedure wordt een gebruikelijke benadering waarin het diffuse deel van de instraling van op zichzelf staande PV installaties wordt beschouwd gevalideerd voor verticale moduleoppervlakken. Voor complexe BIPV modules is de ray-tracing procedure uitgebreid naar de optische simulatie van de interne structuur van de module. Verder is het effect bestudeerd van het grotere deel van de straling overeenkomstig met grotere hoeken van inval voor verticaal geïnstalleerde PV modules wanneer de reflectiviteit van de PV module toeneemt met grotere hoeken van inval van de straling.

Vergeleken met bestaande commerciële simulatieprogramma’s voor de electriciteitsopbrengst is de analyse van de PV celtemperatuur uitgebreid. Door de complexe laagsamenstelling van BIPV modules, zoals diegenen die functioneren als isolerende glaseenheden, zijn de standaardtechnieken geïmplementeerd die normaal worden toegepast in architectonische beglazing (waarbij de drie temperatuuroverdrachtsmechanismes warmtegeleiding, straling en convectie in beschouwing worden genomen). De benadering biedt de mogelijkheid om het effect van windsnelheid op de electriciteitsopbrengst te analyseren of om verschillende laagsamenstellingen in de module te vergelijken. Voor BIPV systemen bestaande uit zonnecellen van wafergebaseerde technologieën zijn het gedrag bij lage lichtintensiteiten en de temperatuurcoëfficiënten gesimuleerd met het twee-diode model. Een simulatieprogramma voor halfgeleiderdevices, ASA geheten, is gebruikt om te demonstreren dat de resultaten van het twee-diode model niet geldig zijn voor amorf silicium zonnecellen, zelfs niet wanneer de effecten van “light soaking” en “annealing” worden verwaarloosd.

Vanwege het specifieke belang voor BIPV is een gedetailleerde studie van de simulaties van schaduwverliezen uitgevoerd. I–V karakteristieken van de cel zijn bepaald voor positieve en negatieve waardes van de spanning en stroom. Het DC vermogen van het BIPV systeem is uitgerekend door ofwel de stromen danwel de spanningen van de uitgerekende I–V karakteristieken en de blocking- of bypassdiodes bij elkaar op te tellen volgens het circuitdiagram. De resulterende systeem I–V curve

moet voor iedere tijdsstap worden uitgerekend. De vooruitgang in rekensnelheid van computers tegenwoordig maakt het mogelijk om deze berekening binnen een redelijk tijdsbestek uit te voeren. De resultaten van het toepassen van de methodologie die is ontwikkeld in dit proefschrift worden gepresenteerd op zowel module- als op systeemniveau. De mogelijkheden voor het kwantitatief dimensioneren van bypass- en blockingdiodes om de PV cellen te beschermen tegen verwarming zijn geanalyseerd. Verder is de afhankelijkheid van de I–V curve van een complexe BIPV module van de hoek van inval gevalideerd.

Een PV systeem geïnstalleerd op een dak in Bad Krozingen dat bestaat uit PV modules gebaseerd op monokristallijn silicium maakte een gedetailleerde validatie van de schaduwsimulatie mogelijk. De overeenkomst tussen het gesimuleerde en gemeten tijdsafhankelijke DC vermogen was uitstekend, resulterend in een R^2 van 97.98%. De statistische maten gebruikt in dit proefschrift worden gedefinieerd in appendix A. Een meer ingewikkelde schaduwstructuur is geanalyseerd voor een BIPV systeem op een zaagtanddak dat gedurende vele jaren is gemonitord. Hoewel de PV modules die zijn gebaseerd op polykristallijn silicium een relatief grote variatie in de STC module I–V karakteristieken vertonen, bereikte de overeenkomst tussen het gesimuleerde en gemeten DC systeemvermogen nog altijd een R^2 van 93.55%. Met een derde PV systeem, gebaseerd op a-Si:H zonnecellen, zijn de effecten van light soaking en annealing gekwantificeerd door de meting van het DC systeemvermogen te vergelijken met de resultaten van de simulatie. Een vierde op een gebouw geïnstalleerd PV systeem is gebruikt om de elektrische mismatch te analyseren wanneer verticaal geïnstalleerde PV modules van verschillende oriëntaties verbonden zijn. Ten slotte laat de simulatie van de invertereﬃciëntie volgens verschillende versies van het Schmidt-Sauermodel een nagenoeg perfecte overeenkomst met de meetresultaten zien, inclusief de verliezen veroorzaakt door een beperkt voltagebereik, voor alle gemonitorde inverters die bestudeerd zijn.

Contents

1 Introduction

1.1 Motivation

Since the beginning of photovoltaic (PV) module production, the advantages of installing modules on buildings have been recognized: the electricity is generated near the consumer loads, and no additional land has to be occupied. However, PV systems that are simply installed on the roof of a building cannot be considered to be building-integrated. Following the most common definition, building-integrated photovoltaics (BIPV) denotes photovoltaic systems that fulfill at least one additional building-related function besides generating electricity. The function may be: thermal insulation, glare protection, noise control or weather protection, among others.

The scientific field of BIPV has grown rapidly during the last decade. Besides the Solar Decathlon that has taken place every year since 2002, the largest PV conferences have increased the emphasis on the topic BIPV. In recent years, the topic has gained considerable importance due to the enactment of the Energy Performance of Buildings Directive (EPBD) by the European Commission in 2010. The directive named 2010/31/EU can be found in [8]. In Article 9.1, the directive demands:

Member States shall ensure that:
(a) by 31 December 2020, all new buildings are nearly zero-energy buildings; and
(b) after 31 December 2018, new buildings occupied and owned by public authorities are nearly zero-energy buildings.

This demand requires that every new building constructed after 2020 has to generate nearly as much primary energy as it consumes. The problem of electricity storage is explicitly excluded from the scope of the directive; the term "zero-energy building" requires per definition only that the total amount of primary energy supplied by the building (from regenerative sources) has to "nearly" equal the total consumed primary energy, including the heating or cooling demands of the building, over a specified period of time, usually the full year. Besides the challenge of reducing or even eliminating the energy demand for cooling or heating, it will be necessary to extend the location for electricity generation from the roof to the building façade to achieve a sufficiently high electricity yield to meet the demands of the building.

Despite this trend to BIPV, the approaches to simulate the electricity yield of free-standing PV systems have not been extended to BIPV applications on a systematic basis; this applies especially to the simulation of the irradiance on vertical PV modules, the PV cell temperature and the behavior of complex BIPV elements. This

PhD thesis fills this gap by analyzing the statistical relevance of various topics, such as the angular and spectral response of the PV modules, the impact of the PV module layer structure to the cell temperature or the importance of the cell I–V curve at negative voltages for simulating the DC power at partial shading.

Particularly in façade applications, the irradiation of the photovoltaic cells of BIPV systems depends on the surroundings. Reflections from the ground or white walls of surrounding buildings as well as shading objects influence the irradiance on the PV cells and play an important role for the electricity yield. One illustrative example is shown in Figs. 4.41 and 4.42 (pp. 118 and 119). For this reason, the surroundings are taken into account in the simulations with the help of ray-tracing calculations. Also the temperature of the PV cells in a BIPV element has to be considered. Façade elements may have the function of thermal insulation; if they consist of photovoltaic components, these may have a higher temperature than free-standing plants due to the poorer heat transfer to the inside of the building. In addition, and most importantly, the inhomogeneous irradiance on the BIPV cells and modules has rather complicated consequences for the electricity yield of the system. None of the discussed topics is new; however, to the author's knowledge, they have never been combined to an electricity yield simulation tool before. The system evaluation under shading conditions needs a considerable amount of calculation time; without the development in computer speed during the last decade, the simulations within this thesis could not have been performed. The behavior of the PV modules at large incidence angles of the irradiance is the next topic; above 60° incidence angle, the reflection losses become significant.

The development of a simulation program requires its validation. At the Fraunhofer Institute for Solar Energy Systems, some BIPV systems have been monitored over many years; the largest and most notable BIPV system, constituting the saw-tooth roof of a prominent institute building, has been simulated within this thesis and used for validation purposes. Furthermore, the validation of the electricity yield simulation under shading conditions was performed using data from a PV system in Bad Krozingen near Freiburg, monitored by another department at the institute. In addition, data from a monitored PV system of amorphous silicon modules near Dresden has been used for validation.

The product development of the BIPV element PVShade®, presented in the next section, was carried out before the time of my thesis within the EU-funded "Cost-Effective" project; prototypes were presented within the PhD thesis of Francesco Frontini [15]. Although two such BIPV systems were installed during 2012, the analyses within this thesis had to be constrained to laboratory measurements of such elements. Nevertheless, interpretation of this geometrically complex BIPV component is also part of the PhD thesis.

1.2 Complex BIPV modules

One goal suggested by the clear targets of the European Builidings Directive is the development of façade-optimized BIPV elements. The optimisation does not have to be restricted primarily to the annual electricity yield but can also focus on the reduction of the building energy demand, comfort, aesthetics, etc. In this respect, there are various optimisation possibilities. For example, the façade element described in the next subsection, although stationary, ensures that the average solar gains through it are lower in summer than in winter. A “complex” BIPV façade element has an interior structure that demands a more detailed optical or thermal simulation compared to standard PV elements. Regarding such complex BIPV modules as depicted in Fig. 1.1 and 1.3, the electricity yield simulation should be able to reproduce the physical effects involved, like the calculation of the optical paths inside the complex BIPV module or the simulation of the PV cell temperatures. For some BIPV façades, reflective surfaces play a role; others may display interference effects, especially if thin-film PV technology is involved. As a first example, the multifunctional BIPV façade element published by Francesco Frontini is presented in the following section.

1.2.1 The angle-selective façade element PVShade®

The PVShade® module has been developed within the European project “Cost-Effective” (subtitle: Convert façades into multifunctional, energy gaining components) [9]. A photograph of a prototype is shown in Fig. 1.1; the 3D structure of the PVShade® module is illustrated in Fig. 2.6 (p. 37).

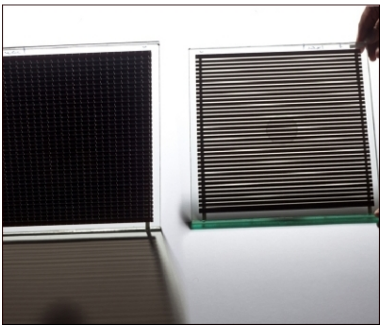

Figure 1.1: Photographs of the outdoor surface of a PVShade® test module. The transmission of the radiation is dependent on the position of the sun (or, in general, the light source).

This BIPV element consists of two thin-film PV modules that have been made semi-transparent by laser-ablating stripes of the photovoltaic layers in the direction corresponding to the series connection of the PV cells. Depending on the laser wavelength, the front transparent conductive oxide (TCO) layer of the thin-film assembly can be removed or not, which has consequences for the electrical connection and the visual performance. After producing two striped modules, the thin-film PV modules are laminated to each other, with the stripes of the two PV modules slightly juxtaposed.

The procedure leads to a dependence of the transmittance not only on the incidence angle, but also on the zenith angle of the sun. Façade elements with this property can be called “angle-selective”. Besides generating electricity, a PVShade® module transmits less solar energy during the summer than during the winter because the direct sunlight near midday is blocked mainly during the summer months. Therefore, it helps to lower the energy-related costs of a building caused by the heating and cooling demand. Furthermore, the BIPV element allows a good view of the surroundings from the inside. The analysis of the solar heat gain coefficient (g-value), which is dependent on the sun’s position, has been published by Francesco Frontini in 2011, including a presentation of possible options for building integration and a building energy simulation [16]. One of the possible applications of the PVShade® module is shown in Fig. 1.2.

Figure 1.2: Daylight simulation of an airport hall with the PVShade® modules installed in the façade. Source: [15]

For the electricity yield simulation of this BIPV system, there are some important questions to be answered. The light path through the interior structure of the modules has to be analyzed; furthermore, it is not easy to decide whether the TCO layer should be removed with the other PV thin-film layers or not. Next, the optimal wiring configuration of the PV modules to each other has to be found. A temperature simulation of the BIPV modules has to be made, not only for the electricity yield calculation, but also to assess thermal stress on the component. Also, maybe more than one MPP tracker is needed when the front and the back PV module of all PVShade® modules of a BIPV system are connected in series. To answer these questions, a detailed analysis is necessary. In order to answer these questions, a

BIPV electricity yield simulation program is needed which is able to deal with such complex BIPV systems.

1.2.2 Other complex BIPV façade elements

An increasing number of companies offer BIPV products with an internal structure that requires a ray-tracing procedure for an electricity yield simulation. Two typical BIPV modules are presented within this section. The Israeli company SolarOr offers a product called SolarOr BeeHive PV façade that consists of glass prisms that refract the light such that electricity is generated by the monocrystalline PV cells, but the view from the inside of the building to the outside is still possible. According to the data sheet, these SolarOr modules have a maximum power per m^2 of 155 W while offering a visible light transmittance of 40%. Furthermore, glare on the outside is avoided due to retro-reflecting the direct sunlight back in the direction of the sun. Furthermore, the façade element has an excellent heat transfer coefficient (U-value) of 0.2–0.35 W/(m^2K).

A similar product is offered by the American company Guardian; the façade element is called Guardian SunGuard PVGU. This facade element also works with total reflection; the PV cells are mounted horizontally, allowing a good view to the outside similar to the SolarOr façade product. According to the data sheet, the maximum power per m^2 is 120 W, with a light transmittance of 49%. The heat transfer coefficient (U-value) is 0.27 W/(m^2K).

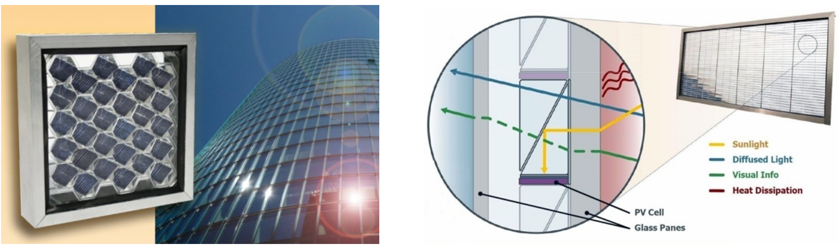

Figure 1.3: Commercially available complex BIPV façade elements. Left: SolarOr BeeHive PV façade, right: Guardian SunGuard PVGU [59, 21]

Both products, depicted in Fig. 1.3, are commercially available. This PhD thesis offers a methodology to calculate the electricity yield of BIPV systems made of these façade elements, which would also include the possibility of optimisation.

1.3 The challenge of optimizing the PV cell and module connection

In every PV system, the PV cells and modules have to be connected in series or parallel. Cable losses are minimized by a large number of series connections; parallel connections can reduce the losses due to shading or due to different PV module orientations. If an inverter is installed, its voltage range has to be considered. In free-standing plants, a good configuration for connecting the PV modules is easy to identify. For BIPV systems, the building defines the frequency of shading situations as well as the orientation of the PV modules; both aspects make the decision more difficult.

Figure 1.4: The fire station of Houten/Utrecht as an example for different module orientations as a consequence of building integration [51].

Different PV module orientations as well as shading conditions can lead to different irradiation of cells that are electrically connected. The rather complicated consequences on the electricity yield for both situations can be calculated by analyzing the I–V curve of every PV cell separately. This offers the possibility of optimizing the connection plan for BIPV systems according to the highest electricity yield. Furthermore, the electricity gained by choosing the optimal connection plan can be calculated.

1.4 Objective of this thesis

An increasing number of high-rise buildings is equipped with BIPV systems in their façades, and even complex BIPV modules as those presented in subsection 1.2.2 are already available for purchase. However, today's electricity yield simulation programs still use models that are adapted for free-standing PV plants. No validated PV simulation program exists to calculate the electricity yield of building-integrated PV systems. For this reason, architects or builders are not able to calculate the annual energy accurately that is generated by a planned or already existing BIPV system.

This lack of knowledge does not only handicap the decision process for installing a BIPV system, it also makes research on the optimization of BIPV systems very difficult.

The objective of this thesis is to develop a simulation procedure for the electricity yield simulation of BIPV systems. First, the physical quantities and principles that are decisive for it are summarized; then, their impact on the electricity yield is quantified. Before this PhD thesis was published, it was unclear whether reflections from surrounding objects play a significant role for the electricity yield. Also the importance of the angular response of a PV module was unknown for the annual electricity yield, especially if the PV module is vertically installed. And the question remained unanswered whether vertically oriented PV modules of different cardinal directions can be connected in parallel and be handled by one single inverter without a major loss due to electrical mismatch.

For BIPV systems, inhomogeneous irradiation on the PV system is an important and frequent issue, for partial shading as well as for PV systems with differently oriented PV modules. For a detailed simulation of the electricity yield of BIPV systems, the consequences of inhomogeneous irradiation have to be analyzed in detail, which will also offer the possibility of optimizing the interconnection of the PV cells and modules. Within this PhD thesis, the simulation of the electricity yield under partial shading conditions is especially brought into focus. To conclude, the aim of this PhD thesis is to develop and validate a simulation procedure to calculate the electricity yield of arbitrary building-integrated PV systems, which has been achieved.

1.5 Outline of the PhD thesis

The first chapter of the PhD thesis gives an introduction to building-integrated photovoltaic systems. After a short general motivation for developing a procedure for the simulation of the electricity yield of BIPV systems, some already existing complex BIPV modules are presented. The challenge of optimizing the electrical interconnection of the PV cells and modules is stressed, which is an important topic for BIPV, due to PV modules of different orientation as well as partial shading.

Chapter 2 focuses on the physical principles that are important for an electricity yield simulation and discusses different approaches for the simulation of the irradiance on the PV cells, the temperature of the PV cells, the electrical properties of the PV cells, their interconnection and the inverter. The aim is to give an overview of the most common simulation approaches for every part of the calculation of the electricity yield of building-integrated photovoltaic systems.

Chapter 3 describes the external programs that have been applied for the simulations within this PhD thesis. The program RADIANCE is applied for all ray-tracing analyses of geometrical configurations, while the program ASA has been applied to calculate the cell I–V curves of PV cells based on amorphous silicon at different irradiances and temperatures, which allows a comparison to the results of the calculation of the cell I–V curves based on equivalent circuits. All the other simulations, following the models and procedures described in chapter 2, have been performed with programs that have been developed during the PhD thesis.

Chapter 4 includes all simulation results and validations that have been performed; this chapter is the core of the PhD thesis. The quantitative analysis of the agreement between simulation and measurement, independent of the physical quantity, is carried out with the statistical measures defined in Appendix A. The measures allow the rating of the quality of different simulation approaches as well as the rating of the physical principles which should be considered in the simulation. Section 4.2 includes the validation of the simulation of irradiance on tilted surfaces, the analysis of the irradiance fraction due to ground albedo, the comparison of the ray-tracing approach with the common method of analyzing the shading course, the analysis of the applicability of the sky discretisation procedure for PV electricity yield simulations, and the incidence angle dependence of the irradiance on PV modules of vertical orientations. In section 4.3, the calculation of the I–V characteristics of an amorphous silicon PV cell applying the two-diode model is compared to the results of the ASA program. Section 4.4 analyzes the operation points of shaded multicrystalline PV cells in a PV module as installed in the saw-tooth roof PV system of Fraunhofer ISE as well as for an amorphous silicon PV module, as installed in the free-standing PV system in Mochau/Dresden. In the same section, the results of performing I–V curve measurements of a PVSHADE® sample at various incidence angles are presented and compared to simulation results. In section 4.5, the electricity yield simulation is finally applied to four different (BI)PV systems. The validation of the electricity yield simulation of a partially shaded PV system is performed with the PV roof system in Bad Krozingen, which consists of PV modules based on monocrystalline silicon and has a very simple shadow pattern. The electricity yield simulation for a BIPV system with a highly complex shading structure has been performed with the saw-tooth roof BIPV system of the Fraunhofer ISE main building, where also the detailed simulation of the cell temperature was applied. The consequences of light soaking and annealing on the PV electricity yield for PV modules based on amorphous silicon is analyzed with the free-standing PV system in Mochau/Dresden. The fourth monitored PV system is installed in Ichtershausen and is made of PV modules based on the a-Si/μ-Si tandem PV technology. For this PV system, the electricity yield of a parallel connection of different vertical orientations of PV modules is simulated.

1.6 Novel contributions to the field

The combination of the ray-tracing procedure with the interconnection of cell I–V curves was already suggested in 1995 by Anne Kovach [31]. However, mainly due to the calculation speed of computers, the simulation program of 1995 was restricted to very symmetric shadow patterns, and the simulation was restricted to the MPP of the system I–V curve, excluding the inverter. Due to the lack of monitored BIPV systems at that time, the simulation program of 1995 remained unvalidated.

Within this PhD thesis, a new simulation approach based on the same idea, but with a detailed temperature simulation of the PV cells, a detailed analysis of the angular response of the (BI)PV modules and a detailed inverter analysis has been developed and compared to the measurement data of monitored PV systems, including the BIPV system in the saw-tooth roof of the Fraunhofer ISE main building. The simulation approach combines various research fields that have already been separately investigated in detail. However, several investigations important for the simulation of the PV electricity yield have been made and are presented in this PhD thesis. With the help of the ray-tracing technique, the consequences of the reflections from surrounding objects on the electricity yield of vertically installed BIPV systems have been quantified (subsection 4.2.3). It has been shown that the 60° approach for the irradiance simulation, described in subsection 2.4.3, is also valid for vertical orientations of irradiance sensors (subsection 4.2.5). Applying the method of separating the sky simulation from the simulation of the geometrical configuration of the surroundings, described in subsection 2.2.5 and commonly applied for daylight simulation of buildings, has clear disadvantages for BIPV systems, as shown in subsection 4.2.4.

As the simulation allows the time-dependent electricity yield to be calculated, statistical measures are defined that allow the agreement between measurement and simulation to be quantified for all time-dependent physical quantities that are relevant for the electricity yield simulation. The clear definition of the statistical measures, as carried out in App. A, allows comparison of the results within this PhD thesis with other simulation programs that can calculate the time-dependent electricity yield. For the PV roof system in Bad Krozingen, an agreement of the electricity yield simulation with the measured DC power of $R^2 = 97.03\%$ is reached for the unshaded PV subsystem, while the measurement of the DC power of the partially shaded PV subsystem shows an agreement of $R^2 = 97.98\%$ (see subsection 4.5.1). The electricity yield simulation for the saw-tooth roof BIPV system of the Fraunhofer ISE main building leads to an agreement of the simulation results with the measured DC power of $R^2 = 93.55\%$, despite the significant variation of the STC I–V curves of the PV modules. With the third monitored PV system, the thin-film PV system in Mochau/Dresden, the seasonal metastability effect of PV modules based on amorphous silicon was quantified on a daily basis, and a simple fitting function was suggested that allows future comparisons of PV systems based on thin-film PV technologies to each other. With the fourth PV system, at Ichtershausen/Erfurt, the DC power loss due to a parallel connection of PV modules of different vertical orientations based on the a-Si/μ-Si tandem technology was quantified (see subsection 4.5.4), which can also be considered to be a novel contribution to the field of BIPV electricity yield simulation.

2 Methods to simulate the electricity yield

2.1 Overview

The simulation of the electricity yield of a BIPV system requires the combination of several physical subdisciplines. Primarily, the electrical behavior of a PV cell, which is reflected in the I–V curve, depends on the irradiance and the temperature; therefore, a detailed simulation of the irradiance incident on every photovoltaic cell of the BIPV system and a simulation of the PV cell temperatures has to be performed. As the BIPV system consists of several PV cells that, in general, operate under different conditions, and as bypass and blocking diodes which can improve the power of the BIPV system may also be integrated, the BIPV system has to be treated as an electrical DC circuit. Finally, an inverter identifies the operation point of maximum system power and converts the DC power into AC power.

It has been discovered during the work of this PhD thesis that, for the general case of BIPV electricity yield simulations, a combination of ray tracing and simulation of the cell I–V curves over the whole voltage range is necessary. Fig. 2.1 gives an overview of the "methodology" to calculate the BIPV electricity yield that has been applied in this PhD thesis.

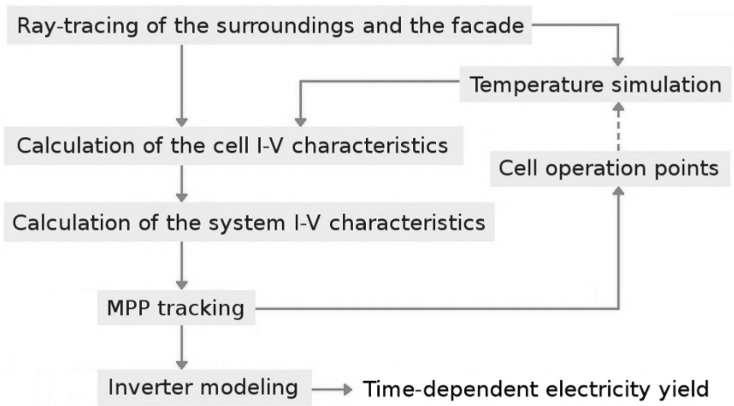

Figure 2.1: Overview of the methodology to calculate the time-dependent electricity yield of a BIPV system. For complex BIPV modules like PVShade®, the ray-tracing procedure is extended to the interior structure of the module. The need for the loop in the simulation chain (dashed line) is discussed in subsection 4.4.1.

First, the irradiance on the BIPV system has to be simulated. In general, there are shading objects in the surroundings. Then, the photovoltaic device has to be optically simulated, not only to determine the angular dependence of reflectance, but also and especially to analyze the optical performance of complex BIPV modules. The electrical behavior of the PV system cannot be predicted without a simulation of the temperature of the PV cell. However, depending on the cell interconnection, also the cell operation points on the I–V curve may influence the temperature. The calculation of the operation points is also interesting to determine the number of bypass and blocking diodes needed. Then, the resulting system I–V characteristic is MPP-tracked by the inverter; after the simulation of the inverter efficiency, the time-dependent AC electricity yield of the BIPV system can be calculated.

This chapter summarizes the decisive physical effects that determine the performance of the BIPV system as well as the methods that may be applied for a BIPV electricity yield simulation. The first subchapter discusses the simulation of the incident irradiation on the PV modules; then, in the next subchapter, spectral issues are discussed that are relevant for the BIPV electricity yield; after that, the optical simulation of the PV module's layer composition and related topics are described. Subchapter 2.5 summarizes the calculation of the cell and module I–V characteristics, that are treated as DC elements of the entire PV system in subchapter 2.6. The next subchapter describes the simulation of the PV cell temperature at operating conditions; after a short discussion of the effects of light soaking and annealing on the DC system power, an analysis of the inverter behavior is presented in subchapter 2.9.

This chapter is restricted to description of the physical effects that influence the DC system power; the discussion of topics that require detailed simulations, including the analysis of relevance of a physical effect to the generated power, is deferred until chapter 4.

2.2 Simulation of the incident radiation

As the energy source for a PV cell is the light incident on its surface, the basis for simulating the electricity yield of a photovoltaic system is the time-dependent calculation of the number of photons reaching the photovoltaic layers, including the spectral distribution of these photons. At first, the definitions of the basic radiometric quantities have to be given.

2.2.1 Radiometric quantitities

Light consists of small particles of electromagnetic radiation, called photons. For photovoltaic applications, the whole energy range of terrestrial solar radiation from approx. 0.5 to 4.4 eV can play a role; even if the photons cannot contribute to the electricity production, their absorption in any layer of the photovoltaic cell still may lead to a temperature increase of it. The photon energy only depends on its frequency ν. As a consequence, the energy of an electromagnetic spectrum depends on the number of photons per frequency:

$$E_{spec} = h \int_0^{\infty} \frac{dN}{d\nu} \cdot \nu \, d\nu \tag{2.1}$$

N is the number of photons with a frequency in $[\nu, \nu + d\nu]$, h the Planck constant and E_{spec} the spectral energy. The radiant flux Φ is defined as the energy of an electromagnetic spectrum per time unit.

$$\Phi = \frac{d}{dt} E_{spec} \tag{2.2}$$

In general, when a PV module is irradiated, the photons come from different directions, usually from the full hemisphere in front of the PV module. The angle of incidence of a photon, expressed in spherical coordinates, is called θ_M, with normal incidence being defined by $\theta_M = 0$. ϕ_M is the azimuth in the module reference system, as depicted in Fig. 2.2.

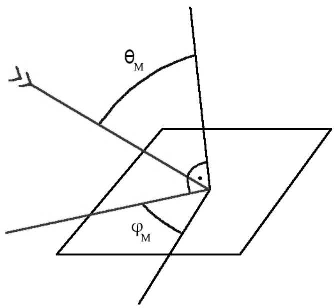

Figure 2.2: The definition of the angles θ_M and ϕ_M of the module reference system. θ_M is the incidence angle, with normal incidence being defined by $\theta_M = 0$. ϕ_M, the azimuth in the module reference system, is zero if the projection of the incident ray onto the PV module surface coincides with the orientation of the PV module.

Based on the two angles in the module reference system, the following two radiometric quantities of major importance can be defined:

$$L = \frac{\partial}{\partial \Omega} \frac{\partial \Phi}{\partial A} \cdot \frac{1}{\cos \theta_M} \tag{2.3}$$

$$E = \int_0^{2\pi} \int_0^{\pi/2} L \cos \theta_M \, \sin \theta_M d\theta_M d\phi_M = \int_{\Omega} L \cos \theta_M \, d\Omega \tag{2.4}$$

with A being the surface area and Ω the solid angle taken into account for observation. Formula 2.3 defines the radiance L, while the irradiance E[1] is defined in Eq. 2.4.

These two are the most important radiometric[2] quantities and will be used throughout this thesis. Obviously, the two quantities have different physical units, namely $W/m^2/sr$ and W/m^2, respectively. L gives information about the total power observed or emitted in the solid angle Ω, while E integrates the observed, seldom emitted, power over the whole hemisphere.[3] When the spectral mismatch is considered (see subsection 2.3.2), pyranometer or silicon sensor measurements can be compared to E for validation purposes. For the prediction of the number of photons absorbed in the absorber layers of a PV cell, the incident angle distribution and therefore L is the relevant quantity.

2.2.2 Meteorological data

The accuracy of the simulation of the incident radiation on the PV modules strongly depends on the available type of weather data. For the purpose of validating the steps of the simulation summarized in Fig. 2.1, the irradiance measurements need to have high time resolution. The analysis of the time-resolved impact of partial shading on the DC power, the analysis of the significance of the PV module's heat capacity and many more phenomena cannot be analyzed if the time resolution of the irradiance measurements is too low. For most PV systems and locations, however, measurement data of the irradiance is not available in that detail. Within this subsection, the possible types of available data sets are presented, for which an electricity yield simulation is still possible, but not at the same level of accuracy. As a first distinction between the different types of available irradiance data, it is important to know whether the irradiance values are

- mean values for one year based on results for several years (like the METEONORM [37] or TRY[4] database)
- values for a specific year:
  - satellite data as a basis for the irradiance values, simulated with models (examples are Satel-Light [52] or GeoModel [17])

[1] Energy as well as irradiance are commonly abbreviated to E. However, the meaning should be clear from the context.

[2] A physical unit is called "radiometric" if the distinction from a "photometric" unit needs to be made. "Photometric" units describe the perception of light by the human eye and will not be needed here.

[3] For the more general process of photons being emitted or photons incident on a surface, the terms "radiation" and "irradiation" are applied. If a time period is specified (e.g. annual), the term "irradiation" will also be used for "irradiative energy per square meter in the specified time period".

[4] Test reference years, available in many countries. For Germany, the test reference years can be ordered from DWD (Deutscher Wetterdienst).

– measured values at the location of the BIPV system

In addition, the types of measured (or simulated) irradiances are important. Within this PhD thesis, the irradiance fraction coming directly from the sun is called "direct irradiance", the other fraction is called "diffuse irradiance". Both irradiance fractions together are called "total irradiance"; when the detection surface is oriented horizontally, this irradiance is also called "global irradiance" because the radiation of the whole sky hemisphere contributes to the irradiance. Again, several types of measurement data are available:

- Only the total irradiance on the module plane (common for most monitored PV systems)
- Two of the following three values:
  – Global irradiance on a horizontal plane
  – Diffuse irradiance on a horizontal plane
  – Direct-normal irradiance
- Only the global irradiance on a horizontal plane

These quantities can be measured either with a pyranometer or a silicon sensor. Their different spectral and angular responses offer different opportunities in the simulation: The pyranometer makes the comparison to STC measurements more accurate, while the silicon sensor is only sensitive for a limited part of the spectrum, as depicted in Fig. 2.4. However, for a wavelength-independent calculation of the power absorbed in the photovoltaic cells, the irradiance values measured by a silicon sensor may be more appropriate. See section 2.3.

The next important criterion for the data basis that defines the possible accuracy of the electricity yield simulation is:

- Time steps of the measurements (hourly, minutely,... values)

In some cases, also time series for the following data may be available:

- Spectral distribution for:
  – Direct irradiance on a horizontal plane
  – Global irradiance on a horizontal plane

The global irradiance can be measured with a pyranometer, while the direct irradiance is frequently calculated by taking the difference of the global and the diffuse irradiance. The latter is measured by a pyranometer with a shadow ring. Its size also defines the terms "direct" and "diffuse" irradiance. An alternative method to measure direct irradiance is to use a pyrheliometer, which tracks the sun.

For the prediction of the PV or BIPV system electricity yield without any irradiance measurements performed on-site, there is no other possibility than to assume a global and diffuse irradiance data set corresponding to the average of previous years. Due to the variation of the irradiance over the years, however, this means that the simulation results of the electricity yield have a far higher uncertainty for predictions than if the evaluation can be performed with already existing meteorological data for comparison to simultaneously measured system performance. Some of the effects presented in this thesis such as the dependence of the inverter on the DC voltage or the dependence of the angular response function on the PV module type may be neglected in the simulation to predict an electricity yield if the uncertainty due to the simulation of the irradiance on a tilted plane is already that high.

Various models have been developed to convert irradiance values to other ones. For example, to simulate irradiance values at shorter time intervals, for example five-minute values from hourly irradiance data, the method of Skartveit-Olseth has been established [57]. Calculating the diffuse-horizontal irradiance fraction from the global irradiance can be performed e.g. with the Erbs model [12]. The most important step in calculating the electricity yield for a non-horizontal (BI)PV system is the calculation of the irradiance on a tilted plane from the global and diffuse irradiance values on a horizontal plane, which will be discussed below.

2.2.3 Simulation of the irradiance on a tilted surface from radiometric measurements on the horizontal plane

For the prediction of the irradiance on tilted surfaces, many models have been developed in the past; today's standard procedure can e.g. be read in [11]. An old, but clearly presented overview of models was published by John Hay in 1985 [23]. The best-known historical models are the one of Liu and Jordan, published in 1963 [35], and the model of Klein and Theilacker from 1981 [30].

In more recent years, the calculation of the irradiance on a tilted plane was augmented by the simulation of the sky radiance distribution. Amongst many other scientists, R. Perez, who also worked on the irradiance simulation on tilted surfaces [41], developed a sky model which could be applied in ray-tracing programs that had been developed at that time. In all the irradiance simulations reported in this thesis, a ray-tracing procedure was applied.

Models for the sky radiance distribution

Also for the simulation of the sky radiance distribution at every time step, many models have been developed until now. A comparison and summary of the best-known models were written in 2004 by Igawa et al. [25]. Comparisons between the Brunger [7] and the Perez models [40] were also made in the diploma thesis of Ralf Preu [43]. As the Perez model is often considered to be the most accurate one, it will be summarized briefly. Originally, the Perez sky model gave a description of the sky luminance distribution. However, it turned out to be also applicable for radiometric values. According to Perez, the radiance relative to the zenith radiance can be simulated by Eq. 2.5.

$$L(\theta,\phi)/L_Z = (1 + a\exp[b/\cos\theta])(1 + c\exp[d\phi] + e\cos^2\phi) \tag{2.5}$$

θ and ϕ are the zenith angle and the azimuth, defining the southern direction to be zero, and the western orientation to have positive values. The parameters a to e can be determined by fitting the irradiance values on a horizontal plane at a certain point of time. a denotes the relative brightness of the horizon; b quantifies the gradient of the horizontal brightness in the zenith direction; c defines the relative irradiance of the circumsolar region, while d defines its width, and e takes into account the irradiance reflected back from the earth's surface [44].

The ground albedo

The next step to predict the irradiance on a tilted surface is to take the reflection from the ground (albedo) into account. The ground albedo (often simply called "albedo") is defined as the reflectance of the ground, assuming it to be a Lambertian surface; this is equivalent to the assumption that the ground emits or reflects the same amount of radiant flux in each direction. A Lambertian surface therefore appears to have the same brightness independent of the observer's position. The light emitted by these surfaces follows the Lambertian cosine law of Eq. 2.6, θ_M being the incidence angle on the module surface.

$$\frac{d}{dA}\Phi(\theta_M) = L\, d\Omega \cos\theta_M \tag{2.6}$$

A standard value for the ground albedo in many PV or daylight simulation programs is 0.2. In fact, grass has an albedo of 0.18-0.25, while the albedo of snow is in the range of 0.45 to 0.9 [1]. This can lead to incorrect simulated irradiance values, especially during the winter. In general, this error is neglected for PV modules installed in Central Europe with a standard tilt angle of around 30°. However, the albedo fraction of the irradiance will increase for vertical PV module orientations; furthermore, the magnitude of the albedo value gains importance, as is described in subsection 4.2.2.

2.2.4 Optical analysis of the BIPV system surroundings

For the shading analysis, besides simulating the sky radiance distribution, it is necessary to define the BIPV system surroundings. For this purpose, two different approaches can be taken. The first one defines shading objects by their altitude and azimuth angles. The second one traces all the possible paths a ray can take within a given geometrical configuration, taking into account not only the dimensions and positions of the shading objects but also the reflectance of their surfaces.

The angular definition of shading objects

For electricity yield calculations of PV systems with shading objects in the surroundings, common programs like PVsyst [46] or PV*SOL Expert [45] define the objects by the angular regions of the hemisphere that they cover. These angles can be directly measured with commercial shade analysis devices. Within the calculation, the direct irradiance fraction is set to zero if the sun's position is located within the measured angles. This approach saves calculation time but has various disadvantages that all arise from the unknown distance between the shading objects and the PV module. (As a result, the size of the shading objects is also unknown.) On the one hand, it neglects the fact that the diffuse irradiance fraction is also influenced by shading, as well as the fraction that results from the ground albedo. On the other hand, if there are large shading objects like neighboring buildings, the reflection from these objects can be relevant but is also neglected.

The approach can be adequate for small shading objects and can be applied for most PV systems that are not building-integrated. However, for the simulation of BIPV systems, neighboring buildings can have a high impact on the irradiance reaching the PV cells, especially if the PV modules are mounted vertically. (For selected surroundings, the effect is quantitatively analyzed in subsection 4.2.3.) For the general case, a more detailed optical analysis of the surroundings is desired.

The analysis of the radiance distribution within a geometrical configuration

To analyze the interplay of the radiance distribution between the PV cell surfaces and the surroundings, for example the amount of radiation reflected by an adjacent building, the radiance distribution for the geometrical configuration as a whole has to be taken into consideration. For this calculation, many known and developed approaches already exist in the field of computer graphics. When an image is "rendered", the radiance distribution over the geometrical configuration is needed to calculate the radiance for every pixel of the image. However, no commercial PV electricity yield simulation program has yet incorporated a ray-tracing process in the PV yield simulation. Nevertheless, applying such a tool for the purpose of BIPV electricity yield simulations is an obvious option; especially for daylight simulations of buildings, ray-tracing simulations have been established for many years. The most important possibilities for simulating the radiance distribution of a given geometrical configuration are described below.

There are two main methods to calculate the radiance distribution for a defined geometrical configuration, the radiosity and the ray-tracing procedures. The radiosity method follows every light path from the light sources (for example, it calculates every path from a simulated Perez sky to a certain geometrical configuration) and calculates the radiance on every discrete point in the geometrical configuration. To achieve that, reflections by objects are taken into consideration by treating them as weak, diffuse light sources. The approach has the advantage of calculating the radiance of every geometrical point at the same time; however, this is not necessary for PV yield simulation purposes. Besides, there are two major disadvantages of the radiosity method. First, the radiosity approach only works with Lambertian surfaces as defined by Eq. 2.6; even slightly specular surfaces cannot be taken into account. Second, even with this limitation, calculation times are very long.

The ray-tracing approach, developed by Arthur Appel, Robert Goldstein and Roger Nagel [2, 18], focuses directly on one point and direction inside the geometrical configuration. This point is called a *grid point* within this thesis, the direction *view direction*. Then, only the rays that are important for the irradiance on the grid point have to be calculated, which can save a lot of of calculation time. In most cases, the rays are followed backwards from the grid point in all directions until they reach a light source. This approach is called backward ray tracing. Within daylight simulations, due to the small solid angle of the sun, a combined approach is applied: The rays from the sun are followed until they reach the objects (called "direct calculation" in the RADIANCE program, see section 3.2); afterwards, backward ray tracing is started ("ambient calculation"). The ray-tracing process is much faster than the radiosity procedure; therefore, also non-Lambertian surfaces as well as transmitting objects can be integrated. However, to a certain extent, the calculation has to be restarted for each different grid point. A complete "grid" covering the whole surface is needed to simulate inhomogeneous irradiance on a PV cell or module. The number of grid points needed in the "grid" depends on the inhomogeneity of the irradiance on the PV cell surface.

2.2.5 Separating the geometrical configuration and the sky simulation

When applying a ray-tracing procedure for the simulation of the irradiance for a whole year, the optical analysis of the geometrical configuration has to be restarted for every single time step when the sky radiance distribution, but not the configuration itself, changes. This problem has already been addressed in the related field of daylight simulations (required by architects to avoid glare as well as too dark regions inside a building). The idea of separating the simulation of the sky radiance distribution from the ray tracing of the given morphology was introduced by P.R. Tregenza in 1983 [62]. After dividing the sky into a certain number of sky regions, the contribution of every region to the ray-tracing result can be analyzed. In daylight simulations, these (photometric) contributions are called daylight coefficients. After this calculation, the radiance (or, for daylight simulations, luminance) values can be calculated for each time step. This is done by multiplying the time-dependent sky radiance values for the sky regions with the corresponding time-independent contributions of the sky regions to the radiance on the chosen grid point. Following this approach, the irradiance on a grid point *GP* can be calculated by Eq. 2.7.

$$E_{GP} = \sum_{i=1}^{N} f(i) \cdot E_i \rightarrow \sum_{i=1}^{N} f(i) \cdot L_i \cdot \Omega_i \tag{2.7}$$

$f(i)$ represents the contribution of a sky region i to the irradiance at the grid point, and N is the total number of sky regions. If N is large enough, the radiance L can be considered to be constant over the whole sky region with solid angle Ω_i. Although this assumption is necessary due to the separation of the sky radiance distribution and the ray tracing of the given geometry, it leads to problems for direct sunlight. The approach does not allow the solid angle of the sun ($\Omega_{sun} = 6.8 \cdot 10^{-5}$ sr) to be modelled with adequate spatial resolution. The direct solar radiation has to be either allocated to one sky region or distributed to the neighboring sky regions, which enlarges the solid angle of the sun. A solution to this problem could be to separate the direct and the diffuse irradiance components for the calculation, as has been implemented in the program *daysim* [10]; however, this requires the definition of sun positions for the direct irradiance component in addition to the sky regions for the diffuse irradiance fraction. Then, also the impact of the sun positions on the irradiance on the grid points has to be calculated in advance. The approach leads to a deviation in the sun's position, dependent on the number of precalculated sun positions.

A related but more detailed method to increase the simulation speed that has been developed during this thesis is presented in section 3.2.

Another restriction of the method of separating the simulation of the sky radiance distribution from the ray tracing of the geometrical configuration should be mentioned. Separating the geometry from the sky simulation is only possible if the optical properties of the modelled materials and the morphology are assumed to remain constant over the whole year. Changes like a higher ground albedo due to snow or moving objects cannot be considered within this method.

2.3 Spectral simulation

Within section 2.2, the spectral dependence of the measured irradiance has been neglected. As can be read from Eq. 2.1, the energy of an electromagnetic spectrum and, as a consequence, also the radiance and irradiance values can be equal for different spectral distributions $dN/d\nu$. As PV cells are based on semiconductor materials which show high transmittance at low photon frequencies corresponding to energies lower than the band gap, the spectral distribution of radiation is of course important for the calculation of its absorption. However, the spectral distribution can be important not only for the photovoltaic layers themselves, but also for reflection, transmission and absorption of surrounding objects as well as for the optical analysis of complex BIPV elements.

However, for most calculations within this thesis, the sky radiance distribution has been calculated on the basis of measured irradiance values on a horizontal plane. The spectral changes to the broadband irradiance measurements have been neglected. The validations of the irradiance simulation, described in section 4.5, show only small deviations, mostly on sunny days. For PV modules with high tilt angles or non-southern orientations, the impact of spectral deviations to the PV electricity yield are certainly relevant; due to the lack of measurement data, the investigations of the impact of spectral deviations on the BIPV electricity yield within this PhD thesis are restricted. Nevertheless, the main issues related to the spectral distribution of the irradiation are summarized within this section.

2.3.1 The spectral distribution of the sky radiation

The most common approach to quantify the spectral distribution of the sky radiation is to restrict the examination to the spectral distribution of the direct, global, circumsolar and hemispherical-tilted irradiation. The spectral distribution can be calculated with the program SMARTS (acronym for: simple model of the athmospheric radiative transfer of sunshine) developed at the National Renewable Energy Laboratory by C.Gueymard [58]. The program considers Rayleigh scattering as well as ozone absorption, mixed gas absorption, trace gas absorption, water vapor absorption and aerosol extinction [39]. A simpler and faster model had already been published in 1984 by Bird and Riordan, which considers atmospheric turbidity, surface pressure, the amount of water vapor, ozone, and ground albedo [4].

For the direct- and global spectral distribution, the air mass is important. The air mass (*AM*) is defined as the path length of direct sunlight through the atmosphere relative to the minimal path length for a receiver at sea level. It can be calculated with Eqs. 2.8 and 2.9 [27, 29].

$$AM(\theta_Z) = [\cos(\theta_Z) + 0.5057 \cdot (96.080 - \theta_Z \cdot 180/\pi)^{-1.6364}]^{-1} \tag{2.8}$$

$$AM_h(\theta_Z) = \exp^{-0.0001184 \cdot h} \cdot AM(\theta_Z) \tag{2.9}$$

with $AM(\theta_Z)$ being the air mass at sea level and $AM_h(\theta_Z)$ the air mass at altitude h. The air mass numbers are also applied to name spectral distributions. For example, the abbreviation AM1.5 defines the spectrum when the position of the sun causes the direct sunlight to traverse an atmospheric path which is 1.5 times longer than the vertical one (corresponding to an incidence angle of the direct irradiation of θ_Z=48.2°). These AM spectra are a common standard for PV efficiency measurements. Based on a publication by Gueymard [22], Fig. 2.3 shows the circumsolar-direct and hemispherical-tilted AM1.5 spectral power density. Both can also be measured with a spectroradiometer.

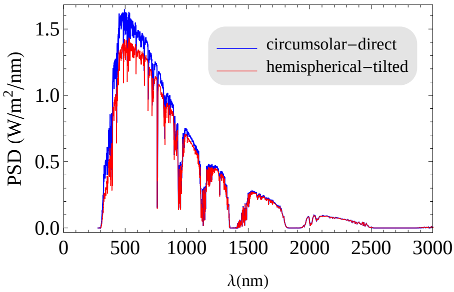

Figure 2.3: The AM1.5 spectra for the circumsolar-direct and hemispherical-tilted power spectral density (PSD) as defined in the standard ASTM-G-173-03. The tilt angle is 37°; the orientation is due south.

2.3.2 Effect of spectral mismatch on irradiance measurements

The spectral distribution of radiation affects the results of irradiance measurements. When the irradiance is measured simultaneously with different devices at the same orientation and location, the results can differ from each other. This difference depends on the spectral response of the devices and the spectral distribution of the irradiation. Fig. 2.4 shows the dependence of the output signal on the wavelength for various irradiance sensors.

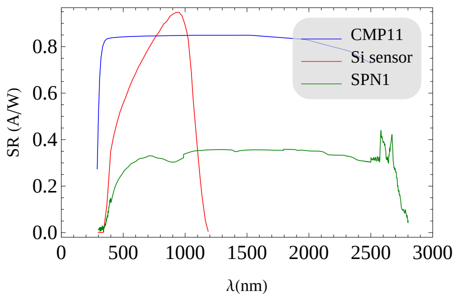

Figure 2.4: Spectral response for the following irradiance sensors: CMP11 pyranometer, c-Si sensor, SPN1 pyranometer. With kind permission of Kipp&Zonen and Dynamax.

With the calibration of the measurement device, a constant factor between the output signal and the resulting irradiance value at a certain spectral distribution is determined. In most cases, the AM1.5 spectral distribution is taken as a calibration basis. Therefore, the device measures incorrect irradiance values for spectral distributions different to AM1.5. The error can be corrected by the spectral mismatch factor MM_{spec}, which is calculated by Eq. 2.10 [38].

$$MM_{spec} = \frac{\int_{280nm}^{2500nm} SR(\lambda)\, \Phi_s(\lambda)\, d\lambda}{\int_{280nm}^{2500nm} SR(\lambda)\, \Phi_m(\lambda)\, d\lambda} \; \frac{\int_{280nm}^{2500nm} \Phi_m(\lambda)\, d\lambda}{\int_{280nm}^{2500nm} \Phi_s(\lambda)\, d\lambda} \qquad (2.10)$$

$SR(\lambda)$ is the spectral response of the measurement device, Φ_s is the standard spectral distribution used for calibration, and Φ_m is the measured global spectral distribution of the incident light. The ratio of the measured irradiances of one device to a second one for a given spectral distribution can be calculated by dividing MM_{spec} of the first by MM_{spec} of the second device.

2.3.3 Spectral corrections in a PV electricity yield simulation

When the global and diffuse irradiance on horizontal or tilted planes is measured, the spectral mismatch between the AM1.5 global and the incident spectral distribution has to be simulated if the result is to be used for an accurate PV electricity yield simulation. The result depends on the spectral response of the measurement device, as described in Eq. 2.10. For sun-tracked PV modules and irradiance sensors, a relationship between the air mass number and the spectral mismatch factor has been detected. In general, MM_{spec} for wafer-based PV cells increases with higher air mass [29]. For PV modules that are not sun-tracked, no satisfying model to calculate the spectral mismatch has been developed yet. Furthermore, with the assumption of a spectral mismatch function depending on the air mass alone, the approach neglects the dependence of the spectral distribution on the incident direction. No spectral measurements of the irradiation have been performed within this thesis. However, the spectral analysis of every sky region would open up many possibilities for the optimisation of PV and BIPV elements. For example, it may be possible to extend the simulation approach for the time-resolved irradiance described in subsection 2.2.5 by the mismatch factor of Eq. 2.10. Furthermore, the spectral distribution of the incident light at different incidence angles and its consequences on the electricity yield could be analyzed for various PV module orientations.

2.3.4 Consequences of the spectral distribution of the incident irradiation on the BIPV electricity yield

The PV module efficiency for certification purposes is usually measured with normally incident AM1.5 irradiance of 1000 W/m^2 and a module temperature of 25°C, the so-called standard test conditions (STC). For BIPV applications, these four conditions almost never coincide. For vertically oriented BIPV systems, the diffuse light fraction is frequently higher than for free-standing PV systems. As the diffuse irradiation fraction is blue-shifted due to Rayleigh scattering, PV technologies based on semiconductor materials with a higher band gap energy than monocrystalline silicon, such as most of the thin-film technologies, show higher average light absorption per irradiance when installed vertically than for a tilt angle similar to the latitude.[5]

The consequences of the deviation of the BIPV conditions from standard test conditions can be more serious again for vertically installed multi-junction PV cell technologies. If the component cells of a multi-junction PV cell are serially connected and the cell efficiency is optimized to STC, deviations of the spectral distribution of the incident light from the AM1.5 standard spectrum as well as high incidence angles can lead to different absorptance in the two semiconductor absorber layers and therefore to major electrical mismatches between the two component cells of the multi-junction PV cell. The quantitative analysis of this loss mechanism again needs spectral measurements of different sky regions, maybe including the polarisation due to its impact on the reflection, and an incidence-angle-dependent coherent optical simulation of the multi-junction cell's layer composition. Then, the electrical mismatch losses for BIPV applications could be determined.

Despite the mentioned spectral effects, the spectral deviations have been ignored within the PV simulations of this PhD thesis. When calculating the irradiance incident on a tilted plane from the measured global and diffuse horizontal irradiance values, the change in the spectral distribution of the incident light dependent on the tilt angle has to be determined by measurements. These measurements are time-consuming and have not been performed during the period of this thesis. However, the irradiance evaluation also shows quite good results when the spectral deviations are ignored, as can be read in section 4.2 and subsection 4.5.1.

2.4 Angular response of a PV module and optical simulation inside the PV module

As the electric power generated by a PV module depends mainly on the temperature and the irradiance, the module efficiency is defined at specified standard test conditions, called STC. The PV modules are tested with a flasher of 1000 W/m^2 irradiance at normal incidence with the spectrum AM1.5 global, at a module temperature of 25°C. This testing procedure is well-suited to compare PV cells and modules of the same technology with each other as well as to do tests concerning degradation or light-soaking and annealing; however, in reality, the modules of PV systems are almost never exposed to these conditions. Not only the spectral deviation of the incident light from AM1.5 is important for BIPV applications, but also higher temperatures, as described in section 2.7, and obliquely incident irradiation plays a significant role for the electricity yield.

[5] However, this does not automatically mean that thin-film technologies are better suited for vertical orientations. The effect has to be compared with the more important low-light behavior of the technology which is, in most cases, worse for thin-film technologies.

To make the simulation of the irradiance on the PV module surface applicable for an electricity yield simulation, there are two basic approaches. Either, the simulated irradiation is compared to standard test conditions, and the I–V curves are taken from laboratory measurements, as described in subsection 2.4.1, or, the amount of absorbed light, and finally the I–V curves at different irradiance and temperature conditions, are directly calculated with a software program like ASA [3], as described in more detail in chapter 3.3.

2.4.1 The effective irradiance

To allocate the simulated irradiance values to I–V curves measured in the laboratory, the incidence angle dependence of the irradiation and the spectral deviation from AM1.5 has to be considered. This can be done by calculating the effective irradiance, which is defined as the irradiance at AM1.5 and normal incidence that would lead to the same amount of electron-hole pairs in the photovoltaic material as in the present case. It can be calculated according to Eq. 2.11.

$$\begin{aligned} E_{eff} &= \int_{\Omega} L \cdot K \cdot MM_{spec} \cdot \cos\theta_M d\Omega = \\ &= \int_0^{2\pi} \int_0^{\pi/2} L(\theta_M, \phi_M) K(\theta_M, \phi_M) MM_{spec}(\theta_M, \phi_M) \cos(\theta_M) \sin(\theta_M) d\theta_M d\phi_M \\ &= \int_0^{2\pi} \int_0^{\pi/2} L(\theta_M, \phi_M) K(\theta_M) MM_{spec} \cos(\theta_M) \sin(\theta_M) d\theta_M d\phi_M = \\ &= 2\pi \cdot MM_{spec} \cdot \int_0^{\pi/2} L(\theta_M) K(\theta_M) \cos(\theta_M) \sin(\theta_M) d\theta_M \end{aligned} \tag{2.11}$$

The equation is similar to Eq. 2.4, but with the correction functions K and MM added. K is the angular response, MM the spectral response. In the case of non-complex BIPV modules, the dependence of the angular response function on the azimuth ϕ_M of the PV module reference system and the dependence of the spectral response function on both the incidence angle θ_M and the azimuth ϕ_M of the PV module reference system are neglected, leading to the lowermost expression of Eq. 2.11.

For incidence angles different to 0°, there are two effects that have to be accounted for. First, the irradiance on the PV module surface area, given in W/m^2, decreases with increasing incidence angle, leading to the cosine factor in the equation. θ_M is the incidence angle of the irradiation on the PV module. In addition, the change of the amount of reflected and transmitted light dependent on the incidence angle relative to the vertical case has to be considered. For BIPV modules with rotationally symmetric reflectance behavior, the latter change can be characterized by the "angular response" function K, described in 2.4.2. For complex BIPV modules, a more sophisticated approach to apply the irradiance simulations to the calculation of the BIPV electricity yield is required, as described in 2.4.4.

The effective irradiance does not contain the reflection loss at normal incidence angles (the angular response K is 1 at 0° incidence angle).

The impact of the spectral deviation of the incident light from AM1.5 can be calculated by MM_{spec}, given in Eq. 2.10. Until a simulation model is developed for the spectral distribution of the incident light on general PV module surface orientations, maybe dependent on the air mass, MM_{spec} has been set to 1. The quantitative error resulting from this simplification, however, is not very large, as suggested by the irradiance validation results of 4.5.1.

2.4.2 The angular response

The angular response of a PV module can be defined by Eq. 2.12 [36].

$$K = \frac{A(\theta)}{A(0)} \tag{2.12}$$

$A(\theta_M)$ is the absorptance of the PV module at an incidence angle of θ_M. By definition, the angular response for an incidence angle of 0° is 1. Eq. 2.12 also implies that the angular response function can only be applied to PV modules without a dependence of the absorptance on the module azimuth ϕ_M.

For modeling the angular response of PV modules, the ASHRAE model is widely accepted [42], represented by Eq. 2.13.

$$K = 1 - b_0\left(\frac{1}{\cos(\theta_M)} - 1\right) \tag{2.13}$$

The parameter b_0 is called the incidence angle modifier coefficient.

However, the ASHRAE model obviously is wrong for incidence angles near 90° where the model predicts a K value of $-\infty$ while it should be 0. For opaque PV cells and modules, a more detailed model was developed by N.Martin and J.M.Ruiz in 2001 [36]. With this model, the K value is calculated according to Eqs. 2.14 and 2.15.

$$R(\theta_M) = R(0) + [1 - R(0)] \cdot \frac{\exp[-\cos(\theta_M)/a_R] - \exp[-1/a_R]}{1 - \exp[-1/a_R]} \tag{2.14}$$

$$\begin{aligned} K = \frac{A(\theta_M)}{A(0)} &= \frac{1 - R(\theta_M) - T(\theta_M)}{1 - R(0) - T(0)} \cong \frac{1 - R(\theta_M)}{1 - R(0)} \\ &= \frac{\exp[1/a_R] \cdot (1 - \exp[-\cos(\theta_M)/a_R])}{\exp[1/a_R] - 1} \end{aligned} \tag{2.15}$$

The parameter a_R can be found by fitting the results of angle-dependent measurements of the short-circuit current. Values for PV modules based on different technologies can be found in [36]. For PV modules with transparent sections, for example the PV modules of the saw-tooth roof PV system shown in Fig. 4.41, the model can be applied by only considering the opaque parts of the PV module. Semi-transparent PV cells, however, can only be treated by measuring the dependence of reflectance and transmittance on the incidence angle.

As the model of Martin and Ruiz has been validated in detail, with R^2 values (see appendix A) of above 99.8% in all cases when comparing measurements with simulations, the ASHRAE model can be considered to be out-dated. The a_R values have been calculated for different layer compositions of PV modules based on crystalline and amorphous silicon.

As Eqs. 2.14 and 2.15 suggest, the model of Martin and Ruiz can also be applied to calculate the transmittance of a layer with negligible absorptance. Fig. 2.5 shows the results of the ASHRAE model for different b_0 values as well as the result of the model of Martin and Ruiz for an air-glass interface.

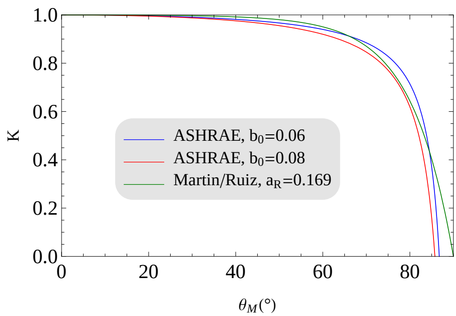

Figure 2.5: The angular response K versus the incidence angle on the module, θ_M. The figure shows the results of the ASHRAE model with b_0=0.06 and b_0=0.08, compared to the result of the model of Martin and Ruiz with a_R=0.169.

Both the model of Martin/Ruiz and the ASHRAE model neglect the spectral dependence of the incident radiation, also the measurements have been made with AM1.5 only. For other spectral distributions than AM1.5, a more detailed approach has to be taken. Within this PhD thesis, the angular response function K is assumed to be independent of the spectral distribution of the incident light.

2.4.3 Models for the effective irradiance

Common PV simulation programs do not analyze the dependence of the radiance on the incidence angle $L(\theta_M)$ because its simulation is too time-consuming. One possibility to get a rough result for rotationally symmetric PV modules is to divide the irradiance into a direct and a diffuse fraction. As the incidence angle of the direct sunlight can be calculated easily, the relative reflection loss of the direct fraction to the case of normal incidence can be calculated by assuming an angular response curve. The diffuse fraction is mostly considered to have a constant incidence angle of 60°, which leads to Eq. 2.16.[6]

$$E_{eff} = [E_{dir} \cdot K(\theta_{dir}) + E_{diff} \cdot K(60^\circ)] \cdot MM_{spec} \tag{2.16}$$

with K being the angular response of the module. With Eq. 2.16, the higher irradiance fraction from the circumsolar region in the diffuse irradiance is neglected as well as the change in incidence angle dependence of the irradiation when shading or reflection occurs. The applicability of this approach for vertical orientations depends on the angular response of the module and has to be analyzed (which, at least for one typical angular response curve, is done in section 4.2).

2.4.4 Optical simulation of complex BIPV structures

The challenges that arise when performing an optical simulation of a complex BIPV system are demonstrated with Fig. 2.6.

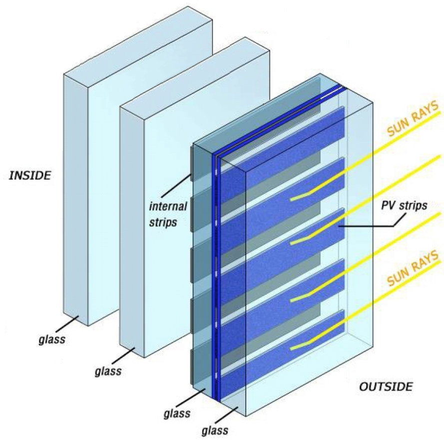

Figure 2.6: The structure of the PVShade® BIPV triple glazing unit. To achieve a higher U-value, two glass panes are added behind the PVShade® module. Optionally, the gaps in between are filled with argon. The photovoltaic stripes are shown in blue; they represent a number of series-connected PV cells, each consisting of the standard layer sequence for amorphous silicon cells on the glass superstrate: TCO/p-type Si/intrinsic Si/n-type Si/Al. Source: [15]

As described in section 1.2, the PVShade® module consists of two thin-film modules of amorphous or tandem micromorph silicon that have been laser-ablated

[6]Although the approach of Eq. 2.16 is widely accepted, I was not able to find any reference.

to form a pattern of photovoltaic stripes along the series connection of the PV cells; then, the two modules are subsequently laminated to each other. The procedure leads to two PV subsystems with lower DC current, but the same DC voltage compared to a standard PV module.

For most façade applications, the BIPV element has to reach a sufficiently low heat transfer coefficient (U-value). For this reason, two further glass panes, at least one with a low-e coating, are installed on the back of the BIPV element; the spaces between the glass panes and the BIPV element are commonly hermetically sealed and filled with a gas like air, argon or krypton. For the outward-facing surfaces of the two blue layers in Fig. 2.6, the effective irradiance has to be determined for every time step. The blue layers summarize the layer sequence TCO/p-type Si/intrinsic Si/n-type Si/Al, whereby the back surface is significantly reflective. In order to determine the irradiance on the PV cell, the reflections from the back metal contact of the cell and the glass-air interfaces have to be taken into account.

For complex BIPV systems, Eq. 2.16 cannot be applied. A ray-tracing approach is required to calculate the effective irradiance, starting within the glass. A detailed description of the latter procedure is given in section 3.2.

The result of the ray-tracing procedure will be the irradiance on the cell surfaces just before the glass-TCO interface. After simulation of the irradiance at the same ray-tracing sensor under STC conditions, the effective irradiance can be calculated by dividing the simulated irradiance of every time step by the simulated irradiance at STC, following Eq. 2.17.

$$E_{eff,t} = E_{sim,t} / E_{sim,STC} \tag{2.17}$$

The approach neglects the angular response of the glass–TCO interface. However, due to the light refraction at the air–glass interface, most of the irradiation will have an incidence angle on the TCO layer below 42°, which makes this simplification acceptable. The approach also neglects spectral changes due to reflection and transmission within the module.

In the case of the PVShade® module, geometrical optics can be applied for the calculation of the effective irradiance; the thin-film layers play a negligible role for the reflectivity of the glass-TCO surface. For some complex BIPV modules, the consideration of coherence or dispersion effects may be necessary, especially if thin-film layers or total reflections play a major role. A thin-film layer can be defined as a layer with a thickness of the same order of magnitude as the wavelength of the radiation. In this case, consideration of the spectral distribution of the incident light may be required, applying similar equations as described in section 3.3.

2.5 Calculation of the cell I–V characteristics

BIPV systems are frequently exposed to inhomogeneous irradiation, either due to PV modules of different orientation wired together or due to shading situations. To analyze the electricity yield of inhomogeneously irradiated BIPV systems, the I–V characteristics have to be analyzed at the cell level. Fig. 2.7 shows an arbitrary I–V curve of an arbitrary PV cell, including the definitions of the quadrants.

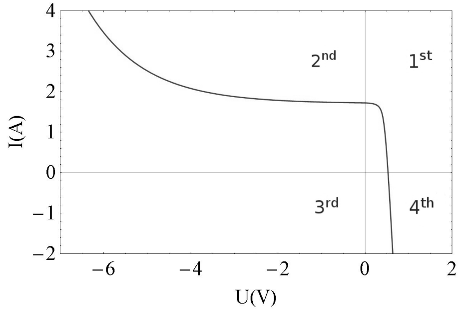

Figure 2.7: An arbitrary I–V curve, measured at standard test conditions (STC). Within this PhD thesis, the quadrants are counted as defined in the graph. In the first quadrant, electrical power is generated. In some publications, the sign of the current is chosen differently, leading to a different numbering of the quadrants.

The I–V curve of the cells has to be known for every pair of effective irradiance and cell temperature; this database of I–V curves has to be created at the beginning of the electricity yield simulation. To do so, there are two basic approaches. In one, the I–V curve of the installed PV modules is or has been measured at standard test conditions (T=25°C, E=1000W/m^2, AM1.5). Then, the parameters of the one-diode or two-diode model can be fitted to this I–V curve, resulting in the I–V curve at different temperatures and irradiances. In the other approach, the I–V curves for different temperatures and irradiances are calculated directly, based on detailed knowledge of the structure of the cell and the layer's properties. However, and most frequently for thin-film PV technologies, this detailed knowledge cannot be gathered from an already manufactured, commercially available PV module; the PV companies have confidential information about the production process, and most layer properties, like the spectrally dependent reflectance and transmittance, can only be measured if the layer is available as a separate sample.

Within this PhD thesis, a combined approach has been followed. The diode models are taken as the basis for PV system yield simulations, also without knowledge of the exact layer properties. More detailed investigations are applied to verify the assumptions made by the equivalent circuit approach. The detailed investigations also identify where further research is required. In subsection 4.3.1, the I–V curves of an a-Si PV cell at low light intensities are simulated with the two-diode model and are compared to a more detailed simulation with the program ASA.

2.5.1 I–V curves based on diode models

As discussed in many PV textbooks, the electrical behavior of a PV cell can be described by an equivalent circuit. Details can be found in [47]. The equivalent circuits of the one-diode and two-diode models are presented in Fig. 2.8. The one-diode model leads to the implicit equation 2.18.

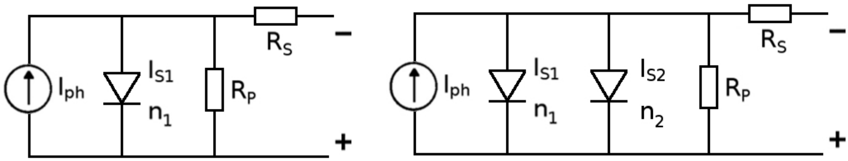

Figure 2.8: The equivalent circuits of a PV cell according to the one-diode model (left) and the two-diode model (right). One and two diodes, respectively, are connected in parallel to a constant current source. Both circuits include a series and a parallel resistance.

$$I = I_{ph} - I_{s1} \cdot (\exp(\frac{V + R_s \cdot I}{n_1 \cdot V_T}) - 1) - \frac{V + R_s \cdot I}{R_p} \qquad (2.18)$$

The diode is defined by the reverse saturation current I_{s1} and the ideality factor n_1 (which is assumed to equal 1), while the thermal voltage V_T can be calculated by Eq. 2.19, with the elementary charge q and the Boltzmann constant k_B. The photocurrent I_{ph} is calculated by assuming a linear relation between the short circuit current I_{sc} and the irradiance E, and inserting the values under short circuit conditions, $(V, I) = (0, I_{sc})$, which leads to Eq. 2.20 and 2.21.

$$V_T = k_B T / q \qquad (2.19)$$

$$I_{sc} = I_{sc}^{STC} \cdot \frac{E}{1000\,W/m^2} \qquad (2.20)$$

$$I_{ph} = I_{sc} \cdot (1 + \frac{R_s}{R_p}) + I_{s1}(\exp[\frac{R_s I_{sc}}{n_1 V_T}] - 1) \qquad (2.21)$$

Within the equivalent circuit, the parallel and series resistance are called R_p and R_s, respectively. However, as shown by A.Wagner [64], the one-diode model is also useful with negative series resistances. For monocrystalline silicon technology, the dependence of the I–V curve on the temperature and the irradiance can be simulated with this "effective" I–V curve within 1.5% for the normal range of operation temperatures and irradiances.

An equivalent circuit with two diodes leads to the implicit equation given in Eq. 2.22.

$$I = I_{ph} - I_{s1} \cdot (\exp(\frac{V + R_s \cdot I}{n_1 \cdot V_T}) - 1) - I_{s2} \cdot (\exp(\frac{V + R_s \cdot I}{n_2 \cdot V_T}) - 1) - \frac{V + R_s \cdot I}{R_p} \quad (2.22)$$

The two diodes are again defined by their reverse saturation currents I_{s1} and I_{s2} and their ideality factors of n_1 and n_2. In most cases, n_1 is assumed to equal 1. The photocurrent again can be calculated by the assumption of Eq. 2.20 and the resultant function value $(V, I) = (0, I_{sc})$, which leads to Eq. 2.23.

$$I_{ph} = I_{sc} \cdot (1 + \frac{R_s}{R_p}) + I_{s1} \cdot (\exp[\frac{R_s I_{sc}}{n_1 V_T}] - 1) + I_{s2} \cdot (\exp[\frac{R_s I_{sc}}{n_2 V_T}] - 1) \quad (2.23)$$

For monocrystalline PV cells, the temperature dependence can be determined from the STC curve. Not only the thermal voltage V_T, but also the parameters I_{ph}, I_{s1} and I_{s2} are temperature-dependent, in accordance with the Eqs. 2.24, 2.25 and 2.26.

$$I_{ph} = (C_0 + C_1 T)E \quad (2.24)$$

$$I_{s1} = C_{s1} T^3 \exp[-\frac{V_{\text{gap}}}{n_1 k_B T}] \quad (2.25)$$

$$I_{s2} = C_{s2} T^{5/2} \exp[-\frac{V_{\text{gap}}}{n_2 k_B T}] \quad (2.26)$$

With the assumption $I_{ph} \approx I_{sc}$ and the temperature coefficient α for I_{sc} from the data sheet, the two constants of Eq. 2.24 can be calculated. The result leads to the temperature coefficients β and γ for the open circuit voltage and the MPP power, which can be validated with the values from the data sheet.

The results of this parameter fitting are presented and discussed in section 4.5. It can be summarized that only the results for monocrystalline cells agree with the data sheet parameters, whereas the relationships in the Eqs. 2.24, 2.25 and 2.26 are not valid for PV modules based on amorphous silicon technologies or tandem a-Si/μ-Si technologies. Some thin-film technologies also show a temperature-dependent low-light behavior that cannot be simulated by the two-diode model. Furthermore, PV modules based on thin-film technologies can have inconsistent material quality which does not allow the behavior of one PV cell to be generalized to all the cells coming from the same production line. If, despite these limitations, the two-diode model is applied to thin-film technologies, the resulting I–V curves are not satisfying. As these uncertainties, can be the most critical ones in the whole PV system simulation chain, a more detailed analysis of the low-light behavior is desirable. One possibility is to perform many PV cell measurements; however, test cells that are small enough to handle are not easy to fabricate by a production line that normally makes large glass-glass modules. The other possibility, independent of any manufacturer, is to produce a-Si cells oneself and analyse the intermediate steps of the production process. This more detailed analysis is described briefly in the next section while its results for an arbitrary amorphous silicon PV cell are summarized in section 4.3.1.

For a commercially available PV module ndependent of the technology, it is of course far easier to measure the STC I–V curve of the full PV module instead of measuring the I–V curve of the single PV cells. Within this PhD thesis, the cell I–V curves are calculated by dividing the voltage of the module I–V curve by the number of series-connected, and dividing the current of the module I–V curve by the number of parallel connected PV cells. There are two advantages to this approach. First, no single PV cell has to be prepared for measurement. Second, the simulations based on these "quasi-cell" I–V curves do not have to take the cell connection losses explicitly into account. Without detailed measurements of the cell connection losses, the error made by this approach is difficult to quantify; however, the results indicate that it is very low.

2.5.2 Detailed physical modeling of the I–V curve

For the detailed simulation of the cell I–V characteristics at low-light conditions and different temperatures, the calculation of the number of absorbed photons in the photovoltaic layers, described in subsection 3.3.1, has to be combined with the calculation of the current density generated by the PV cell. This calculation, dependent on the external applied voltage, can be performed with the following equations [65].

$$\vec{\nabla}(\varepsilon\vec{\nabla}\psi) = -\rho \tag{2.27}$$

$$\frac{\partial n}{\partial t} = \frac{1}{q}\vec{\nabla}\vec{J}_n + G_{opt} - R_{net} \tag{2.28}$$

$$\frac{\partial p}{\partial t} = \frac{1}{q}\vec{\nabla}\vec{J}_p + G_{opt} - R_{net} \tag{2.29}$$

$$\vec{J}_n = n\mu_n\vec{\nabla}E_{FN} \tag{2.30}$$

$$\vec{J}_p = p\mu_p\vec{\nabla}E_{FP} \tag{2.31}$$

Eq. 2.27 is the Poisson equation with the relative permittivity ε of the material, the electric potential ψ and the charge density ρ. The continuity equations for negative and positive charges are shown in Eqs. 2.28 and 2.29, with the charge densities n and

p, the optical generation rate G_{opt}, the net recombination rate R_{net} and the current densities $\vec{J}_{n/p}$. The latter are connected to the quasi-Fermi energy levels E_{FN} and E_{FP} by Eqs. 2.30 and 2.31, $\mu_{n/p}$ denoting the mobility of the negative and positive charge carriers.

The detailed calculation of the I–V curves on the basis of the physical properties of the PV cell layers is not discussed within this PhD thesis. For performing this calculation, the ASA program described in section 3.3 has been applied. The models and assumptions made by the ASA program can be read in the program's user manual [3]. A short summary, focussing on the simulation of the number of absorbed photons, can be found in chapter 3.3.

2.6 Cell and module connection

To make the voltage level of a PV system suitable for the inverter (in the case of grid integration) or for rechargeable batteries (in the case of stand-alone PV systems), the PV cells are connected in series. Parallel connections are needed to keep the voltage low or to reduce shading losses.

Knowing the I–V characteristics of every component of an arbitrary DC electrical circuit allows the I–V characteristics of the whole circuit to be calculated easily [54]. The total I–V curve of two cells connected in parallel can be calculated by adding up the electric current for each voltage value. For cells connected in series, the total I–V curve equals the sum of the voltages for each current value. If the two considered cells do not have the same I–V curve, these summations in general cannot be performed without knowledge of the electric behavior in the region of negative current (important for the parallel connection) or voltage (series connection). To a certain extent, the behavior at negative currents can be derived from the two-diode model. However, the region of negative voltages, also called *reverse bias*, needs to be simulated in detail.

2.6.1 The electric behavior of PV cells under negative voltage conditions

For the BIPV system in the saw-tooth roof of the Fraunhofer ISE main building, described in subsection 4.5.2, the dark I–V curves of seven polycrystalline silicon cells (Shell Solar, A=12.5x12.5 cm^2) were measured in the negative voltage range; the results are depicted in Fig. 2.9. The measurements were performed with an I–V measurement device (from the company *halm*). As the power of the PV cell resulting from the applied voltage when operated in reverse bias is very high, the duration of each measurement was less than 25 ms to keep the PV cells undamaged.

As can be seen, the reverse bias behavior of the polycrystalline cells is quite variable, even for PV cells from the same manufacturer. The reason is the very strong dependence of the break-through voltage on the amount of doping of the p and n silicon layers. Further investigations of the break-through behavior of polycrystalline

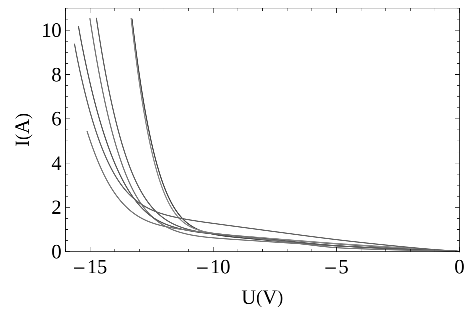

Figure 2.9: The measured dark I–V curves of seven polycrystalline silicon (pc-Si) cells in the negative voltage region.

silicon cells can be found in [32]; the physics of reverse biased PV cells in general is summarized in [31].

Some models exist to simulate the electrical current in the negative voltage range at different temperatures and irradiance values. The best-known of them is the Bishop model [5]. As described in [47], the suggested term I_b of Eq. 2.33 can not only be applied to the one-diode model, but also to the two-diode model, which leads to Eq. 2.32.

$$I = I_{ph} - I_b - I_{s1} \cdot (\exp(\frac{V + R_s \cdot I}{n_1 \cdot V_T}) - 1) - I_{s2} \cdot (\exp(\frac{V + R_s \cdot I}{n_2 \cdot V_T}) - 1) - \frac{V + R_s \cdot I}{R_p} \tag{2.32}$$

with the additional term

$$I_b = g_b \cdot \frac{V + R_s I}{R_p} \cdot (1 - \frac{V + R_s I}{V_b})^{-n_b} \tag{2.33}$$

based on the Bishop parameters g_b, n_b and V_b, with g_b being the fraction of ohmic current involved in the avalanche breakdown, n_b the avalanche breakdown exponent and V_b the breakdown voltage.

Within the simulations of this thesis, the reverse bias simulations have been restricted to an average dark cell I–V curve which is shifted up the current axis by the value of I_{sc} resulting from the I–V curve simulation. This allows a major decrease in calculation time due to the smaller voltage range needed for the numerical I–V curve simulation. (The consequences of the temperature dependence of the cell reverse bias behavior to the system I–V curve depend on the analyzed case, but are small in general.)

2.6.2 Connection of two or more PV cells

The principles of electrical cell connection are indicated in Fig. 2.10. To calculate the I–V curve of two series-connected cells, their voltage values, positive or negative, have to be added for every current value. For cells connected in parallel, the current values have to be added for every voltage value to obtain the two-cell I–V curve. In a computer program, the equality of the current values for series connection and of the voltage values for parallel connection in both I–V tables can be achieved with the help of linear interpolations.
For series connection of two cells exposed to different irradiance conditions, the negative voltage region of the cell receiving less radiation becomes important for calculating the first quadrant of the total I–V curve. For parallel connection, the same applies for the negative current region. Contrary to a popular fallacy, the shape of the I–V curve in the decisive first quadrant is not changed by the connection alone. The only sharp bend of Fig. 2.10 that can be traced back to the connection of the cells alone is that of the green curve at -15 V; however, this bend is only important in theory. If the two-cell system were MPP tracked, the resulting power for series connection would be dominated by the cell with the lower irradiance, while the total power for parallel cell connection, in general, nearly equals the sum of the power from the two individual cells.

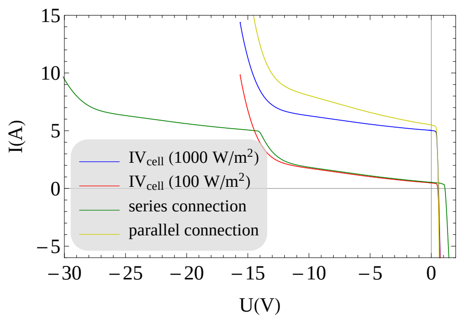

Figure 2.10: The I–V curves of the parallel and series connection of two PV cells. The cells are assumed to operate at different irradiance conditions; for the negative voltage range of the PV cells, one arbitrary reverse bias I–V curve has been chosen from Fig. 2.9. The figure shows the full I–V curves of the pc-Si cell at 100 W/m^2 and at 1000 W/m^2 irradiance, at a temperature of 25°C; in addition, the resulting I–V curves for series and parallel cell connection are depicted.

2.6.3 Bypass and blocking diodes

Solar modules made of wafer-based crystalline silicon PV cells are always manufactured with integrated diodes. These diodes fulfill two functions. First, they prevent the PV cells from being operated at points with negative voltages or currents; second, they may improve the module I–V curve in the first quadrant at partial shading conditions compared to the situation without diodes. Both functions are summarized in the following pages.

When the inverter chooses the operation point of the system I–V curve, it simultaneously defines the operation points of all the PV cells involved. In the case of inhomogeneous irradiation, as in shading situations or when differently oriented modules are electrically connected, the cells can also be forced by the inverter to operate at negative voltages (second quadrant of the cell I–V curve) or currents (fourth quadrant) which leads to an increase of the cell temperature or, in serious cases, to fire. A bypass diode parallel to every series connection and a blocking diode before every parallel connection would lead to complete protection. However, the lifetime of bypass and blocking diodes, especially under conditions with a high level of inhomogeneous irradiation, is shorter than that of PV modules; moreover, their integration into the module is expensive. Therefore, bypass diodes are mostly integrated parallel to about ten to twenty series-connected PV cells (for wafer-based technologies), while blocking diodes, if they are applied, are installed after every parallel module string connection.

The effect of the bypass diode being integrated can be calculated analogously to the description in subsection 2.6.2, as soon as the I–V curves of the bypass (or blocking) diodes are known. The circuit diagram of the case discussed in the next lines is shown on the left side of Fig. 2.11.

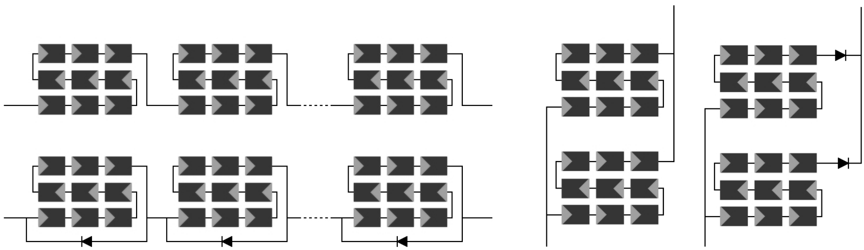

Figure 2.11: The circuit diagrams discussed in the text. Left: (sixteen) PV modules made of nine PV cells each, connected in series, with and without bypass diodes; right: two of the same PV modules, connected in parallel, with and without blocking diodes installed.

The polycrystalline cells are assumed to be protected by a bypass diode after 9 cells each (like the two lower partial modules of Fig. 4.15). 16 of these modules are assumed to be connected in series. While all the other modules operate at STC, one module is shaded to 100 W/m^2; however, for simplification, also this module is assumed to have a temperature of 25°C, and all the cells in this one module are shaded equally. For this system, the I–V curve is calculated with and without a bypass diode connected in parallel to each module. The results are shown in Fig. 2.12.

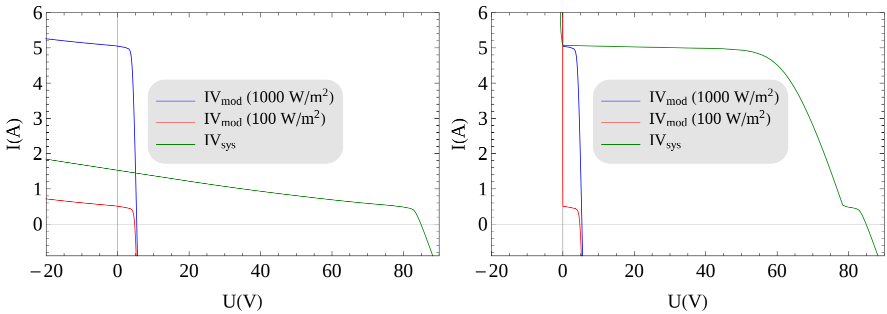

Figure 2.12: The system I–V curve of 16 series-connected modules of 9 cells each, with the I–V curve of each of the 15 modules at STC and the I–V curve of the shaded module. Left: without, right: with bypass diodes connected in parallel to each module.

In the left-hand graph of Fig. 2.12, the influence of the reverse bias voltage on the first-quadrant I–V curve of the PV cell is visible. As depicted in the right-hand graph, a parallel-coupled bypass diode cuts off the negative voltage region of every module. Both of the functions of bypass diodes mentionned above are visible in Fig. 2.12. Assuming the left-hand PV system of 16 modules without the bypass diodes to be MPP tracked, this leads to a system voltage of 61.733 V. With the corresponding current of 0.67 A, the maximum system power is 41.36 W. Now, the PV module operation points can be calculated. For the series module connection, the voltage values of the module I–V curves at the given system current have to be identified. The modules of the unshaded string each operate at 5.195 V; however, the shaded module is operating at -16.195 V. The irradiated solar modules heat up the shaded one.

With the bypass diodes connected in parallel to every module, as on the right side of Fig. 2.12, this danger is averted. Furthermore, the shape of the system I–V curve has improved. Again assuming that the 16-module PV system is MPP tracked, the resulting power is more than six times higher: the maximum power is 271.56 W, at a voltage of 59.035 V and a current of 4.60 A. However, the shape of the I–V curve in the first quadrant changes; sharp bends occur, as depicted on the right side at a voltage of 78 V. With bypass diodes, due to these sharp bends, not only global, but also local power maxima become possible. The consequences are described in subsection 2.9.1.

To understand the functionality of blocking diodes, two 9-cell modules are assumed to be coupled in parallel, one of the two modules operating at STC, the other one being shaded completely. The circuit diagram is depicted on the right side of Fig. 2.11; the resulting I–V curves are shown in Fig. 2.13.

As depicted on the right side of Fig. 2.13, a blocking diode prevents the modules from being operated in the fourth quadrant. This also changes the two-module I–V

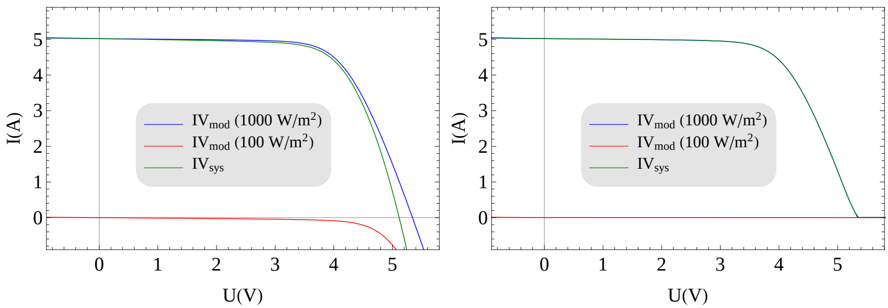

Figure 2.13: The system I–V curve of two modules of 9 cells each, connected in parallel. In addition, the I–V curve of the module operating at STC and the I–V curve of the completely shaded module are depicted. Left: without, right: with blocking diodes connected in series to each module. On the right side, the blue and the green curves are identical, as are the red curve and the abscissa.

curve slightly; assuming the two-module system to be MPP tracked, the left side results in 17.73 W, 3.91 V and 4.53 A, while the values of the right side are 17.81 W, 3.89 V and 4.58 A. Again, the PV module operation points can be calculated; here, the module currents at the given system voltage have to be identified. At the imposed voltage of the discussed example, the shaded module without a diode operates at -0.08 A, while the blocking diode results in 0.00 A current. As demonstrated, the heating up of cells and modules due to shading of parallel configurations is negligible in comparison to series connections. However, the main function of a blocking diode is the prevention of cell or module operating points in the fourth quadrant due to short-circuited cells (or, very seldom, modules) in a string that is connected in parallel to another string; the larger number of serially connected cells of the neighboring string will lead to higher negative currents than in the presented case. Moreover, if the inverter is not MPP tracking, but operating near the open circuit voltage, this also leads to a higher negative operation point of the shaded cell. Therefore, blocking diodes prevent cell heating due to some electrical faults, whereas bypass diodes prevent cell heating due to inhomogeneous irradiation. Further investigations on this topic can be found in section 4.4.

2.6.4 Electrical mismatch

MPP tracking, usually performed by the inverter (see subsection 2.9.1), can only be applied to the system I–V curve. The maximum power point of the system leads to module and cell operation points that in general are not equal to their individual maximum power points. In general, if two PV units (cells, modules or strings) at different operating conditions are connected, the maximum power of the total I–V curve is lower than or equal to the sum of the maximum power of the two partial I–V curves; the imposed operation points of the partial units do not have to be those with maximum power. The power loss resulting from this deviation is called electrical mismatch, summarized in Eq. 2.34.

$$MM_{el} = 1 - \frac{P_{MPP,tot}}{\sum_{i=1}^{N} P_{MPP,i}} \tag{2.34}$$

The index i enumerates the partial units connected together to form the system with the total curve with maximum power $P_{MPP,tot}$. For the BIPV system that was constructed in Ichtershausen in 2012, the mismatch losses due to parallel connection of different module orientations are predicted in subsection 4.5.4.

2.6.5 Partial shading at cell level

In general, the simulation of partial shading at cell level can be handled by splitting up the PV cell in the parts of different irradiation which are then connected in parallel, with all the consequences that have been discussed in subsection 2.6.3. In the case of good conductivity of the electrical cell contacts, the cell behavior is nearly the same as if the whole cell were irradiated homogeneously with the arithmetic mean of the inhomogeneous irradiance [48]. For thin-film technologies like amorphous silicon, the relatively low conductivity of the TCO layer could make the simplification invalid, especially for oblong, partially shaded cells. Experimental studies are required to quantify the effect.

2.7 Temperature analysis

2.7.1 The linear approach

For free-standing PV plants, it is widely accepted – and also again validated in subsections 4.5.1 and 4.5.3 – that the linear approach of Eq. 2.35 [20] is sufficient.

$$T_{mod} = T_{amb} + \kappa \cdot E_{eff} \tag{2.35}$$

To determine the optimal value of κ, a database can be generated with many free-standing PV plants which include temperature measurements, e.g. with a Pt100 sensor, of the back surface of the modules. A value of κ=0.025 K m^2/W, resulting in a temperature difference of 25°C between the ambient and module temperature at an irradiance of 1000 W/m^2, shows good results for glass-glass PV modules as well as for PV modules that have a Tedlar® back surface (like most wafer-based PV modules). In some BIPV cases, a similar linear approach may be adequate. The general approach and its limitations are described in the following section.

2.7.2 Consideration of the BIPV module's layer structure

Fig. 2.14 shows a typical BIPV module's layer structure for use as an insulating glass unit (IGU) (these BIPV modules are installed in the saw-tooth roof of the Fraunhofer ISE main building, see subsection 4.5.2).

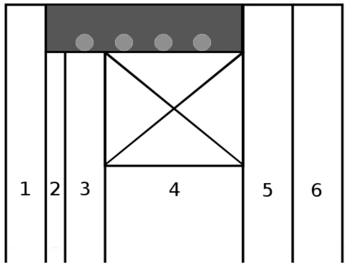

Figure 2.14: Typical layer structure of a wafer-based BIPV module. 1: glass pane, 2: space for the crystalline Si cells embedded in a polymer, 3: glass pane, 4: space filled with air, argon or krypton, 5&6: glass panes laminated with a polyvinyl butyral (PVB) interlayer. The interior surface of the glass pane no.5 has a low-e coating. The diagonal cross indicates a spacer.

If the whole layer structure is considered for the temperature simulation, the thermal conductivity of the materials has to be known as well as the heat transfer coefficient to the inside and the outside environments. Furthermore, if there are gas-filled spaces in the module, also convection and thermal radiation play a role for the heat transport within the BIPV module. Heat conduction, thermal radiation and convection are described briefly in the following lines but are treated in greater detail in many textbooks (e.g. [53]).

Heat conduction

The thermal conductivity, symbolized by λ, describes the heat flux per surface area $\dot{Q}/A = \dot{q}$ inside a gas or material which is caused by transferring kinetic energy from one particle (atom or molecule) to the next. The amount of transferred kinetic energy depends on the difference in temperature between both sides of the gas or the material. For the special case of a layer, which is treated as a cuboid, the phenomenon can be described by Eq. 2.36.

$$\dot{q} = \lambda / d_{layer} \cdot \Delta T \tag{2.36}$$

The heat flux can be calculated if the thickness of the layer d_{layer} and the temperatures at the front and the back of the considered layer are given. Although λ is temperature-dependent in general, especially for gases, the dependence has been neglected within the temperature simulations in this thesis to keep the equations linear.

Thermal radiation

The heat flux due to photon emission is called thermal radiation. If only a single solid body is considered, the Stefan-Boltzmann law of Eq. 2.37 can be applied to describe the radiation emitted by the body.

$$\dot{q} = \sigma \cdot \varepsilon \cdot T^4 \tag{2.37}$$

The thermal radiation depends only on the emissivity factor ε, which has values between 0 and 1, and the temperature, being proportional to T^4. Eq. 2.37 shows that black bodies ($\varepsilon = 1$) have the maximal thermal radiation for a given temperature. The proportionality factor $\sigma = 5.670 \cdot 10^{-8}$ W/m^2/K^4 is called the Stefan-Boltzmann constant.

If the radiative heat flux from one layer to another is calculated, it has to be considered that both layers emit photons; therefore, the difference between the two heat fluxes has to be calculated. This leads to the mathematical term of Eq. 2.38.

$$\dot{q}_{res} = \dot{q}_{12} - \dot{q}_{21} = \sigma \cdot E \cdot (T_1^4 - T_2^4) \tag{2.38}$$

with the thermal radiation exchange parameter E. In the extreme case of one of the two layers being a black body, E equals the emissivity coefficient ε of the other solid. In the case of material-material interfaces, E equals the expression $1/(1/\varepsilon_1 + 1/\varepsilon_2 - 1)$.

The thermal radiation between solids and the sky can be calculated with the help of the sky temperature. To determine the sky temperature, the measurements of a pyrgeometer have to be analyzed. To calculate the resulting thermal radiation, the sky is treated as a black body of this temperature.

Convection

The heat flux caused by macroscopic particle transport is called convection. It plays a role for the heat flux through gases and fluids. In the BIPV case, convection especially influences the heat fluxes within gas-filled gaps and from the BIPV module to the interior and exterior. Especially for the latter case, the calculation of the convective heat flux is very difficult: it depends not only on the temperature difference, but also on the wind speed and direction as well as on the module orientation. The latter is especially important for the simulation of free convection.

Implementation within the simulation

For this thesis, the applied models are kept at a simple level. Air gaps are simulated by assigning a constant "effective heat transfer coefficient". As the heat transfer is a combination of free convection, thermal radiation and thermal conduction, and also the distribution among the three modes is not constant, various dependences are neglected by this assumption.

Also the heat fluxes to the inside and the outside of the considered BIPV module are described by constant heat transfer coefficients h, defined by Eq. 2.39.

$$h = \dot{q}/\Delta T \tag{2.39}$$

This approach neglects the influence of wind, the dependence of the free convection on the orientation, the dependence of the thermal radiation on the sky temperature, and many other effects. Nevertheless, as analyzed in subsection 4.5.2, the simulation quality can be considered to be satisfactory.

With the calculation of the heat fluxes, a system of equations can be set up and solved. The BIPV modules in the saw-tooth roof of Fraunhofer ISE are taken as an example.

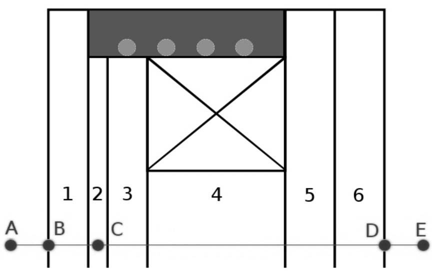

Figure 2.15: Chosen temperature nodes for the cross-section of Fig. 2.14.

In general, the module temperature is either measured on the outermost glass surface or on the innermost glass surface, if a contact sensor is chosen. These temperatures are not equal to the temperature of the PV cells. To estimate the difference, the heat transfer coefficients from one temperature node to the next, shown in Fig. 2.15, have to be calculated.

$$h_{AB} = h_e \tag{2.40}$$

$$h_{BC} = \frac{1}{\frac{d_1}{\lambda_1} + \frac{d_2/2}{\lambda_2}} \tag{2.41}$$

$$h_{CD} = \frac{1}{\frac{d_2/2}{\lambda_2} + \frac{d_3}{\lambda_3} + \frac{1}{h_4} + \frac{1}{h_{56}}} \tag{2.42}$$

$$h_{DE} = h_i \tag{2.43}$$

The indices A to E denote the temperature nodes, A denoting the outdoor environment and E the interior room air temperature. h_a and h_i are the outdoor and interior heat transfer coefficients. According to the German standards DIN EN 673 and 674, they are considered to equal the constant values h_a=25 W/m^2/K and h_i=7.7 W/m^2/K (no wind velocity measurements have been performed within this thesis).

With the equations 2.40 to 2.43, applying the definition of the heat transfer coefficient $q_{ij} = (T_j - T_i) \cdot h_{ij}$, the resulting heat fluxes can be calculated with the following system of equations.

$$\dot{q}_{AB} + \dot{q}_{BC} = 0 \tag{2.44}$$

$$\dot{q}_{BC} + \dot{q}_{abs} + \dot{q}_{el} + \dot{q}_{CD} = 0 \tag{2.45}$$

$$\dot{q}_{CD} + \dot{q}_{DE} = 0 \tag{2.46}$$

$\dot{q}_{abs}$ is the heat flux due to absorption of solar radiation, which is neglected for all the layers except the silicon layer 2. The heat flux $\dot{q}_{abs}$ is equal to the absorbed power, which is a by-product of the optical simulation. Furthermore, the temperature is influenced by the PV cell operation point: if the operation point is in the first quadrant (i.e. normal operation), the electricity generated by the cell leaves the system, making $\dot{q}_{el}$ negative. However, if the operation point is in another quadrant, the cell heats up. A quantitative analysis of this effect can be found in section 4.4.

With the values T_{int} = 25°C, λ_1=λ_3=λ_5=λ_6=0.76 W/m/K, d_1=d_3=$3.2 \cdot 10^{-3}$ m, λ_2=0.212 W/m/K, d_2=$0.76 \cdot 10^{-3}$ m, d_5=d_6=$4 \cdot 10^{-3}$ m and an assumed constant heat transfer coefficient h_4=0.9 W/m^2/K for layer 4, the temperature simulation yields the results of Eqs. 2.47 to 2.49.

$$T_{front} = 0.039 \cdot (\dot{q}_{abs/C} + \dot{q}_{el}) + 0.969 \cdot T_{amb} + 0.031 \cdot T_{int} \tag{2.47}$$

$$T_{wafer} = 0.044 \cdot (\dot{q}_{abs/C} + \dot{q}_{el}) + 0.965 \cdot T_{amb} + 0.035 \cdot T_{int} \tag{2.48}$$

$$T_{back} = 0.0046 \cdot (\dot{q}_{abs/C} + \dot{q}_{el}) + 0.099 \cdot T_{amb} + 0.901 \cdot T_{int} \tag{2.49}$$

The coefficients for the wafer and the front temperature are similar, which means that the difference between them will be low (the difference here is around 1°C). For identical interior and outdoor temperatures, which is, in general, not the case for

BIPV applications, the offset in the equations disappears, and the form of Eq. 2.35 is achieved. More detailed investigations can be found in section 4.5.

2.8 Light soaking and annealing

Some thin-film PV technologies (especially amorphous silicon, but also CIS/CIGS and others) show complicated electrical behavior when exposed to variable temperature or irradiance conditions. The I–V curve of PV cells based on these technologies is not only a function of the temperature and the irradiance, but also of the condition of the material. This condition is influenced by its exposure to irradiation and/or temperature within the days (or even weeks, as for amorphous silicon) before.

It can be observed that the I–V curve of an a-Si:H PV cell deteriorates after its production when it is irradiated, which is called Staebler-Wronski effect after the authors of the first publication about the effect [60]. However, the cell I–V curve can be improved again by exposing the PV cell to high temperatures. The process of improvement, which can be accelerated by irradiation [63], is called “annealing”. Even the initial power can be achieved by exposing the PV cell to high temperatures for a certain time period, which for a-Si:H at 120°C is about 30 hours [13].

For the comparison of PV modules to others of the same technology, a “stabilized efficiency” has to be measured. For this purpose, the a-Si:H module is irradiated with a solar simulator for about two weeks while keeping the temperature in a certain range. The details can be read in the standard IEC 61646.

The metastability effect causes higher power outputs during the summer and lower ones during the winter months, compared to the simulation results. Within the simulation for this thesis, the effect is neglected, but at least for a-Si modules, a quantitative analysis is made within subsection 4.5.3.

However, the behavior of other thin-film technologies is similar. A summary of the effects has been given by M. Goldstein and L. Dunn [19], where the latest research on metastability of a-Si, CdTe, CIS/CIGS and even crystalline silicon is discussed. However, as this topic is not specific to BIPV simulations, the topic has not been addressed here in detail. The simulation process has been prepared to include variable I–V characteristic curves in the future as soon as the effects discussed in this subsection can be simulated.

2.9 Inverter and MPP tracking

The inverter of a PV system meets two demands: on the one hand, it ensures that the maximum available power is taken from the PV system by performing MPP tracking, and on the other hand, it converts direct current into alternating current, making the power available for grid connection or for local usage.

2.9.1 MPP tracking at the system level

As has already been described in section 2.6, a system I–V curve can lead to more than one local power maximum, especially when bypass and blocking diodes are involved and the irradiance distribution on the cells is inhomogeneous. However, during the time when the inverter analyzes the whole I–V curve of the first quadrant, it does not operate at the maximum power point. Former inverters restricted their analysis of the I–V curve to the range near the previous maximum power point; however, new inverters have changed their behavior to the analysis of the full quadrant which allows them to find the global maximum at every analysis step. Commonly, this approach to find the MPP in shading conditions is called "shadow MPP tracking". For the electricity yield simulation, it has to be known whether the inverter possesses this functionality.

2.9.2 Inverter losses due to the MPP voltage range

In general, the inverter requires a minimum open circuit voltage of the PV system to start operation. Most inverters define a MPP voltage range in their data sheet by the two voltages V_{min}^{MPP} and V_{max}^{MPP}. There are various inverter functionalities; in general, however, after the minimum open circuit voltage has been reached, this voltage is kept constant until the MPP voltage is higher than V_{min}^{MPP}; after that, the inverter starts the MPP tracking. Analogous behavior occurs at high voltages: if the MPP voltage would be higher than V_{max}^{MPP}, the voltage is kept constant at a value of V_{max}^{MPP}. Furthermore, if the nominal AC power of the inverter is exceeded, the output AC power is kept constant, and the inverter heats up until it derates (loses efficiency). The losses due to the MPP voltage range are discussed for the simulation of subsection 4.5.4.

2.9.3 The inverter efficiency

The power losses of the DC to AC conversion are characterised by the inverter efficiency, which mainly depends on the input power, but also on the inverter temperature, the grid voltage and the DC input voltage. In former days, only the first dependence was quantified in the data sheet by indicating the efficiencies at an input power of 10%, 50% and 100% of the nominal inverter power. Based on these values, the well-known Schmidt-Sauer model was developed [55]. As nowadays also the efficiency dependence on the input voltage is included in the data sheet, also the Schmidt-Sauer model has been refined to include the input voltage dependence [56]. The approach is summarized by the following formulas. With p_{out} being the output power relative to the nominal inverter power, the power loss fraction p_{loss} is fitted by a second-degree polynomial with the coefficients p_{self}, v_{loss} and r_{loss}:

$$\eta = \frac{p_{out}}{p_{out} + p_{loss}} \qquad p_{loss} = p_{self} + v_{loss} \cdot p_{out} + r_{loss} \cdot p_{out}^2 \tag{2.50}$$

The assumptions directly lead to the following equation for the efficiency:

$$\eta = \frac{p_{out}}{p_{out} + p_{self} + v_{loss} \cdot p_{out} + r_{loss} \cdot p_{out}^2} \tag{2.51}$$

The enhanced Schmidt-Sauer model makes the following three parameters dependent on the voltage, as indicated by the Eqs. 2.52 to 2.54:

$$p_{self} = p_{self,0} + p_{self,1} \cdot V_{DC} + p_{self,2} \cdot V_{DC}^2 \tag{2.52}$$

$$v_{loss} = v_{loss,0} + v_{loss,1} \cdot V_{DC} + v_{loss,2} \cdot V_{DC}^2 \tag{2.53}$$

$$r_{loss} = r_{loss,0} + r_{loss,1} \cdot V_{DC} + r_{loss,2} \cdot V_{DC}^2 \tag{2.54}$$

The model is applied to the inverters of the Bad Krozingen PV system and the BIPV system in the saw-tooth roof of the Fraunhofer ISE main building within the subsections 4.5.1 and 4.5.2.

3 Program descriptions

3.1 Overview

For all analyses performed within this PhD thesis, simulation programs have been written. The only external programs that have been applied are the ray-tracing program RADIANCE and the semiconductor analysis program ASA, which are both described in detail in this chapter. With the ray-tracing program RADIANCE, the 60° approach of Eq. 2.16 has been validated for vertical PV module orientations. Furthermore, the applicability of the separation between the simulations of sky radiance distribution and the optical simulation of the surroundings of the BIPV system, as described in subsection 2.2.5, has been analyzed. Also the importance of considering reflections from neighboring buildings as well as considering the reduction of the ground albedo due to shading for the simulation of the irradiance on the PV cells are analyzed with the help of RADIANCE. With the semiconductor simulation program ASA, the two-diode model to simulate the low-light behaviour of amorphous silicon PV cells has been validated. Both programs, RADIANCE and ASA, will be presented in detail in this chapter. In general, great effort has been made to base the program structure on command lines. With the large number of lines and columns in text files, imports into programs with an extended graphical user interface have to be avoided. Furthermore, the level of automation can be increased when the programs are based on a command line structure. Most of the steps of the methodology are performed with programs developed by the author of this thesis. Their program structure will not be described in detail, as the fundamental calculation methods are described in the respective sections of chapter 2.

RADIANCE is a ray-tracing program. It is applied to improve the irradiance calculation for BIPV systems with complex surroundings or shading structures. The second program, ASA (Advanced Semiconductor Analysis), is applied to analyze the I–V curves of PV cells based on thin-film PV technologies under variable temperatures and irradiances. Within this PhD thesis, ASA is applied to validate the two-diode model for an a-Si:H PV cell; in this way, the low-light behavior of the PV cell can be analyzed without taking metastability effects into consideration. Furthermore, the ASA program can help to perform a system-based optimisation of material or layer properties to maximize the system's electricity yield under realistic operating conditions instead of optimizing these properties to maximize the PV cell efficiency under standard test conditions (STC).

3.2 The program RADIANCE

3.2.1 General information

The parts of the methodology shown in Fig. 2.1 that require ray-tracing calculations are performed with the Linux-based backward ray-tracer (see subsection 2.2.4) RADIANCE. It was written by Greg Ward at the Lawrence Berkeley National Laboratory (LBNL), mainly for architects and lighting engineers for daylight simulations in buildings, and can be downloaded free of charge at [49] including the C source code of the software. As a consequence, many people work simultaneously on improving the program. The main advantage of RADIANCE is its structural design: it mainly consists of shell commands written in the C programming language that can be automated easily by shell scripting. However, the learning curve for the program related to programs with a graphical user interface is quite flat.

As the program is already described in detail in [33] and in many tutorials that are available online, the following section gives only a very brief overview. The description is restricted to the parts of the program that are important to understand the challenges for the BIPV electricity yield simulation that arise from the basic assumptions of the ray-tracing program. Furthermore, the description of the RADIANCE commands including the most important program options will be important for the next chapter of this thesis, especially for the tradeoff between the calculation time of the irradiance simulation and its accuracy.

In accordance with the name of the program, the calculations are based on radiometric units (see subsection 2.2.1). For daylight simulations, most of the programs can translate the radiometric into photometric quantities, which makes it possible to perform parallel simulations of the BIPV electricity yield and photometric calculations, like daylight or glare simulations of buildings.

3.2.2 Material description

The RADIANCE program works only with surfaces, not with solid objects. This is not a problem for objects where only the reflection or total absorption is important. However, the calculation of the absorbed fraction of light becomes difficult for transmitting materials. Optical properties of solid objects that appear within the geometry are not defined by a real or complex refractive index. Instead, every surface is defined by derived values like reflectance, transmittance or specularity (the latter is defined as the photometric ratio of the direct fraction of the reflected light to the total reflected light). Objects with different optical properties on the front and the back surface can be defined by using two surfaces with different properties in the simulation.

In RADIANCE, spectral effects can only be simulated by changing these parameters for every considered wavelength. For the photometric daylight simulations, three parallel calculation channels exist to perform simulations with RGB values (one parameter each for the red, green and blue regions of the visible spectrum when it is divided into three parts). These three channels could be taken for a parallel calculation of three different wavelengths; for general spectral investigations, the material parameters have to be changed for every wavelength. However, the computer structure of RADIANCE is not optimized to changing material parameters within a shell script, which would make the calculations quite slow.

There are many material types in RADIANCE; this description will focus on those that are important for the irradiance simulation within a BIPV electricity yield simulation. For complex BIPV geometries, the transparent materials are essential, as described in subsection 3.2.9. The material *dielectric* (RADIANCE material and command names are italicized within this thesis to avoid confusion) allows the analysis of light refraction at smooth surfaces, including the phenomenon of total reflection.[1] As the optical material properties in general, however, are not characterized by complex refraction indices in RADIANCE but by reflectance and transmittance, also the material properties of light refraction and absorption are defined by externally given values. The material *dielectric* needs two quite unphysical input parameters: a ”refractive index” that tells the program the angular change of the light path in air on entering the material, and a value named ”transmission” that contains the information about the fraction of light transmitted by the surface. The absorbed fraction is calculated by analyzing the path length of the light through the material, dependent on the incident angle. This means that every ray that passes a surface with the material *dielectric* has to pass a second surface with the same material property; otherwise, the light path remains refracted during the further calculation. The geometry has to be defined carefully to ensure that this problem is avoided.

dielectric also belongs to the category of materials that are orientation-dependent. With this orientation, which is read from the spatial object definition (objects are defined by the coordinates of their corners, and their sequence defines the orientation), the program decides in which direction the rays are refracted. If the geometry is analyzed inside a transparent object, the distance of the chosen grid point to the first *dielectric* surface is the basis for the calculation of the absorbed fraction of light. The material *dielectric*, however, is not applicable for analyzing rough surfaces. For rough as well as transparent surfaces, the material *trans* is available. The latter has not been applied within this thesis. (However, for example, the simulation of a PVShade® BIPV module with partially transparent photovoltaic stripes could only be simulated with the *trans* material. See subsection 4.4.2.) Furthermore, materials with a special reflection or transmission behavior can be created by the user by importing measurement data.

The material *dielectric* only works when the adjacent surroundings have a refractive index of 1. If an assembly of two optically different materials in optical contact

[1] The names of the material types are not always chosen very well. In fact, the name often implies physical behavior that has nothing to do with the special features of the material type.

with each other has to be simulated, the material *interface* (partially) solves the problem. The material parameter "refractive index" again defines the ray direction, but this time, already refracted ray paths can be simulated. The *interface* surface, which is also direction-dependent, always has to be between two *dielectric* surfaces to keep the calculation valid. However, also the *interface* material does not have the possibility to simulate rough surfaces.

The third material of major importance that can simulate transmission is *glass*. It was written to shorten the calculation times that often explode when a geometrical configuration with many *dielectric-dielectric* surface definitions is analyzed, due to the simulation of internal reflections. *glass* avoids these calculations. For complex BIPV systems, this material is applied to simulate windows of buildings from the surroundings or to define the third glass pane in a BIPV triple glazing unit.

For non-transparent materials, roughness as well as specularity can be simulated with the material type *plastic*.[2] Three parameters define the object properties: "reflection", "roughness" and "specularity".

Light sources in RADIANCE are also treated as surfaces with material properties, with the exception of the sky, that is defined only by the angular direction (this is done by the *source* command, the only exception from the definition of the geometry by surfaces). With *light*, *spotlight* and *glow*, three "material" types define the light sources. Within the simulation, and corresponding to the standard procedure, the material *light* is applied for the direct sunlight, while the material *glow* defines the diffuse sky.[3]

3.2.3 The simulation of the sky radiance distribution

Besides the definition of materials and objects, the sky radiance distribution has to be calculated for every chosen time step. A short description of the Perez model can be found in subsection 2.2.3. Here, the RADIANCE programs that allow the sky to be simulated according to the mentioned models are described.

The main calculations are performed by the program *gensky*. Given a month, day, time of day, and the position on earth in longitude and latitude coordinates including the time zone, the program calculates the local solar time, the solar azimuth and altitude. The program neglects the change of the sun's position from year to year; this results in a small error that can be important for concentrating PV cells, but not (yet) for BIPV applications. *gensky* also simulates the sky radiance distribution according to the CIE sky luminance standard S011/E:2003. Depending on the chosen

[2] This material type, despite its name, can be applied for all rough objects that are non-transparent.

[3] According to the convention within the program, the *glow* material increases the ambient bounce value by 1. This takes into account that the diffuse part of the sky radiation has already been scattered. For the definition of the ambient bounce value, see subsection 3.2.6. In common RADIANCE simulations, this convention allows a separation of the direct sunlight analysis (*light* material, –ab=0) from the impact of the diffuse sky (*glow* material, –ab=1) by performing ray-tracing analyses with zero and one ambient bounces, respectively, and comparing both results afterwards.

program options, a sunny, cloudy, uniform or intermediate sky can be simulated in either radiometric or photometric units. The other RADIANCE subprogram called *gendaylit* processes a pair of measured sky irradiance data – see subsection 2.2.3 – to a Perez sky radiance distribution. The user has the choice between the following input formats: direct-normal irradiance and diffuse-horizontal irradiance (for most of the American weather databases), global-horizontal irradiance and diffuse-horizontal irradiance (for European databases like DWD and Meteonorm), and also photometric measurement data (illuminance values) can be forwarded to the program. Both commands, *gensky* and *gendaylit*, produce sky definitions in RADIANCE format that can be forwarded directly to perform the ray-tracing calculations.

3.2.4 Sky discretisation

For some applications (see e.g. the approach described in section 2.2.5), discretisation of the simulated sky radiance distribution is necessary. One approach is to choose sky regions with a similar solid angle. Within the so-called Tregenza sky discretisation originally developed to accelerate daylight simulations [62], 145 sky regions with similar solid angles were defined according to Fig. 3.1 (left side). A later extension implemented by Christoph Reinhart allows simulations to be made with a finer sky discretisation. The example of 577 sky regions is shown on the right side of Fig. 3.1.

Furthermore, every method of sky discretisation has to find a way to deal with the direct sunlight. In the presented approach, the sun is divided into the neighboring three sky regions while the sun radiance value is separated into three components according to the distance to the center of the three sky regions. These calculations are carried out by the RADIANCE program *genskyvec*. The approach leads to solid angles of the sun that are significantly too high. As a consequence, the shading and penumbras show significant deviations, which are analyzed quantitatively in subsection 4.2.4.

3.2.5 Definition of the investigated geometrical configuration

RADIANCE has its own format to define the geometrical configuration of the situation which is to be analyzed. It is based on simple text files with the extension .rad. Although there are many help programs to define the object surfaces (like *genbox*, *gensurf* or *xform*), it is still quite complicated and time-consuming to define the geometrical configuration by typing text files. In the meantime, transformations from different 3D modeling tools have been implemented. The geometrical configuration can be defined with the programs Rhinoceros, Sketchup or EcoTect and will be transformed automatically into .rad files that can be further processed with RADIANCE. Every object surface is defined by its dimensions, direction and material type. The definitions of the material properties, including the "material" definitions of the sky, are summarized in another file format called .mat files. The

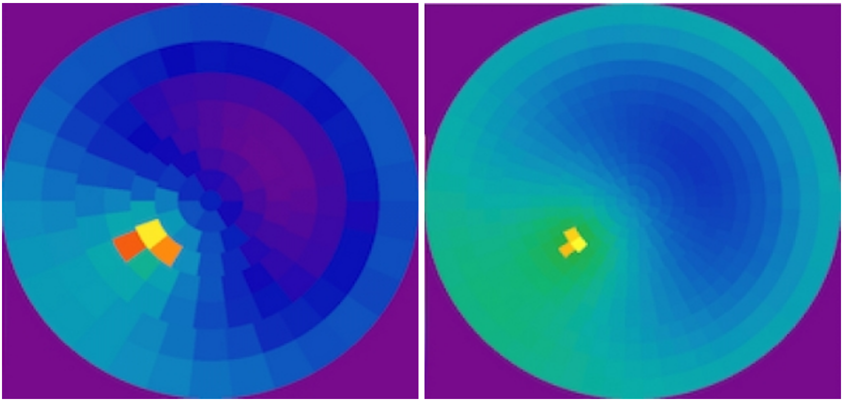

Figure 3.1: Stereographic fish eye projection of the sky hemisphere, with the sky radiance distribution simulated according to Perez (bottom: southern, left side: eastern direction). Left: the Tregenza sky discretisation, right: the Reinhart extension to finer sky resolutions (here, the sky is divided into 577 sky regions). To depict the direct sunlight distribution, a sunny day was chosen. Both graphs show the sun position of April 21^{st} at 10 a.m. Source: [26]

sky simulation, the dimensions of the geometrical configuration and the material properties are summarized in RADIANCE by creating a so-called octree file. This octree includes all geometrical information that is needed to perform the ray-tracing calculations and is saved in machine-readable format. The octree is created from the geometry files by the *oconv* command that summarizes all the definitions of the geometry in one file.

3.2.6 The rendering procedure

The creation of the octree file represents the final step of the geometrical definition; every ray-tracing procedure is based on an octree file. The basis of the programs described in the following lines is the *rtrace* command. By defining a grid point including a direction, *rtrace* calculates either the radiance of the object located in the view direction (program option $-I-$), or it reproduces the total irradiance incident on the given grid point from the hemisphere defined by the given direction (program option $-I+$). Both calculations follow the same concept: from every intersection point of a ray with an object, a pencil of rays is sent out to analyze the radiance values of their directions. With the $-I-$ option, this procedure starts at the first object that is located in the view direction, with the $-I+$ option, the procedure starts immediately at the grid point.

The accuracy as well as the duration of the calculation strongly depends on the number of ambient bounces ($-ab$). This is the number of steps in the calculation at which new bundles of light are sent out from the intersection point of one view ray and another object. An ambient bounce value of zero means that only light that directly hits the grid point is considered; if the value is one, then the light that only needs one reflection to reach the grid point is also considered. The number of rays within a bundle of light is defined in the $-ad$ (ambient division) program option. To shorten the calculation time, RADIANCE analyzes the difference between the radiance values at two neighboring intersection points and omits the radiance calculation for an intermediate intersection point if the difference (related to the ambient accuracy $-aa$) and the distance (related to the ambient resolution $-ar$) is small enough. This method of increasing the calculation speed is called "ambient caching".

In RADIANCE, images are rendered by the program *rpict* which is based upon the $-I-$ option of *rtrace*. Assuming an image of the geometry in a certain view direction that has defined dimensions, the radiance value of every pixel of the image corresponds exactly to the results of the *rtrace* $-I-$ command if the view direction equals the direction from the viewer through the pixel of the image. *rpict* creates the ray directions that correspond to the image dimensions, saves the radiance value for every pixel and returns either a table of the radiance values or the same values in a machine-readable image format that can be opened with the RADIANCE program *ximage*. To do so, *rpict* needs detailed information about the dimensions of the image to determine the ray directions. The most important image properties are the x/y resolution and the angle of beam spread in both dimensions; furthermore, the image can be in rectangular or in fish-eye view format, parallel or perspective, the fish-eye view can be in equidistant, orthographic or stereographic projection, and so on. These properties, including the view direction, define the ray directions that are necessary for the simulation of the radiance values for every pixel. The ray directions can also be calculated by the program *vwrays*, which means that the *rpict* command does nothing else than combining *vwrays* with *rtrace*.

3.2.7 Incidence angle dependence

As already discussed in section 2.4, the analysis of the incidence angle dependence can be important for BIPV applications, especially when they have an internal structure or if reflecting components of the BIPV element or the surroundings have to be taken into account. These simulations can be done with the program RADIANCE by carrying out the following procedure, which has been developed within this thesis. For the comparison to other approaches, see section 2.4 and subsection 4.2.5.

Images are rendered by sending out view rays from a defined grid point in the direction of every pixel of the image. These directions are defined by the view file. In Fig. 3.2 (left side), an image rendered as an equidistant fish-eye view is shown. This projection follows the simple relation presented in Eq. 3.1.

$$r = f \cdot \theta_P \tag{3.1}$$

r is the distance of the pixel from the center of the image, θ_P is the incidence angle of the light coming from the pixel, and f is the focal length of the camera that represents the proportionality factor. Compared to the stereographic projection, following the relation $r = 2f \cdot \tan(\theta_P/2)$, and the equi-solid-angle fish-eye projection, following the relation $r = 2f \cdot \sin(\theta_P/2)$, the equidistant fisheye projection allows the incidence angle to be read directly from the distance to the image center.

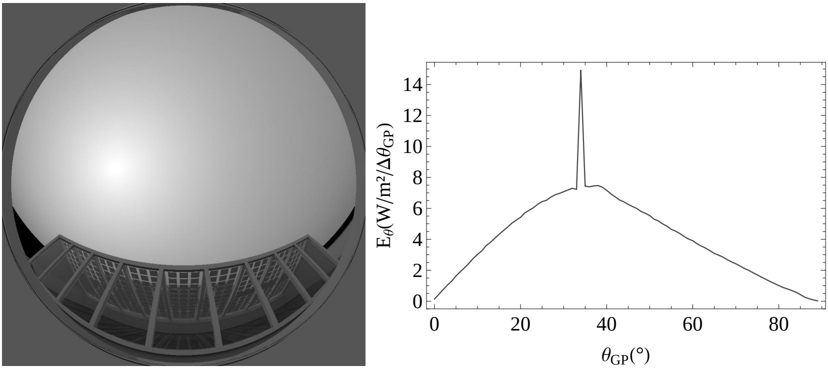

Figure 3.2: Left: Equidistant fisheye view from the external glass surface of a BIPV module in the saw-tooth roof of the Fraunhofer ISE main building. The sky (chosen point of time: May 5^{th}, 10 a.m.) is rendered according to the Perez model. For every pixel of the image, the distance to the center is proportional to the incidence angle of the light. Pixels outside the 90° circle represent the light coming from the back of the PV module. Right: Incidence angle dependence of the irradiance, calculated from the data set represented by the image on the left.

If the radiance values resulting from the rendering process are not saved in an image format but in a table, the irradiance dependence on the incidence angle can be calculated by multiplying all radiance values with the solid angle corresponding to the view ray and summing up all of the products that belong to a certain incidence angle range, as shown in Eq. 3.2.

$$E_{\theta_{GP},GP}(t) = \sum_{p \in \theta_{GP}} L_p(t) \cdot \Omega_p \cdot \cos\theta_{GP} \tag{3.2}$$

θ_{GP} represents the range of incidence angles taken into account for the irradiance E. Within the simulations of this thesis, $\Delta\theta_{GP} = 1°$ has been chosen. GP stands for grid point, as the irradiance can be inhomogeneous on the BIPV surface and therefore has to be calculated for a certain number of grid points. The number of chosen grid points depends on the one hand on the geometry and the chosen number of sky regions, on the other hand on the size of the PV cells and their connection within the PV modules, and will therefore be discussed in the subsections 4.2.4 and 4.5.2.

The result of applying Eq. 3.2 to the radiance values that correspond to the rendered image in Fig. 3.2 (left side) is shown on the right side. In this case, there are no reflections of the direct sunlight, which is the most frequent case. The incidence angle dependence can also be handled according to Eq. 2.16.

Related to Eq. 3.2, a definition problem occurs that should be discussed here. The term L stands for radiance and has the unit W/m^2/sr, while E, the irradiance, has the unit W/m^2. For values with the unit W/m$^2/\theta_{GP}$, like $E_{\theta_{GP}}$, no term exists. According to the symmetry of the Eq. 3.2 to the irradiance definition given in Eq. 2.4, and also considering the fact that W/m^2 means nothing else than W/m^2/hemisphere, the term irradiance is also used for it in this PhD thesis.

3.2.8 rtcontrib and the calculation of the transfer functions

In 2010, a new RADIANCE subprogram called *rtcontrib* was developed by Greg Ward [26]. It allows *rtrace* calculations to be made with specific light sources within the same octree file. As an example: If the geometry has two light sources, *rtcontrib* can render images only by considering one of them. Combining the two *rtcontrib* results for the two light sources with the picture adder *pcomb*, the same image appears as if *rtrace* had been applied. If the same calculations had been done with *rtrace*, it would have been necessary to change the geometry file first by removing one of the two light sources.

The advantages of *rtcontrib* are especially relevant for the sky discretisation. If the sky is divided into N regions, this corresponds to N different light sources. Therefore, the program fits perfectly for the approach to shorten the calculation time described within subsection 2.2.5.

Until now, when applying *rtcontrib*, only the Tregenza/Reinhart sky discretisation shown in subsection 3.2.4 has been implemented. For shorter calculation times, an implementation of a sky discretisation that is finer at the possible sun positions over the year and more rough at the diffuse parts of the sky is essential.

Such sky discretisations are already available within the RADIANCE-based software *daysim* [10] that is mainly applied for photometric calculations. The transfer should not be very difficult but has not been done within this thesis.

The main idea to reduce the calculation time has already been explained in subsection 2.2.5. With the procedure described in subsection 3.2.7, the approach can be extended to include the incidence angle dependence of the irradiance. First, the impact of a single sky region with a constant radiance of 1 W/m^2/sr on the incidence angle dependent irradiance is calculated, which is described in Eq. 3.3. These impacts are called transfer functions (TF).

$$TF^{i}_{\theta_{GP},GP} = \sum_{p\in\theta_{GP}} L^{i}_{p,rel} \cdot \Omega_p \cdot \cos\theta_{GP} \tag{3.3}$$

The transfer functions represent the irradiance on a grid point as a function of incidence angle if one single sky region with the radiance of 1 W/m^2/sr is switched on and the rest of the sky is "switched off". The decisive difference to Eq. 3.2 is the time independence of the radiance values $L_{p,rel}$. The index *rel* denotes their relation to the standardisation of the sky region radiance, which means that the unit of the transfer functions is (W/m^2)/(W/m^2/sr)=sr.

Again, the pixel data rendered by *rtcontrib* that are needed to calculate one transfer function can also be saved in a RADIANCE image format. Fig. 3.3 (left side) shows this pixel data for the calculation of the transfer function with the arbitrary number 1137 (for a chosen number of sky regions of 2305[4]), with the same geometry as rendered in Fig. 3.2. On the right side, the transfer function itself is depicted.

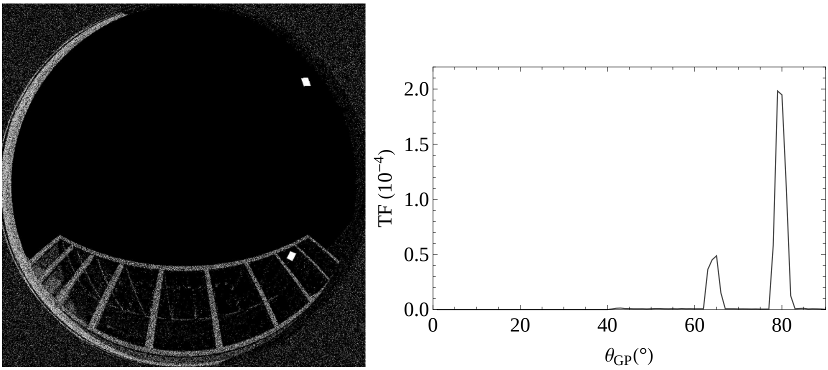

Figure 3.3: Left: Rendered radiance values, here saved in a highlit image format for demonstration, that are then processed into a transfer function by Eq. 3.2. A sky discretisation of 2305 sky regions has been chosen; the highlit sky region is no. 1137. Note that the depicted hemisphere does not show the whole sky due to the tilt of the PV surface; thus, the analyzed sky region may not be visible if located behind the PV module containing the viewing sensor. Right: Transfer function (TF) no.1173. Incidence angle dependence of the irradiance per radiance of the sky region, calculated from the pixel radiance values in the left image. The higher peak corresponds to the bright sky region no. 1137, the lower peak is caused by the reflection shown in the left image.

After the calculation of the transfer functions, the irradiance as a function of incidence angle can be calculated for every time step by Eq. 3.4. The time-independent transfer functions are multiplied by the time-dependent radiance value of the sky region i for every time step. As this is only a matrix multiplication, the calculation time becomes much shorter than when performing the ray tracing for every time step.

$$E_{\theta_{GP},GP}(t) = \sum_{i=1}^{N} TF_{\theta_{GP},GP,i} \cdot L_i(t) \tag{3.4}$$

[4] The counting starts in the north and follows the azimuthal direction before increasing the altitude angle.

As mentioned before, the radiance values corresponding to the sky regions can be calculated by the RADIANCE program *genskyvec*.

Within this thesis, the incidence angle dependence is analyzed for situations with one single sensor. Under shading conditions, there are significant disadvantages that are caused by the relatively wide penumbra, as has been shown in subsection 4.2.4. Furthermore, if more than one grid point is considered in a given geometry, the RADIANCE program performs more than one simulation simultaneously, which is not yet possible with the described methodology. For the simulations on system level, the irradiance simulations are performed with the approach of subsection 2.4.3. However, the simulations show very good agreement between both approaches, which is demonstrated in subsection 3.2.7.

3.2.9 Rendering inside the material

Within this subsection, the possibilities are discussed of applying RADIANCE for ray-tracing calculations inside a material. Due to the internal structure of the computer program, RADIANCE is not able to perform ray-tracing simulations after only one *dielectric* interface. An algorithm is presented to find the right irradiance values based on those calculated by RADIANCE.

Considering complex BIPV façades like PVShade, the possibility to perform ray-tracing analyses also inside the material would greatly extend the possibilities of a BIPV electricity yield simulation tool based on a ray-tracing program. The idea is to combine the optical analysis of the BIPV system surroundings with the optical analysis needed to characterize the internal structure of the BIPV elements.

As mentioned before, RADIANCE only works with surfaces, not with solid objects. Absorption therefore is calculated by the distance a ray travels from one *dielectric* surface to the next, while one surface alone defines the refraction of light. After having analyzed the irradiance simulation output for a normally incident light source of small diameter after only one *dielectric* material with a constant refraction index of 1.5, it can easily be discovered that the calculated irradiance values are about double too high. This deviation appears only for the specular (direct) calculation, not for the ambient one (see subsection 2.2.4 for details). However, to the author's knowledge, the approach presented in the following part has not been published elsewhere. Remembering that the rays are followed backwards in RADIANCE, it becomes clear that the definition of the bundle of light rays sent out from the grid point is independent of possible refraction of the rays afterwards. Therefore, for the direct path, the irradiance calculation is wrong when performed inside the material. It should follow Eq. 3.5, according to the definition given in Eq. 2.4:

$$E = \int_{2\pi} L \cos\theta_m d\Omega = \int_{\Delta\phi_m} \int_{\Delta\theta_m} L \cos\theta_m \sin\theta_m \, d\theta_m d\phi_m \qquad (3.5)$$

The index m indicates the location inside the material. L is restricted to the light source normally incident to the *dielectric* surface and is zero everywhere else. Due to backward ray tracing, the density of rays giving the radiance values $L(\theta_m, \phi_m)$ remains constant when the angles are transformed as follows.

With the equations

$$L(\theta_m, \phi_m) \to L(\theta, \phi) \tag{3.6}$$

$$\sin\theta_m = \frac{n_1}{n_2} \cdot \sin\theta \tag{3.7}$$

$$d\phi_m \to d\phi \tag{3.8}$$

and the partial derivative

$$\frac{d\theta_m}{d\theta} = \frac{d}{d\theta}(\arcsin(\frac{n_1}{n_2} \cdot \sin\theta)) = \frac{n_1}{n_2} \frac{\cos(\theta)}{\sqrt{1 - \frac{n_1^2}{n_2^2} \cdot \sin^2(\theta)}} \tag{3.9}$$

the calculation of the irradiance can be rewritten by substitution into:

$$E = \int_{\Delta\phi} \int_{\Delta\theta} L(\theta, \phi) \cdot \sqrt{1 - \frac{n_1^2}{n_2^2} \cdot \sin^2(\theta)} \cdot \frac{n_1}{n_2} \sin(\theta) \cdot \frac{n_1}{n_2} \frac{\cos(\theta)}{\sqrt{1 - \frac{n_1^2}{n_2^2} \cdot \sin^2(\theta)}} d\theta d\phi = \tag{3.10}$$

$$\int_{\Delta\phi} \int_{\Delta\theta} L \cdot \frac{n_1^2}{n_2^2} \cdot \cos(\theta) \sin(\theta) d\theta d\phi = \frac{n_1^2}{n_2^2} \int_{\Delta\Omega} L \cdot \cos(\theta)\, d\Omega \tag{3.11}$$

Fig. 3.4 shows the application of the ray-tracing calculations within the material using the correction factor n_1^2/n_2^2. A single *dielectric* surface is placed at a position of 70 *mm* in the direction of the light source. Then, the irradiance values are calculated for several sensor positions behind and in front of the *dielectric* surface. For standard glass with an assumed constant refractive index of 1.5, the correction factor has the value $1/n_{glass}^2 = 0.444$. On the left-hand side of Fig. 3.4, the application of the correction factor to the irradiance results behind the *dielectric* surface is shown. The right-hand side compares the incidence angle dependence of the irradiance just before and just after an air-glass intersection, which is calculated with the ambient path of the ray-tracing procedure.

For the ambient calculation, the results are correct without applying the correction factor, as demonstrated on the right side of Fig. 3.4. Assuming a constant sky radiance of 1 W/m^2/sr, the integral over the red curve gives the result 3.14159 W/m^2, which equals the π value. The integral over the blue curve can be compared with that of the

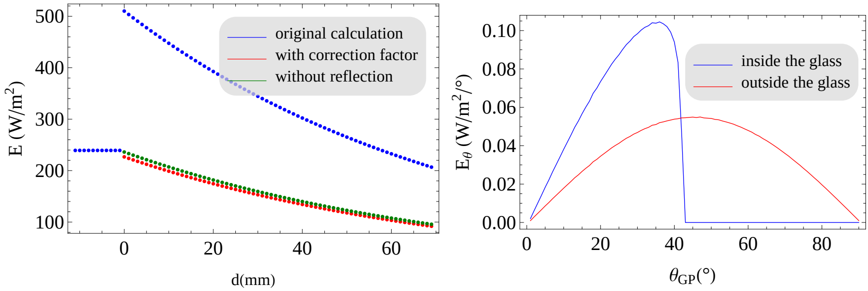

Figure 3.4: Analysis of the ray-tracing results for sensor points inside a material. Left: A light source that is simulated with the "direct" calculation in RADIANCE, normally oriented to a *dielectric* surface; irradiance values after the *dielectric* surface located at d=0 mm. Depicted are the original values without the correction factor, with the correction factor and after multiplying by $1/0.96$ to account for the reflection loss. The chosen glass absorption corresponds to an exponential decay factor of α=12.83 m^{-1}. Right: The same air-glass interface analyzed with a simulated sky of constant radiance (which belongs to the ambient calculation), with the irradiance dependence on the incidence angle just before and just after the air-glass interface.

red curve after multiplying the latter with an angular response curve. Choosing the result of the Martin and Ruiz model, depicted in 2.5, the latter gives a total of 2.965 W/m^2. However, the RADIANCE calculations are not spectrally resolved. Applying the Fresnel equations of Formula 3.16 with a constant refractive index of $\tilde{n} = 1.5$, the total gives 2.845 W/m^2, while the integral over the blue curve yields 2.811 W/m^2. The deviation may arise from the chosen resolution of $x/y = 2048$.

As has been mentioned in subsection 2.4.4, the optical simulation of the internal structure of PVShade® requires a ray-tracing procedure that starts inside the material. For this case, applying the rtcontrib procedure of subsection 3.2.8 does not require any direct calculation path (the sun's radiance is distributed among the three adjacent sky regions). To visualize the raytracing calculation, however, the whole sky is considered in Fig. 3.5, and a point of time without any direct sunlight is chosen.

The two rendering results show that the refraction of light by transmission is considered as well as the total reflection coming from the front glass-air interface, especially visible outside the central circle. Inside this circle, the whole external hemisphere is visible, including the ground, which is represented by a *plastic* material with an albedo of 0.2. The outer circle that touches the edges of the image marks the edge of the front glass pane. The optical details like chosen material parameters and grid point density are discussed within subsection 4.4.2.

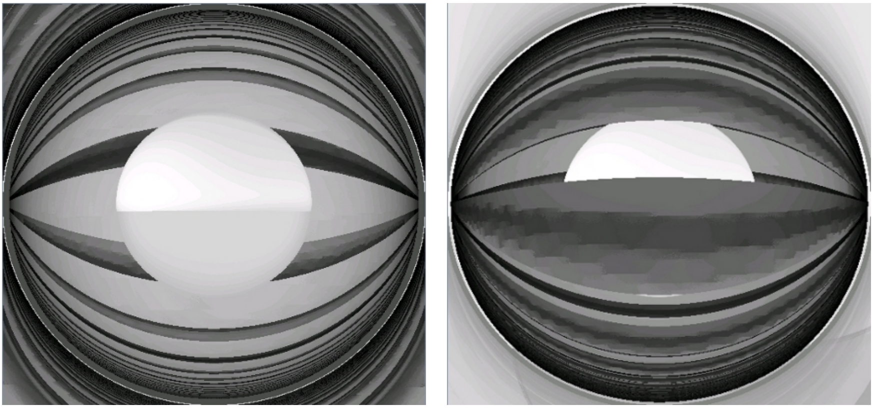

Figure 3.5: Visualized ray-tracing results from the optical simulation of PVShade®, in equidistant fisheye projection, following Formula 3.1. Left: Simulation for the thin-film layers in the front plane. Right: the same simulation for the back plane. The grid points chosen for these demonstration images are located just in front of the glass-TCO interface of a PV cells in the center of the BIPV module (see Fig. 2.6).

3.3 The program ASA

ASA, an acronym for Advanced Semiconductor Analysis, is a computer program that performs a detailed optical and electrical analysis of thin-film as well as crystalline silicon cells and has already been adapted for other PV technologies like CIGS. It was developed by Prof. Miro Zeman and others at TU Delft.

The physical approach of the program is described in a manual that can be downloaded online [67, 3]. However, it is briefly summarized in the following pages. On the one hand, the ASA program performs the optical simulation of a PV cell to calculate the number of absorbed photons in all the photovoltaic layers that comprise the PV cell. For flat interfaces, the Fresnel equations are applied; those interfaces can be calculated with or without considering coherence. Propagation of light scattered at rough interfaces is assumed to be incoherent. When the ratio of diffuse to specular reflectance of an interface is known, the program can also perform semi-coherent calculations. For the electrical simulation, on the other hand, the number of generated electron-hole pairs can be analyzed in multiple layers. After having solved the semiconductor equations by applying the Fermi-Dirac statistics for the occupation of energy levels, and assuming various models for the different recombination loss mechanisms, all relevant electrical parameters and functions, including the I–V curve, can be calculated. Within this thesis, the program is applied to validate the two-diode model for PV cells based on amorphous silicon, as described in subsection 4.3.1. Furthermore, it may offer the possibility of analyzing the spectral impact on the electricity yield of BIPV systems. Originally, an extension of the optical part to variable incidence angles was planned to analyze the angular response of thin-film PV cells and modules; however, this work is still in progress. As soon as this feature is added to the program, the optimisations of the material could be oriented toward the maximal annual electricity yield instead of the cell efficiency under standard test conditions. For this goal, also more detailed spectral data has to be collected, as described in section 2.3.

3.3.1 Description of the optical simulation within ASA

With the ASA program, the calculation of the number of absorbed photons is based on a defined spectral density function for the incident power, usually the AM1.5 global spectrum. It therefore depends on a spectral function, not only on a radiometric value. This allows the optical simulation of coherence in thin-film layers. For the solar spectral range, the coherence length is about 1 μm; for layers with a thickness less than the coherence length, interference effects have to be considered. The importance of interference effects is also dependent on the roughness of the interface (the scattering angle of the transmitted or reflected light influences the optical path through one layer).

Layers with flat interfaces

If Snell's law can be applied for the interface transmission, and the angle of incidence equals the angle of reflection for the interface, the straight-forward approach described in the following lines is applied. This is the case for flat interfaces. Besides the ASA manual [67], the following analytical approach can also be found in many textbooks, such as [24] and [6].

The reflection and transmission at a flat interface for normally incident light is calculated according to Eq. 3.12 and 3.13, independent of its polarisation. As the direction of the reflected and transmitted light fractions are opposite, the sum $\tilde{r}+(-\tilde{t})$ equals 1, that means, the sign denotes the direction of the light. The ˜ indicates that the variable is a complex number.

$$\tilde{r} = \frac{\tilde{n}_0 - \tilde{n}_1}{\tilde{n}_0 + \tilde{n}_1} \qquad \tilde{t} = \frac{2\tilde{n}_0}{\tilde{n}_0 + \tilde{n}_1} \tag{3.12}$$

$$R = |\tilde{r}|^2 = \left| \frac{\tilde{n}_0 - \tilde{n}_1}{\tilde{n}_0 + \tilde{n}_1} \right|^2 \qquad T = 1 - R \tag{3.13}$$

$\tilde{r}$ and $\tilde{t}$ are called the Fresnel coefficients; the optical properties of the materials before and after the interface are described by the complex refractive indices $\tilde{n}_0$ and $\tilde{n}_1$. For incidence angles different from zero, a separation of the calculations for s and p polarisation is required. Within ASA, this is done with effective refractive indices, as defined in Eq. 3.14. The angles θ_0 and θ_1 are related by Eq. 3.15.

$$\tilde{n}_{is,\mathrm{eff}} = \tilde{n}_i \cos\tilde{\theta}_i \qquad \tilde{n}_{ip,\mathrm{eff}} = \tilde{n}_i / \cos\tilde{\theta}_i \qquad i = 0,1 \tag{3.14}$$

$$\tilde{n}_0 \sin\tilde{\theta}_0 = \tilde{n}_1 \sin\tilde{\theta}_1 \tag{3.15}$$

Even when the incident radiation is assumed to be unpolarized, both the parallel and perpendicular components have to be analyzed; after that, the arithmetic mean is calculated, as described in Eq. 3.16.

$$R = \frac{1}{2}(R_s + R_p) = \frac{1}{2}(|\tilde{r_s}|^2 + |\tilde{r_p}|^2) = \frac{1}{2}\left(\left|\frac{\tilde{n}_{0s,\mathrm{eff}} - \tilde{n}_{1s,\mathrm{eff}}}{\tilde{n}_{0s,\mathrm{eff}} + \tilde{n}_{1s,\mathrm{eff}}}\right|^2 + \left|\frac{\tilde{n}_{0p,\mathrm{eff}} - \tilde{n}_{1p,\mathrm{eff}}}{\tilde{n}_{0p,\mathrm{eff}} + \tilde{n}_{1p,\mathrm{eff}}}\right|^2\right) =$$
$$\frac{1}{2}\left(\left|\frac{\tilde{n}_0 \cos\tilde{\theta}_0 - \tilde{n}_1 \cos\tilde{\theta}_1}{\tilde{n}_0 \cos\tilde{\theta}_0 + \tilde{n}_1 \cos\tilde{\theta}_1}\right|^2 + \left|\frac{\tilde{n}_0/\cos\tilde{\theta}_0 - \tilde{n}_1/\cos\tilde{\theta}_1}{\tilde{n}_0/\cos\tilde{\theta}_0 + \tilde{n}_1/\cos\tilde{\theta}_1}\right|^2\right), \qquad T = 1 - R \tag{3.16}$$

On this basis, the optical calculation of a layer (two interfaces) can be performed. First, if the interface after the layer is neglected, the spectral photon flux decreases exponentially within an absorbing material, as described by the Beer-Lambert law (Eq. 3.17).

$$\Phi(x,\lambda) = \Phi_0(\lambda)\exp[-\alpha(\lambda)x] \tag{3.17}$$

The absorption coefficient $\alpha(\lambda)$ is related to the imaginary part of the complex refractive index $\tilde{n} = n + i\kappa$ according to Eq. 3.18.

$$\kappa = \frac{\alpha\lambda}{4\pi} \tag{3.18}$$

The absorption within the material can be calculated by the attenuation of the spectral photon flux, shown in Eq. 3.19.

$$\hat{A}(x,\lambda) = -\frac{d}{dx}\Phi(x,\lambda) = \Phi_0(\lambda)\alpha(\lambda)\exp[-\alpha(\lambda)x] = \alpha(\lambda)\Phi(x,\lambda) \tag{3.19}$$

A is the absorption in the material, the caret indicates the spectral dependence. Formula 3.20 shows the direct dependence of the electron-hole pair generation rate inside the photovoltaic layers on the photon absorption.

$$G_{opt}(x) = \int_{\lambda_1}^{\lambda_2} \eta_G\, \hat{A}(x,\lambda) = \eta_G A(x) \tag{3.20}$$

In most cases, the quantum efficiency of generation η_G can be considered to equal 1 for all wavelengths. If the energy of the photon is higher than the band gap, the energy difference will lead to a temperature increase of the layer that absorbed the photon.

If the second interface of the thin-film layer is considered, reflections between the first and second interface lead to a geometric series within the optical simulation (Eq. 3.21). The situation is depicted in Fig. 3.6.

$$\sum_{k=0}^{\infty} q^k = \frac{1}{1-q} \qquad \forall |q| < 1 \tag{3.21}$$

By considering the phase of the electromagnetic waves, the geometric series leads to the following Fresnel coefficients for the layer in total:

$$\tilde{r}_{\text{layer}} = \tilde{r}_1 + \frac{\tilde{t}_1 \tilde{t}_1' \tilde{r}_2 \exp[-2i\tilde{\delta}_1]}{1 - \tilde{r}_2 \tilde{r}_1' \exp[-2i\tilde{\delta}_1]} \tag{3.22}$$

$$\tilde{t}_{\text{layer}} = \frac{\tilde{t}_1 \tilde{t}_2 \exp[-i\tilde{\delta}_1]}{1 - \tilde{r}_2 \tilde{r}_1' \exp[-2i\tilde{\delta}_1]} \tag{3.23}$$

The phase is connected to the complex refractive index and the penetration depth by $\tilde{\delta}_1 = (2\pi/\lambda)\, d_1 \tilde{n}_1 = (2\pi/\lambda)\, d_1 (n_1 - i\kappa_1)$.[5] For more than two layers, the approach can be extended by assuming the layer to be an interface with the Fresnel coefficients $\tilde{r}_{\text{layer}}$ and $\tilde{t}_{\text{layer}}$ from the Eqs. 3.22 and 3.23.

The absorption within the layer can be calculated by following the black and white dots in Fig. 3.6. The two geometric series lead to Eq. 3.24.

$$\hat{A}(x,\lambda) = \alpha_1 \Phi_{\text{IN}} \left| \frac{\exp[-i\tilde{\delta}_1 x/d_1]}{1 - \tilde{r}_2 \tilde{r}_1' \exp[-2i\tilde{\delta}_1]} + \frac{\tilde{r}_2 \exp[-i\tilde{\delta}_1] \exp[-i\tilde{\delta}_1 (d_1 - x)/d_1]}{1 - \tilde{r}_2 \tilde{r}_1' \exp[-2i\tilde{\delta}_1]} \right|^2 \tag{3.24}$$

$$\Phi_{\text{IN}} = \Phi_0 T_{01} = \Phi_0 (1 - R_{01}) = \Phi_0 (1 - \left| \frac{\tilde{n}_0 - \tilde{n}_1}{\tilde{n}_0 - \tilde{n}_1} \right|^2) \tag{3.25}$$

Φ_{IN} is the photon flux after the first interface, which can be calculated by multiplying the original photon flux by the transmitted fraction, as shown in Eq. 3.25.

For incoherent flat layers, Eqs. 3.22, 3.23 and 3.24 are changed to Eqs. 3.26, 3.27 and 3.28. Here, the norm is taken before calculating the geometric series. The series consists of real numbers here.

---

[5] The complex phase is only relevant for "total" reflections and does not have to be discussed here.

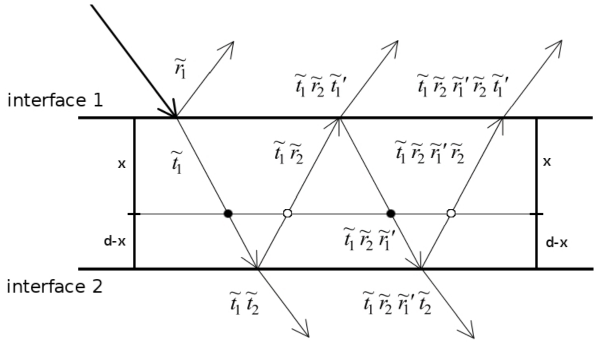

Figure 3.6: Schematic diagram for the absorption calculation with Eq. 3.24. The black dots mark the light paths for the geometric series represented by the left term in the norm of Eq. 3.24, the white dots represent the geometric series of the right side in the norm. Based on Fig. 3.2 of [67].

$$R_{\text{layer}} = |\tilde{r}_1|^2 + \frac{|\tilde{t}_1|^2\,|\tilde{t}_1'|^2\,|\tilde{r}_2|^2 \exp[-2\alpha_1 d_1]}{1-|\tilde{r}_2|^2\,|\tilde{r}_1'|^2 \exp[-2\alpha_1 d_1]} \tag{3.26}$$

$$T_{\text{layer}} = \frac{|\tilde{t}_1|^2\,|\tilde{t}_2|^2 \exp[-\alpha_1 d_1]}{1-|\tilde{r}_2|^2\,|\tilde{r}_1'|^2 \exp[-2\alpha_1 d_1]} \tag{3.27}$$

$$A_{\text{layer}} = \alpha_1 \Phi_{\text{IN}} \frac{\exp[-\alpha_1 x] + |\tilde{r}_2|^2 \exp[-\alpha_1(2d_1 - x)]}{1-|\tilde{r}_2|^2\,|\tilde{r}_1'|^2 \exp[-2\alpha_1 d_1]} \tag{3.28}$$

Layers with rough interfaces

In general, the optical analysis described in this subsection is not sufficient for thin-film photovoltaic cells and modules. For example, a standard PV cell based on amorphous silicon has the layer sequence glass/TCO/p-type Si/intrinsic Si/n-type Si/Al. The TCO-Si interface is often rough to achieve photon trapping, which, due to scattering, leads to an increased probability for the photons to be absorbed in the silicon photovoltaic layers. These interfaces cannot be considered to be flat, and e.g. Eq. 3.15 cannot be applied anymore. Instead, the probability of reflection into a certain angular range has to be known for a given rough interface. This wavelength-dependent function is called ADF, angular distribution function. If also the dependence on the incidence angle is desired, the BSDF, bidirectional scattering distribution function, has to be known.

Furthermore, there are interfaces with a specular fraction of reflection and/or transmission. This leads to the need for a combined, semi-coherent approach.

For both problems, there is no standard solution, and certain simplifications have to be made. The simulation of rough interfaces is important, but not straightforward.

For the optical simulation of rough interfaces, the following assumptions are made within the program ASA: [67]

- The simulation taking into account coherent light propagation is combined with the simulation of incoherent light propagation. The ratio of the light with incoherent light propagation to the total amount of light is called the haze parameter; its definition range is between 0 and 1.
- The diffuse fraction (haze parameter) depends on the incidence angle.
- The reflected and transmitted light of a random interface is rotationally symmetric with respect to the surface normal. In other words, each is only a function of one angle, the angle of incidence.
- The area of the layers is neglected (one-dimensional calculation).
- The total of the reflected light from a rough interface is identical to that from a flat interface.

As a consequence, for the simulation of the total reflection and transmission of a rough layer, four input functions are necessary: the reflection and transmission dependent on the emergent angle, called $f_R(\lambda, \theta_{out})$ and $f_T(\lambda, \theta_{out})$, and the haze parameters $H_R(\lambda, \theta_{in})$ and $H_T(\lambda, \theta_{in})$. All four functions can be measured or estimated, respectively. For rough interfaces without a specular fraction, the functions $f_{R/T}(\lambda, \theta_{out}) = cos(\theta_{out})$ and $f_{R/T}(\lambda, \theta_{out}) = cos^2(\theta_{out})$ are suggested.

First assuming the haze factor to be one, R and T from the Eqs. 3.26 and 3.27 can be expanded to matrices. Within the following formulas, the matrices are indicated by the sign ˇ. The dimension of $\check{R}$ and $\check{T}$ equals NxN, N being the chosen discretisation of the two angles. The energy conservation is fulfilled with the conditions of Eq. 3.29 and 3.30.

$$\sum_{\theta_{out}} [\check{R}_{11}(\theta_{in}, \theta_{out}) + \check{T}_{12}(\theta_{in}, \theta_{out})] = 1 \qquad \forall\ \theta_{in} \tag{3.29}$$

$$\sum_{\theta_{out}} [\check{R}_{22}(\theta_{in}, \theta_{out}) + \check{T}_{21}(\theta_{in}, \theta_{out})] = 1 \qquad \forall\ \theta_{in} \tag{3.30}$$

The first index of the matrices defines the original, the second one the target medium. If there are two possibilities (e.g. R_{22}) for a three-layer composition), a third index defines the concerned layer (e.g. $R_{22,1}$).

Again, a layer can be reduced to an effective surface with the geometric series:

$$\check{R}_{11,\mathrm{eff}} = \check{R}_{11,1} + \check{T}_{21} \cdot \check{M}_2 \cdot \check{R}_{22,2} \cdot \check{M}_2 \cdot [\mathbb{1} - \check{R}_{22,1} \cdot \check{M}_2 \cdot \check{R}_{22,2} \cdot \check{M}_2]^{-1} \cdot \check{T}_{12} \quad (3.31)$$

$$\check{T}_{13,\mathrm{eff}} = \check{T}_{23} \cdot \check{M}_2 \cdot [\mathbb{1} - \check{R}_{22,1} \cdot \check{M}_2 \cdot \check{R}_{22,2} \cdot \check{M}_2]^{-1} \cdot \check{T}_{12} \quad (3.32)$$

$$(\check{M}_j)_{ii} = \exp[-\alpha_j d_j / \cos(\theta_i)] \qquad \forall\, i \quad (3.33)$$

Therefore, the calculation of $2N$ geometric series per layer is necessary. After the straight-forward calculation of the irradiances E_j^+ and E_j^-, defined as the upward and downward irradiance within the j^{th} layer, the absorption profile is calculated with Eq. 3.34.

$$A_j(\lambda, x_j) = \frac{1}{N}\left(\sum_{i=1}^{N} \frac{\alpha_j}{\cos(\theta_i)} E_{j,x_j}^{+/-}\right) \quad (3.34)$$

For layers with a haze parameter that does not equal 0 or 1, both approaches can be combined. Within the specular calculation, the Fresnel coefficients are changed with the following assumptions:

$$\tilde{r}_{spec} = \tilde{r} \cdot \sqrt{1 - H_R} = \frac{\tilde{n}_0 - \tilde{n}_1}{\tilde{n}_0 + \tilde{n}_1} \sqrt{1 - H_R} \quad (3.35)$$

$$\tilde{t}_{spec} = \tilde{t} \cdot \sqrt{1 - H_T} = \frac{2\tilde{n}_0}{\tilde{n}_0 + \tilde{n}_1} \sqrt{1 - H_T} \quad (3.36)$$

For the diffuse part of the semi-coherent simulation, correction factors for the incident radiation which are based on the corrections of the specular part are applied to fulfill the law of energy conservation.

3.3.2 Simulation of the electrical cell behavior with ASA

As the simulation of the cell I–V characteristics from the generation profile was not investigated, but only applied within this thesis, and direct dependences of the electrical simulation of the PV cell for building integration do not exist, the description of this part will be kept short. A summary can be found in [66] and, again, in [67].

For the calculation of the I–V characteristics of an a-Si:H PV cell, the standard properties of a-Si:H have to be considered. The amorphous structure of a-Si:H leads to a different density of states (DOS) distribution compared to crystalline silicon; still, there are clear valence and conduction band states, but in contrast to crystalline silicon, there are tail states for the valence band as well as for the conduction band. Within the ASA program, the number of tail states is assumed to be an exponential function of energy. Furthermore, states within the energy band gap, which are caused by coordination defects, have to be considered. These band-gap states can be of positive, negative or neutral charge; furthermore, they are localized, not extended. In general, the changes in the DOS lead to more complicated recombination-generation (R-G) statistics; within the program, the Shockley-Read-Hall statistics are applied for the tail states, while the Sah/Shockley statistics describe the dangling bond defect states of all charges. For multi-junction PV cells, also models for tunnel-recombination junctions (TRJ) are implemented.

4 Results of performed simulations and validation

4.1 Overview

This chapter includes all analyses and validations that have been carried out to investigate the quality of a BIPV simulation. Although each simulated PV system includes irradiance or temperature simulations, it has been decided to split chapter 4 into the following sections. First, general simulations of the irradiance on the PV cells of a BIPV system have been performed, including error analyses of simulation approaches of various degrees of complexity. In the second section, the investigations made at the cell level are described that are necessary for an electricity yield simulation, especially performance and limits of the PV cell's behavior at low light intensities, predicted with the two-diode model. The next section includes all the investigations of this PhD thesis at module level; the PV cell's operation points are analyzed under partial shading conditions, and I–V curve measurements of a PVSHADE sample at different incidence angles of irradiation are analyzed. Finally, simulations of the DC and AC power output at the system level have been performed. The conclusions are summarized in chapter 5.

In this PhD thesis, four PV systems have been chosen for the analysis and validation of the proposed simulation procedure to evaluate the electricity yield of building-integrated photovoltaic systems. The PV roof-top system in Bad Krozingen, presented in subsection 4.5.1, does not qualify to be called building-integrated. However, for the validation of the shading simulation of section 2.6, a PV system with a small and monitored amount of shading with PV modules based on monocrystalline silicon is very suitable. The calculation of the irradiance on tilted orientations and at partially shaded positions can be validated, and the cell and module I–V curves can be predicted with high accuracy. The second chosen PV system, which is building-integrated, is presented in subsection 4.5.2. It is based on poly-crystalline PV cells and has a far more complex and larger amount of shading. Furthermore, the temperature analysis has to be more detailed for building-integrated PV systems. The third PV system, described in 4.5.3, is not building-integrated, but allows the analysis of the outdoor behavior of amorphous silicon modules; the effect of light-soaking is estimated, as far as the two-diode model allows. The fourth chosen PV system, described in 4.5.4, has not yet been monitored for long enough to allow validation; however, it shows the possibility of mismatch analyses and predictions.

The most challenging investigation that has been performed, however, is described at the module level in section 4.4. The I–V curve measurements of a PVShade® module and their comparison to the simulation results clearly showed the need for a RADIANCE representation of the light sources used in the g-value laboratory of Fraunhofer ISE to interpret the angle-dependent measurements.

4.2 Quantitative investigations of the irradiance on a PV module surface

4.2.1 Validation of the simulated irradiance on a tilted surface

The basis of all irradiance calculations that have been discussed in section 3.2 is the Perez sky model, which itself is based on measured global horizontal and diffuse horizontal irradiance values. It is therefore important to analyze to which extent this pair of irradiances can provide a good representation of the sky radiance distribution, and how far the Perez model succeeds in providing it.

However, when validating simulated irradiance values, a compromise has to be made regarding the orientation used for validation. Simulating horizontal irradiance values obviously does not validate the Perez model. When calculating the irradiance on a tilted surface, the ground albedo has to be accounted for. The validation was done with the irradiance values over a year, measured by two CMP11 pyranometers: one horizontal and one tilted 45° and facing south. Assuming an albedo of 0.2, it can be read from Fig. 4.3 that the light fraction coming from the ground is around 2.5%. The measured irradiance values are depicted in Fig. 4.1.

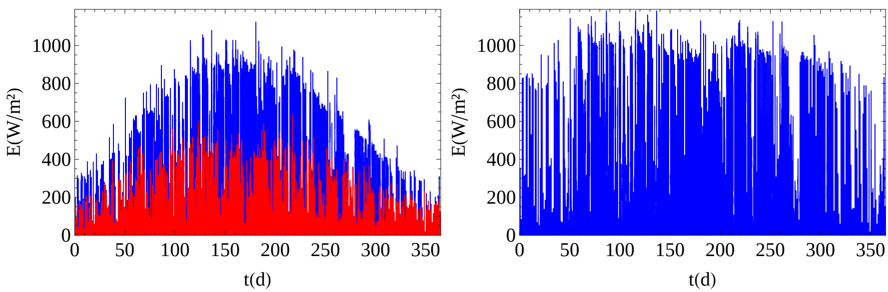

Figure 4.1: Left: Global (blue) and diffuse (red) horizontal irradiance data of the year 2005 in 10-minute steps, measured at Fraunhofer ISE in Freiburg i.B. with a pyranometer with a sun-tracked shading ball. Right: Irradiance on a 45° tilted surface facing south, also measured with a pyranometer.

The measured and simulated irradiance values on a tilted surface are compared in Fig. 4.2. Here, the simulation was performed by standard ray tracing (*rtrace −I−* command) without discretizing the sky. In the left graph, the difference between simulated and measured irradiance is depicted. During the summer, these differences are very small, while there are some outliers during the winter months. The latter can be explained by snow on one of the two pyranometers or higher ground albedo due to snow. On the right, the simulated and measured irradiance are depicted for five arbitrary summer days; the graphs show that the Perez sky model works very well. Expressed quantitatively, and for 10-minute time steps, the coefficient of determination, R^2, is 99.00%, with a root mean square error of $RMSE$=30.93 W/m^2 and a mean bias error of MBE=-8.74 W/m^2 even without excluding the wrong measurements during the winter. The definition and significance of these statistical measures, which will appear frequently within this chapter, are summarized in appendix A. For other sensor orientations, the deviation of the irradiance simulation to the measurements is difficult to guess. Measurements at vertical orientations can only be modelled satisfactorily if the albedo value is constant, for example that for a gravel roof. For the error analysis of sensor orientations differing from south, further measurements are necessary.

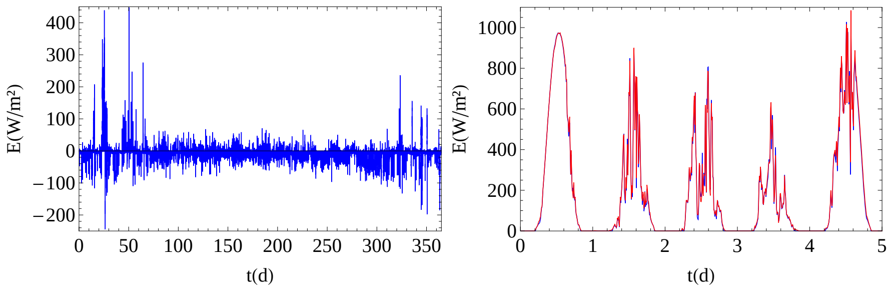

Figure 4.2: Left: The difference between simulated and measured irradiance on a tilted surface at 45° tilt angle oriented to the south. Right: Simulated (blue) and measured (red) irradiance on a tilted surface for five summer days (June 3^{rd}–7^{th}, 2005).

4.2.2 The influence of the albedo on south-oriented PV modules

In subsection 2.2.3, the higher importance of the ground albedo for vertical orientations of PV modules has been described. Fig. 4.3 shows the annual irradiation with and without a ground albedo of 0.2 and the irradiance fraction on a south-facing plane for different tilt angles; Fig. 4.4 shows the dependence of the irradiance on the ground albedo value for the vertical, south orientation. Obviously, at vertical orientations, the albedo has a large influence on the PV electricity yield. For example, snow reflects far better than grass. Throughout this thesis, the standard albedo value of 0.2 has been chosen.

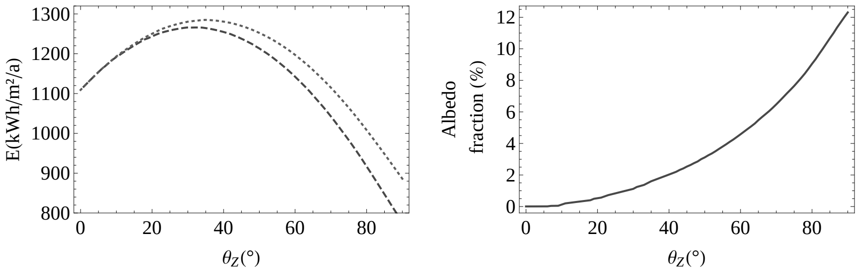

Figure 4.3: Left: Annual irradiation in Freiburg/Germany on a surface with southern orientation for different tilt angles θ. Dotted: with, dashed: without consideration of the ground albedo. Right: percentage of the ground-reflected annual irradiation relative to the total annual irradiation on the tilted surface. Chosen parameters: 0.2 ground albedo, hourly time discretisation of the irradiance values, Perez sky simulation (see Eq. 2.5)

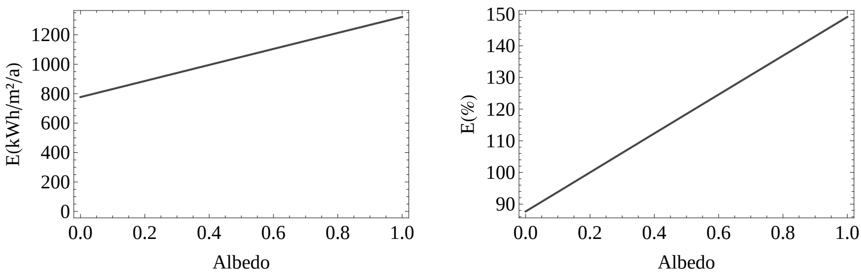

Figure 4.4: Dependence of the irradiation on the albedo for a vertical, south-facing facade. Left: annual irradiation, right: percentage of the irradiation relative to the value obtained with the standard value of 0.2 for the ground albedo.

4.2.3 Comparison of the angular definition of a shading object with the implementation of a rendering procedure

Assuming that the Perez model simulates the sky radiance distribution and the object reflections correctly, the two approaches described in subsection 2.2.4 can be compared by analyzing the impact of light reflection from adjacent objects (like buildings) on the irradiance on the modules. To perform these simulations, the geometrical configuration shown in Fig. 4.5 has been chosen. It consists of two walls with a height of six meters that are orthogonal to each other. On the wall that is oriented to the south, five sensors have been placed to analyze the shading caused by the east-facing wall. For the ground, a circle of 20 m radius has been implemented. All the surfaces are assumed to be Lambertian. The wall reflectivity of

0.65 corresponds to a white wall[1], while the black wall is represented by a reflectivity of zero.

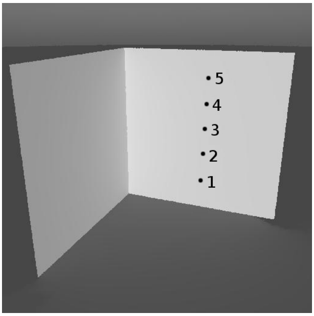

Figure 4.5: Rendered image of the chosen geometrical configuration to perform various basic simulations within section 4.2. The black points indicate the locations of the sensors which are counted from 1 to 5 upwards. The surfaces are assumed to be Lambertian with a reflectivity of 0.2 (ground) and 0.65 (walls), respectively.

With the global-horizontal and diffuse-horizontal irradiance values of the year 2005 in ten-minute steps, which have already been depicted in Fig. 4.1, the annual energy total due to irradiation at point no. 3 in the middle, calculated by normal ray tracing with $-ab$=4,[2] is calculated for the following situations: (1) with the east-facing wall and the ground albedo, (2) with the wall, but without the ground albedo, (3) without the east-facing wall, with the ground albedo; (4) with neither the wall nor the ground albedo, (5) with a black east-facing wall, with the ground albedo, and (6) with a black east-facing wall, without the ground albedo. For one arbitrary sunny day, the results are depicted in the left-hand graph of Fig. 4.6. On the right, the results for simulation (1) are depicted for every sensor.

The resulting values of annual irradiation can now be applied to analyze the losses due to the east-facing wall.[3] For this issue, sensor no. 1 is chosen. Performing the simulation of the annual irradiation with the wall and the ground, the annual irradiation at this sensor position is 779.86 kWh/m^2/a. This value includes light incident via paths like sky-ground-wall-sensor or sky-sensor-wall-sensor.[4] Without considering the reflections from the east-facing wall (but still considering light paths like sky-sensor-ground-sensor), the annual irradiation is 705.77 kWh/m^2/a. In relative numbers, this means that the wall decreases the annual irradiation on the sensor by

[1] $R = 0.65$ is the reflectance value of a rather gray-white wall. The color RAL9002 with $R = 0.668$ is called gray-white, while RAL9010, pure white, has a reflectance of $R = 0.838$ [61].

[2] The results of different ambient bounce settings have been simulated; between $-ab$=3 and $-ab$=4, the difference is below 1%. For further details, see subsection 3.2.6.

[3] If no color is specified in the following lines, the expression “wall” means the “real” gray-white wall.

[4] Here and in the following lines, the reflection paths are named with “wall” (meaning the east-facing wall) and “sensor” (meaning the south-facing wall or the final sensor position).

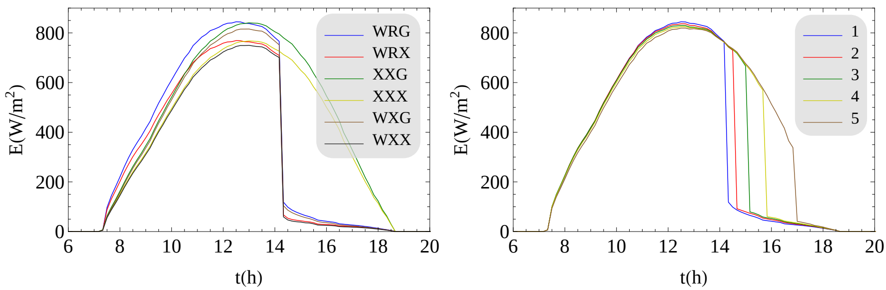

Figure 4.6: Simulated irradiance for an arbitrary sunny day (March 16^{th}, 2005). Left: sensor no. 1. The calculations have been performed for the following situations: with the east-facing white wall and the ground (WRG); with the white wall, but without the ground (WRX); without the wall, but with ground (XXG); without both the wall and the ground (XXX); with a black wall and the ground (WXG); with a black wall, but without the ground (WXX). Right: The irradiance simulation of the same day for the configuration with the east-facing white wall and the ground, for all five sensor points.

9.50%. This is also the error that common PV simulation programs, which define the shading objects by shading angles, would make when simulating this geometrical configuration, as described in section 2.2.

After performing these detailed ray-tracing simulations, further conclusions can be drawn. Without the east-facing wall, but with the ground, the annual irradiation on sensor no. 1 is 923.83 kWh/m^2/a. The same simulation without considering the ground albedo leads to an annual irradiation of 811.89 kWh/m^2/a which corresponds to a relative deviation of 12.11%. This agrees well with the results within Fig. 4.3 although the absolute values differ due to the light path sky-sensor-ground-sensor.

Furthermore, the losses due to the east-facing wall can be analyzed. Assuming this wall to be perfectly black ($R = 0$), the annual irradiation including the ground reflections is 705.77 kWh/m^2/a. This corresponds to an annual loss of 23.06% compared to the same geometrical configuration without an east-facing wall. With a white wall, as can be concluded by the annual irradiation value of 779.86 kWh/m^2/a, the relative loss is 15.58%.

Comparing the annual irradiation reaching the sensor after the radiation has been reflected from the ground for the configuration without the east-facing wall (111.94 kWh/m^2/a) with that with a black wall (78.75 kWh/m^2/a), the impact of the ground obstruction by the east-facing wall can be analyzed. Their difference of 33.19 kWh/m^2/a compared to the annual irradiation on the sensor with a white wall and the ground corresponds to an annual irradiation fraction of 4.26% that is lost due to ground obstruction by the east-facing wall.

The calculated annual irradiations for the different analyzed configurations are summarized in Tab. 4.1.

Wall	R	ground	Total (kWh/m^2/a)
yes	yes	yes	779.86
yes	yes	no	684.60
no	-	yes	923.82
no	-	no	811.89
yes	no	yes	705.76
yes	no	no	627.02

Table 4.1: Annual irradiation on sensor no.1 for different assumed geometrical configurations. The first column specifies whether the east-facing wall has been included, the second (R) defines whether the wall has been chosen white or black, and the third documents whether the simulation has been performed with or without the ground. The last column shows the annual irradiation.

The results lead to the conclusion that for BIPV simulations, the neglection of reflections from the surroundings is not permitted for the general case. However, the approach of defining the shading objects by their angles can be sufficient for small or dark objects.

4.2.4 The impact of the sky discretisation on the penumbra

As discussed in subsection 2.2.5, the reduction of the calculation time achieved by discretizing the sky hemisphere leads to a larger solid angle for the direct light fraction. To avoid ray tracing of the given geometrical configuration (surroundings and façade) for every single time step throughout the year in the simulation, the impact of every sky region on the incident radiation on the PV cells can be calculated. To be able to separate the sky rendering from the ray tracing for the geometrical configuration, the sun has to be incorporated into the sky discretisation. This incorporation can be performed either by assuming the nearest sky region to have the radiance value of the direct sun or, more accurately and avoiding discrete jumps in the sun's position, by calculating the distance to the three nearest-neighbor sky regions and distributing the radiance of the direct sunlight depending on this distance. The RADIANCE program *genskyvec* performs the latter calculation.

The most obvious simulation inaccuracy coming from the sky discretisation and therefore expansion of the direct sunlight source over a larger solid angle is shown in Fig. 4.7. When simulating the geometrical configuration shown in Fig. 4.5, the shading is not predicted as accurately compared to the rendering for every time step. This can be traced back to the larger solid angle of the direct irradiance fraction which leads to a larger penumbra.

It can be concluded from Fig. 4.7 that 145 sky regions are certainly not enough to perform shading analyses, while the result for 577 regions is still not satisfying. For the choice of the number of sky regions, the ratio of the distance between the sensor points and the distance of the shading object to them is decisive. However, the higher

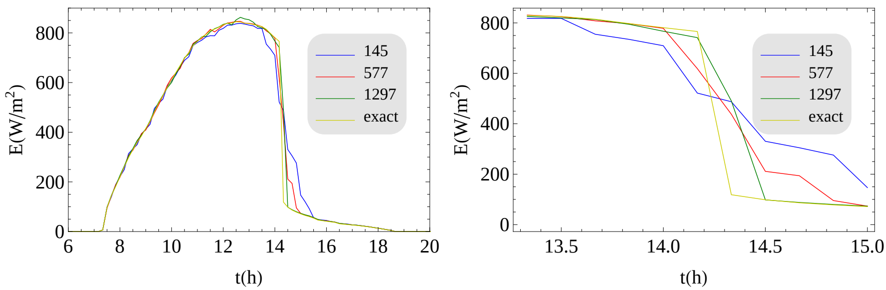

Figure 4.7: Irradiance at sensor no. 1 for the configuration shown in Fig. 4.5 for a sunny day (March 16th, 2005), simulated with different sky discretisations. On the left, the full day is plotted; the decisive period between 14 and 15 hours is depicted on the right. The colored lines represent different numbers of discretisation patches of the sky. In yellow, the time-dependent ray-tracing result is shown. The calculations are performed with 10-minute steps, which explains the non-vertical flank of the yellow curve.

penumbra has a smoothing effect on the local irradiance distribution, so it even may be helpful when problems due to discretisation of the chosen sensor points occur (for example, for very inhomogeneous irradiance levels on the module surface).

4.2.5 The incidence angle dependence of the irradiance on a PV module

For BIPV systems, especially for vertical orientations, the fraction of high incidence angles can be significantly higher than for ground-mounted systems that are oriented to optimize the electricity yield and therefore to minimize the angle of incidence. This fraction also determines the importance of the angular response of the modules for BIPV electricity yield simulations. In Fig. 4.8 and Fig. 4.9, the dependence of the irradiance on the incidence angle is shown for different PV module orientations without shading objects, assuming the location to be Freiburg i.B. (48° N). The simulations were carried out with 10-minute values with 577 sky discretisation regions and taking a ground albedo of 0.2 into account.

The impact of the incidence angle dependence of the diffuse irradiance fraction

For free-standing PV plants, the incidence angle dependence of the diffuse fraction of the irradiance on a PV module does not have to be analyzed; the 60° approach of Eq. 2.16 for the simulation of the effective irradiance is sufficient. However, this is not so clear for vertical orientations, due to the larger amount of high incidence angles and the greater fraction of diffuse irradiance. With the detailed approach described in 3.2.7, the exact values can be compared to the approximation of neglecting the incidence angle dependence of the diffuse irradiance fraction. The result of the latter

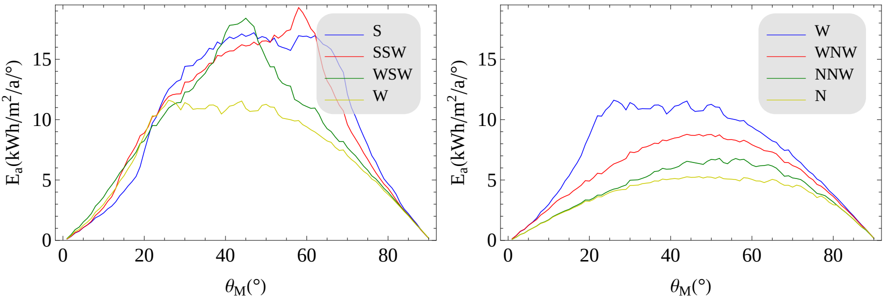

Figure 4.8: Incidence angle dependence of the annual irradiation on different vertical orientations for a BIPV system in Freiburg i.B. (48° N). Left: south (S), south-south-west (SSW), west-south-west (WSW), west (W). Right: west (W), west-north-west (WNW), north-north-west (NNW), north (N).

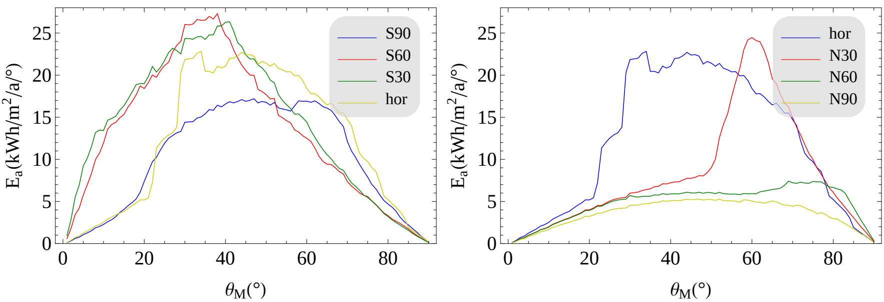

Figure 4.9: Incidence angle dependence of the annual irradiation on different tilt angles for a BIPV system in Freiburg i.B. Left: south vertical (S90), south 60° tilted (S60), south 30° tilted (S30), horizontal (hor). Right: horizontal (hor), north 30° tilted (N30), north 60° tilted (N60), north vertical (N90).

approximation obviously depends on the angular response, that means, on the layer composition of the module. For the validation of the approximation, the angular response curve from the Martin-Ruiz model, depicted in Fig. 2.5, has been chosen. Due to the relevance of the incidence angle distribution, the results also depend on the location and the considered year. In the following analysis, Freiburg i.B. and irradiance data from the year 2010, which is available in 10-minute steps, has been selected. The albedo is assumed to be 0.2. The orientations are the same as in Figs. 4.8 and 4.9, the resulting statistical measures, according to App. A, are depicted in Tab. 4.2 and 4.3.

The results show that the simple approach of Eq. 2.16 is completely adequate for all orientations relevant for BIPV applications, if there is no special angular response behavior (like PVShade® or similar angle-selective PV elements). No investigation of the incidence angle distribution of the diffuse irradiation fraction is required if

Orientation	$R^2[\%]$	RMSE	MBE	$\overline{s.det.}[W/m^2]$	$\overline{s.60}[W/m^2]$
S/90°	99.958	4.51	−0.19	214.80	214.99
SSW/90°	99.952	4.80	−0.24	209.76	210.01
WSW/90°	99.943	4.90	0.07	188.66	188.59
W/90°	99.933	4.50	−0.06	154.51	154.57
WNW/90°	99.919	3.58	−0.19	117.02	117.21
NWN/90°	99.887	2.45	−0.34	87.61	87.95
N/90°	99.848	1.81	−0.33	75.68	76.01

Table 4.2: Statistical measures, according to App. A, when comparing different models to simulate the effective irradiance, based on meteorological data of the year 2010 at Freiburg i.B. Comparison of the approach of Eq. 2.16 and the detailed incidence angle analysis of section 3.2 for vertical module orientations without shading, with the AR curve of Fig. 2.5. The *RMSE* and *MBE* values are given in W/m^2. The mean values of the irradiance in both the detailed and the 60°-approach are listed in column five and six.

Orientation	$R^2[\%]$	RMSE	MBE	$\overline{s.det.}[W/m^2]$	$\overline{s.60}[W/m^2]$
S/90°	99.958	4.51	−0.19	214.80	214.99
S/60°	99.973	4.75	0.82	290.40	298.59
S/30°	99.972	4.88	0.77	307.53	306.76
hor	99.954	5.12	−1.01	257.02	258.03
N/30°	99.905	4.69	−0.46	168.24	168.7
N/60°	99.781	3.14	0.14	98.05	97.91
N/90°	99.849	1.80	−0.33	75.68	76.01

Table 4.3: Statistical measures when comparing different models to simulate the effective irradiance, based on meteorological data of the year 2010 at Freiburg i.B. Comparison of the approach of Eq. 2.16 and the detailed incidence angle analysis of section 3.2 for different N/S module orientations without shading, with the AR curve of Fig. 2.5. The *RMSE* and *MBE* values are given in W/m^2.

there are no shading objects and the layer composition of the module is simple. Obviously, the diffuse irradiance fraction is still small enough and their average angular response value is near enough the assumed one for 60° to keep the results satisfying. For angle-selective modules or special absorption-enhancing techniques like light trapping etc., not only the angular response curve, but also the reliability of the 60° approach has to be analyzed in detail.

4.3 Investigations on the level of photovoltaic cells

4.3.1 Comparison of the two-diode model for an a-Si:H PV cell with the results of the ASA program

As described in subsection 2.5.1, the two-diode model, which gives good results for monocrystalline PV cells, is the standard model for the simulation of the cell I-V curve dependent on temperature and irradiance. However, when the model is applied to thin-film PV cells, sim"ulation problems occur.

To quantify the deviations when applying the two-diode model to thin-film PV cells, its results are compared to more detailed I–V curve simulations with the ASA program described in section 3.3. For this purpose, an ASA input file with all the available material specifications of an examined PV cell of amorphous silicon is taken. With this file, the I–V curves at different irradiances and temperatures can be calculated. The material specifications can be found in the annex of the diploma thesis of R. Kind [28]; the most important input parameters for ASA are also tabulated in [50]. The cell size has been set to $A_{cell} = 10^{-3}$ m^2. To gain the parameters of the two-diode model, the I–V curve at standard test conditions is fitted. The result of this fit is shown in Fig. 4.10.

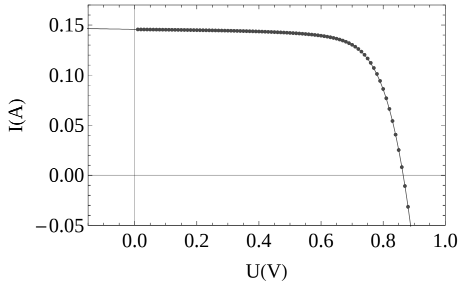

Figure 4.10: The STC I–V curve for an amorphous silicon PV cell that has already been examined in detail in [28]. Dotted: the STC I–V curve simulated with ASA, solid line: two-diode model fit to the ASA result.

The two-diode model fit leads to good agreement with the STC curves. The resulting values, assuming $n_1 = 1$, are: $n_2 = 2.28$, $I_{s1} = 4.81 \cdot 10^{-17}$ A, $I_{s2} = 4.66 \cdot 10^{-8}$ A, $R_s = 0.181\ \Omega$, $R_p = 167.75\ \Omega$. With these parameters, the two-diode model also allows calculation of temperature-dependent and irradiance-dependent results. These dependences can now be compared to the ASA results.

Low-irradiance behavior

The most important result of the two-diode model is the simulation of the cell behavior at low irradiance values. However, although the fitting parameters for the STC curve were identified unambigiously, large deviations are observed in comparison to a detailed analysis of the physical PV cell behavior, performed with the ASA program. Fig. 4.11 shows the results of both approaches.

While the linear behavior of the short-circuit and MPP currents has been maintained, the voltage results of the two-diode model under low irradiance conditions are lower than the results of detailed simulation with the ASA program. The conse-

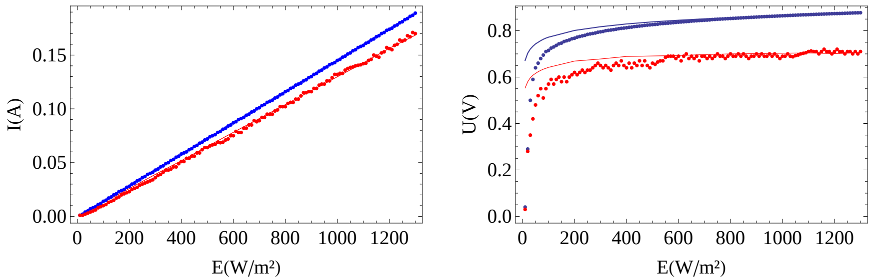

Figure 4.11: Simulation results for the behavior of the a-Si cell at low irradiance; solid line: ASA results, dots: two-diode model. Left: the values for I_{sc} (blue) and I_{MPP} (red) versus the irradiance. Right: the dependence of V_{oc} (blue) and V_{MPP} (red) on irradiance.

quences for the simulated fill factor $FF = P_{MPP}/(I_{sc} \cdot V_{oc})$ and the PV cell efficiency are shown in Fig. 4.12.

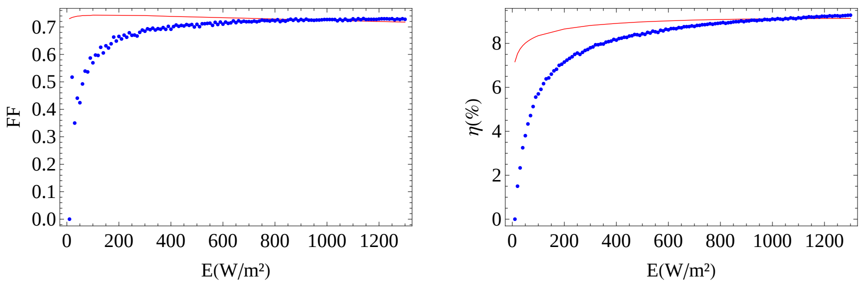

Figure 4.12: The fill factor (left) and the efficiency (right) of the a-Si cell versus the irradiance. Red: result of the detailed ASA simulation, blue: result of the two-diode model.

Especially Fig. 4.12 shows the importance of a more detailed simulation program for the I–V curves, at least for amorphous silicon PV cells. The deviation of the results gained by the two-diode model to the ASA results exceeds 10% for irradiance values less than $230 \pm 30\ \mathrm{W/m^2}$ for the fill factor and $320 \pm 10\ \mathrm{W/m^2}$ for the efficiency. The two-diode model can be considered to be inadequate. The question is still open, whether PV cells measured after the production process, without any knowledge about the details of their layer composition, can be simulated with higher precision. Research on this topic is definitely needed; the PVMD research group at the Delft University of Technology is also working on this subject.

Temperature dependence

To simulate the temperature dependence of a PV cell with the two-diode model, Eqs. 2.25, 2.26 and 2.24 are applied as a standard procedure. However, these formulas obviously lead to wrong results for amorphous silicon. Assuming a temperature coefficient $\alpha = -0.022\%/\mathrm{K}$ for the short circuit current, the resulting temperature coefficients for the open circuit voltage and the MPP power are $\beta = -0.228\%/\mathrm{K}$ and $\gamma = -0.248\%/\mathrm{K}$. Here, the results are very different to the ASA results, corresponding to large deviations from the data sheet specifications in sections 4.5.3 and 4.5.4, leading to the hypothesis that the temperature dependences of Eqs. 2.25 to 2.24 do not apply for thin-film technologies.

Instead, within this thesis, the following assumption has been made: the temperature coefficients for the short circuit current ($\alpha = -0.022\%/\mathrm{K}$) and the open circuit voltage ($\beta = -0.223\%/\mathrm{K}$), that are specified in the data sheet, are valid for the whole voltage and current range. This assumption is wrong for wafer-based technologies, because the temperature coefficients in the MPP region are higher for both the current and the voltage, but it works well for thin-film technologies. The resulting temperature coefficient for the MPP power is $\gamma = -0.330\%/\mathrm{K}$. The results are plotted in Fig. 4.13.

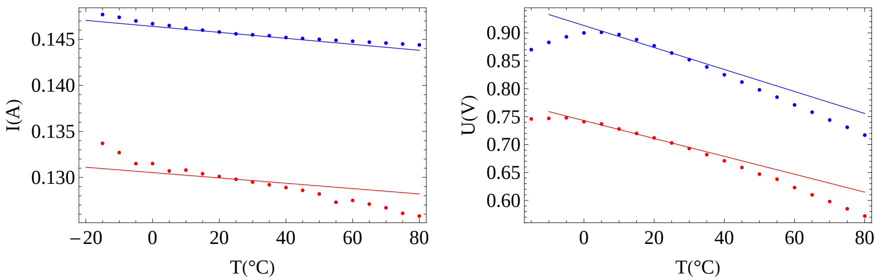

Figure 4.13: Simulation results for the temperature dependence of the current and the voltage of the a-Si cell. Left: short circuit current (blue) and MPP current (red); right: open circuit voltage (blue) and MPP voltage (red). Dotted: ASA results, solid line: two-diode model (linear assumption).

The mentioned assumption leads to the deviation in the MPP power shown in Fig. 4.14.

Unlike the crystalline PV technologies, the temperature dependences are non-linear for amorphous silicon. By comparing the ASA results with the electrical properties of an a-Si PV cell operating under changing temperature and irradiation conditions, the separation of the material properties from the complications described in the section about light soaking and annealing, section 2.8, is possible. However, under outdoor conditions, the dangling-bond density changes, and the consequences for all the material properties are still not fully understood. Furthermore, the detailed

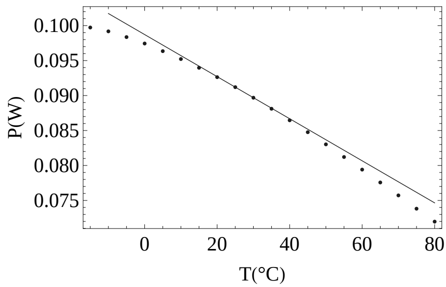

Figure 4.14: Simulated dependence of the MPP power on the temperature of the a-Si cell. Dotted: ASA result, solid line: two-diode model (linear assumption).

analyses with ASA cannot be performed with commercially available PV cells. Until better models than the two-diode model exist, it still has to be used for the low-light and temperature investigations of amorphous silicon PV cells in PV modules and systems, as has been done in subsections 4.4.2, 4.5.3 and 4.5.4. In general, the issue of modeling I–V curves for amorphous silicon PV cells as a function of irradiance and temperature can be considered to be independent of the BIPV-related studies of this PhD thesis.

4.4 Investigations on the level of photovoltaic modules

4.4.1 Cell connection issues at the module level

The principles of combining cell I–V curves to module and system I–V curves, dependent on the wiring configuration, has been described in subsection 2.6.2, and, including the diodes, in subsection 2.6.3. The calculation of I–V curves of combined PV cells is straight-forward, as is the calculation of the operation points of every cell when the PV system is MPP-tracked. However, the resulting cell operation points are not easy to predict, especially for complicated shadow patterns.

Cells operation points in the second or fourth quadrant of the I–V curve are abbreviated as “negative operation points” in this PhD thesis. They are mainly caused by inhomogeneous irradiation of the PV module. At negative cell operation points, power is not generated, but absorbed, which can lead to a severe temperature rise of the PV cells. In order to avoid damage to the PV cells, it is important to prevent the cells from possible heating. The best way in theory would be a bypass diode parallel to and a blocking diode in series with every cell. In practice, one bypass diode protects a certain number of series-connected cells. The implications are discussed in the following lines.

The roof-integrated PV modules that are discussed in subsection 4.5.2 are customized products. To reduce the loss of electric power due to shading, the 36–cell modules have been connected to form three separate electric circuits, as depicted in Fig. 4.15.

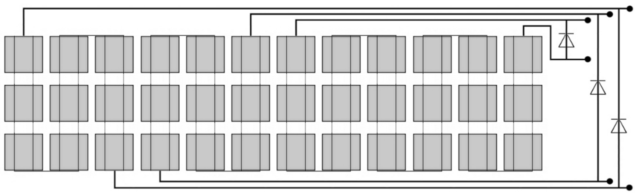

Figure 4.15: Electric circuit of the customized modules of the roof-integrated BIPV system of 4.5.2. The squares represent the polycrystalline silicon cells. The more frequently shaded, lower part of the PV module corresponds to the left side of the schematic diagram, where one bypass diode is connected in parallel to nine PV cells each. The upper part of the PV module, which is shaded less, corresponds to the right side of the diagram. Here, one bypass diode is connected in parallel to 18 PV cells.

Three bypass diodes are connected in parallel to the strings of nine, nine and eighteen polycrystalline cells and prevent these cell strings from operating at negative voltages (the diode voltage can be neglected in this case). To simplify the following calculation, a constant cell temperature of 25°C is assumed. Furthermore, in each case, one cell of a 9-cell or the 18-cell string, respectively, is shaded homogeneously, while the other cells operate at STC. With the assumption that this single module is MPP tracked, the operation point of the shaded cell can be calculated according to subsection 2.6.2. Fig. 4.16 shows the resulting electric power generated (positive) or absorbed (negative values) by the shaded cell.

The graph shows low negative voltage (and therefore power) values at irradiance values below 106.5 W/m^2 for 9 cells and 231.1 W/m^2 for 18 cells. However, in a real PV system, usually a single module is not MPP tracked. The simulated situation applies at the system level only if all the modules of the PV system are shaded in exactly the same way. Symmetric shading structures are common for free-standing plants, as shown by the PV system presented in 4.5.1. For BIPV systems, however, the general case of different degrees of shading of the involved modules is important.

The general case does not allow any predictions of the module voltage imposed by the inverter, because it depends on the irradiance level on the cells of the other modules. The only well-defined boundary condition is that the module voltage is positive due to the bypass diode. The operation point of each module is determined by the whole system. Fig. 4.17 again shows the power associated with the shaded cell of Fig. 4.16 as a function of the irradiance, but this time not under the condition of MPP tracking, but, more generally, for different impressed module voltages.

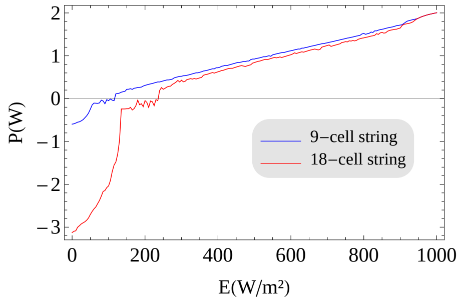

Figure 4.16: The electric power generated or absorbed by one shaded cell of a 9-cell or an 18-cell string, respectively, with the remaining cell string operating at STC and being MPP tracked, versus irradiance level on the shaded cell. Blue: Cell in 9-cell string, red: cell in 18-cell string. Positive power values indicate that the shaded cell generates energy; negative values mean the cell absorbs energy and is heated up.

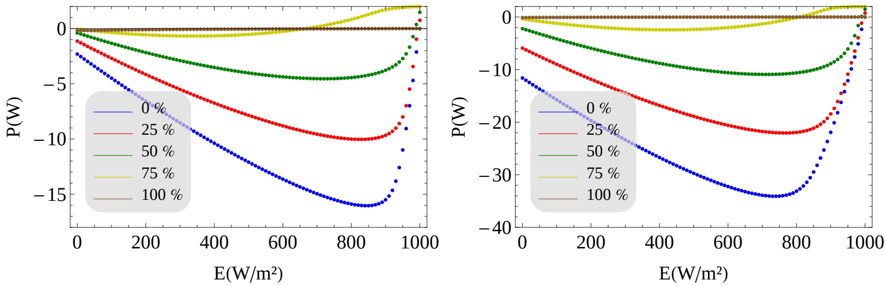

Figure 4.17: Power absorbed or generated by the single shaded cell at different module voltages versus irradiance level on the shaded cell. Negative values indicate that the cell is heated up. Left: cell in 9-cell string, right: cell in an 18-cell string. Blue: 0%, red: 25%, green: 50%, yellow: 75%, brown: 100% of the STC open circuit module voltage.

The graphs of Fig. 4.17 show that for low module voltages, a negative operation point of a single shaded cell is probable. Whether the heating power defined by the negative cell operation point damages the p–n junction, depends on the duration of the shading situation, on the cell temperature, on the cell technology, but also on the cell material homogeneity. For complex shading structures, a detailed analysis of the cell operation points under different shading conditions is needed. This also applies to the bypass diodes themselves; their lifetime depends on the frequency of shading situations. Related investigations of polycrystalline silicon cells have been reported in [14].

For thin-film PV modules, however, the situation is different. To demonstrate this, an a-Si module with 106 series-connected cells, and six cell strings connected in parallel, is analyzed. Again, all cells are assumed to operate under STC, while one single cell is shaded.[5] The power corresponding to the cell operation point is plotted versus the cell irradiance. Fig. 4.18 shows the results.

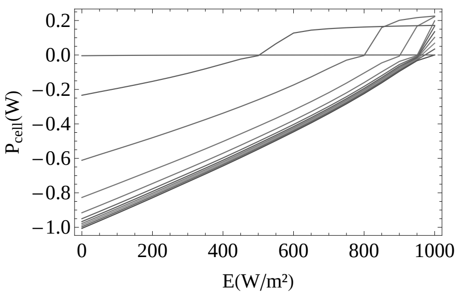

Figure 4.18: Power absorbed or generated by a single shaded cell, P_{cell}, at different module voltages in an a-Si module ("S4" from Signet Solar), the cell being shaded at different irradiance levels and all the other ones operating at STC. Negative values of P_{cell} indicate that the cell is heated up instead of generating power. Lowest curve: 0% of the module STC open circuit voltage (which has a value of 0.896 V), highest curve (along the abscissa): 100% of the module STC open circuit voltage. 11 curves, in steps of 10% of the module STC open circuit voltage, are plotted.

For thin-film PV modules that consist of a parallel connection of cell strings, the most critical case for cell temperature rise due to operation points at negative power values occurs for high shading levels, while for wafer-based technologies, an irradiance value on the shaded cell of around 80% of the irradiance on all the other cells is most critical.

To quantify the impact of the absorbed power, which is defined by the negative cell operation point, on the cell heating, a comparison to the cell heating due to solar irradiation is helpful. This leads to the following result. The cell heating due to absorption at STC, assuming that the module is not operating, can be roughly calculated by $P_{heat} = E \cdot (1-R) \cdot A_{cell}$. For the two examples above, the wafer-based and the thin-film silicon PV module, assuming a reflectance value of 0.225 for pc-Si and 0.358 for a-Si:H [36] and a cell area of $2.43 \cdot 10^{-2}$ m^2 and $2.42 \cdot 10^{-3}$ m^2, respectively, the resulting heat gains due to irradiation are $P_{heat} = 18.83$ W for the polycrystalline silicon cell and $P_{heat} = 1.55$ W for the a-Si:H cell. For wafer-based PV technologies, the cell heating power under shading conditions (here: $P_{OP} = 35$ W, as can be read from the right graph of Fig. 4.17) can be much higher than the highest heat gain due to irradiation (here: $P_{heat} = 18.83$ W). In contrast, for thin-film PV cells, the situation is different: Even for the worst case of PV cell heating due to negative operation points, the heating power under shading conditions is lower ($P_{OP} = 1$ W, see Fig. 4.18) than the cell heating due to irradiation ($P_{heat} = 1.55$ W). Thin-film PV cells are colder when being shaded, as long as the operation point of

[5] This is not the only critical case; also the analysis of the operation points for a totally shaded cell string or the analysis of the operation points for a shaded cell in each cell string may be relevant.

the PV module is not negative. The large number of parallel connections in thin-film PV modules "saves" the shaded cells from heating up.

However, for thin-film PV technologies, the module may also operate at negative voltages due to the lack of a bypass diode. If the module voltage is negative, also the heating power due to negative cell operation points can be higher than in the discussed case of the PV module operation point being in the first quadrant. The module voltage in turn depends on the number of modules and the PV array configuration. As can only be indicated here, the simulation results show that problems may arise for long module strings if one cell of every parallel cell string in every module of one module string is shaded to a large extent and the module string is connected in parallel to enough other, but unshaded module strings. The shaded cells then operate far in the fourth cell quadrant. In any other case, bypass and blocking diodes can be omitted.

For certain irradiance and shading conditions, the cell operation points are certainly relevant for the temperature simulation of the PV cells. This is especially valid for wafer-based PV modules. However, the system I–V curve is not strongly influenced by the higher temperatures of single cells. Furthermore, in most cases, the temperature rise of the shaded cells is only relevant for a short duration. As a conclusion, it can be stated that the operation point analysis is recommended for prediction of critical cell operation points even if bypass diodes are installed. However, although the cell I–V curves will change due to the temperature rise at negative cell operation points, this change can be neglected for the simulation of the power generated by the PV system. Therefore, the dashed line in Fig. 2.1 that indicates this impact can be neglected.

4.4.2 The angular response measurements of the PVShade® module in the *g*-value laboratory of Fraunhofer ISE

At the Fraunhofer Institute for Solar Energy Systems (ISE), the TestLab Solar Facades facility provides the possibility to determine the optical and thermal characteristics of façade elements. The facility is accredited to measure the angle-dependent direct-hemispherical transmittance at AM1.5, the spectrally resolved reflectance and transmittance in the case of homogeneous façade elements, the U-value (heat transfer coefficient, given in $W/(m^2K)$) and the g-value (total solar energy transmittance, given in %). In regular measurements in the g-value laboratory, which is part of this TestLab, the g-value is determined. For the examinations presented in this chapter, however, the solar simulator and rotatable sample holder of the g-value laboratory have been applied for electric measurements of the PVShade® sample, namely I–V curve measurements of the PV stripes of the front and of the back planes of the PVShade® sample separately, at different tilt angles. The long-term aim of performing electrical measurements in the g-value laboratory is to quantify the dependence of the g-value on the module operation point.

The measured PVShade® sample has already been shown in Fig. 1.1. The sample consists of 38 stripes in the front and 38 stripes in the back, with 26 active PV cells per stripe. For the positive and negative electric contacts, four tabs made of aluminum have been installed. As the tabs have no electrical connection to the TCO layer in front of the PV cells, the last, 27^{th} cell of every stripe is left in open circuit and does not contribute electrically.

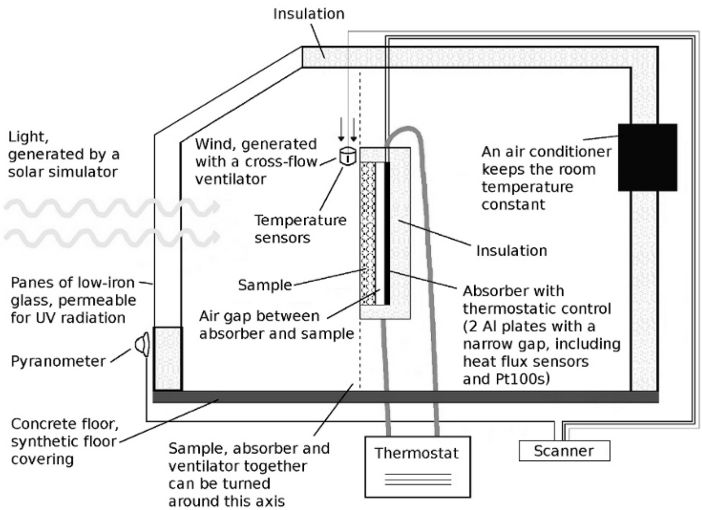

Figure 4.19: Cross-section of the g-value measurement facility at Fraunhofer ISE. Source: TestLab Solar Façades.

Fig. 4.19 shows the layout of the g-value measurement facility. When a façade element is measured, it is fixed on a rotatable mount within the measurement cabin. While the façade element is irradiated through a low-iron glass window by the solar simulator located outside the cabin, the exterior and interior heat transfer coefficients for the sample surfaces are kept constant at the values h_e=25 W/m^2/K and h_i=7.7 W/m^2/K, as defined in the European standard DIN EN 674. The cabin temperature is kept constant as well as the temperature of the absorber behind the sample.

The solar simulator shown in Fig. 4.20 consists of halogen-metal vapor lamps, produced by the company Osram. To keep the irradiation high, which is necessary to avoid the low-light range of the PV cells, as many lamps as possible have to be installed (the maximum number of halogen lamps is four). However, the divergence of the light source has to be considered. For the PVShade® sample, divergent light may lead to inhomogeneous irradiation of the back PV stripes. This again may lead to electrical mismatch of the series-connected PV cells. To keep the impact of beam divergence on the electrical mismatch of the PV cells as low as possible, but the irradiation high, three lamps have been installed above each other, while the cell strings of the installed PVShade® sample are kept vertical. In the chosen configuration, the irradiance on the sample remains rather constant along the vertical axis, even when the sample mount is turned. The inhomogeneous irradiance along the horizontal axis, however, has only a low impact on the DC power due to the parallel PV cell connection along the horizontal axis.

The IEC 60904-9 standard characterizes solar simulators by the following three properties: spectral match to AM1.5, non-uniformity of the irradiance over the test area, and temporal instability of the solar simulator. If the irradiation beam does not consist only of parallel rays, the second property changes with the tilt angle of the sample. As defined in the above-mentioned standard, the non-uniformity (NU) of the solar simulator is calculated by Eq. 4.1.

$$NU = \frac{E_{max} - E_{min}}{E_{max} + E_{min}} \cdot 100 \tag{4.1}$$

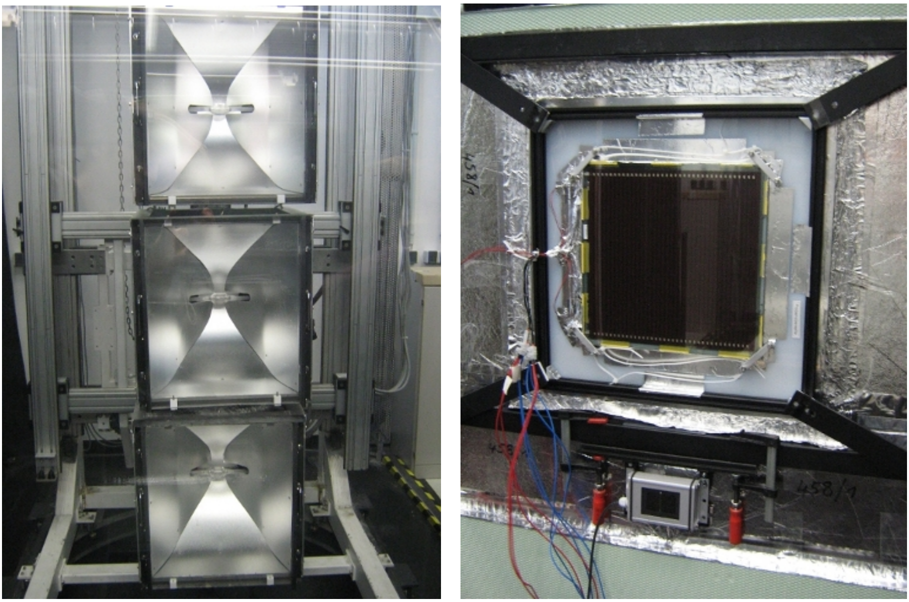

Figure 4.20: Left: the solar simulator of the g-value laboratory in the configuration chosen for the measurements described in this chapter. Right: The PVShade® sample installed on the rotatable mount in the measurement cabin, with a c-Si reference cell.

Simulation of the divergence of the solar simulator with RADIANCE

Before the I–V curve measurements were performed, the irradiance distribution on the sample's surface was measured with a pyranometer. This measurement was performed for different tilt angles of the sample mount. The acquired data allows a partial validation of the agreement of the divergence of the light source assumed in the RADIANCE simulation with the three lamps of the solar simulator.

Within this RADIANCE simulation, the lamps have been considered to be divided into 10x10 small light sources each, with each light source being a Lambertian radiator. Assuming that these 300 light sources represent the solar simulator, the irradiance on the surface of the PV cells in the front PV stripes and the back PV stripes can be simulated by ray tracing. For small tilt angles, the simulation of the solar simulator is not satisfying; for a more precise simulation, the divergence of the solar simulator has to be measured in detail. At high tilt angles, the simulated irradiance distribution is very satisfying; however, this agreement is only necessary, but not sufficient for a validation of the simulation of the solar simulator, as the exact directional characteristic of the irradiance is unknown. The gathered statistical results for the agreement are listed in Tab. 4.4.

Angle	**R^2[%]**	**RMSE**	**MBE**	**NU[%]**	$\overline{s.}$[W/m^2]	$\overline{m.}$[W/m^2]
0°	12.46	11.35	6.69	2.18	590.27	583.58
20°	46.39	11.18	8.15	3.08	560.25	552.11
45°	97.75	5.01	4.36	8.79	429.76	425.40
60°	99.74	1.64	−0.85	11.37	310.04	310.89

Table 4.4: Validation results for the RADIANCE simulation of the divergence of the solar simulator at different tilt angles of the sample mount. The *RMSE* and *MBE* values are given in W/m^2. In the fifth column, the non-uniformity calculated with Eq. 4.1 is listed; the sixth and seventh columns specify the arithmetic mean values of the simulated and the measured irradiances on the surface of the test sample.

The poor results for low tilt angles are caused by a small shift of the lamp irradiation axis to the center of the PV sample, which leads to inhomogeneous irradiation, also for a tilt angle of zero. At large tilt angles, this effect is totally outweighed by the inhomogeneous irradiance on the sample surface due to the lamp divergence. Regarding the non-uniformity of the irradiance on the sample, the solar simulator fulfills the IEC specifications of class C ($NU < 10\%$) at least for tilt angles less than or equal to 45°, while the specifications of class B ($NU < 5\%$) is fulfilled for incidence angles less than or equal to 20°.

The irradiance measurements have been made only for rotation of the sample plane around a vertical axis in one direction; all the PVShade® measurements described below were performed with sample rotation in the same direction as the irradiance measurements, for the direction of lower as well as for the direction of higher optical transmission of the PVShade® sample. For this reason, the sample had to be rotated by 180° around a horizontal axis and remounted for the I–V curve measurements in the direction of higher optical transmission.

Simulation of the effective irradiance for the front and back PV stripes of the PVShade® sample

For the simulation of the cell I–V curves from the irradiance on and the temperatures of the PV cells, the effective cell irradiance defined in subsection 2.4.1 has to be calculated. This calculation allows the calculation of cell I–V curves based on STC measurements. In the case of a PV module with an internal structure like PVShade®, the effective irradiances on the cells of the PV stripes in the front as well as of those in the back plane have to be calculated. A ray-tracing calculation includes the internal reflections in the sample.

A cross-section of the PVShade® sample is shown in Fig. 4.21.

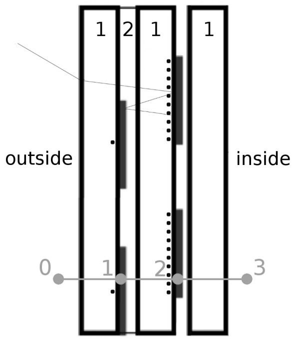

Figure 4.21: The interior composition of the PVShade® sample that has been measured in the g-value laboratory. The darker dots show the position of the grid points in the optical simulation. Darker numbers: 1: glass panel, 2: PVB interlayer; longish vertical areas: the PV cells, representing the layer sequence TCO/p-type a-Si/intrinsic a-Si/n-type a-Si/Al; lighter numbers: temperature nodes.

The comparison of the irradiance calculations by ray tracing to STC measurements is achieved by calculating the irradiance inside the glass, just in front of each TCO layer, for both planes of PV stripes. As the ray-tracing simulation has to be performed for a sensor point that is located inside the glass, the correction term of Eq. 3.11 has been applied.

As has already been mentioned, the three lamps that represent the solar simulator have been installed above each other. The chosen lamp configuration minimizes the variation of the irradiation on the sample along a vertical axis. As the PV stripes, which represent a series connection of 26 PV cells each, are also positioned parallel to the vertical axis, the losses due to electrical mismatch can be neglected. Therefore, the I–V curve of each PV stripe can be calculated by multiplying the voltage of one cell I–V curve with the number of cells per PV stripe. For the front PV cells, the irradiance has only been simulated for one grid point per PV stripe. To analyze the shading of the back PV cells due to the front cells, the average irradiance on one cell per stripe has been simulated by calculating the arithmetic mean of the irradiance on ten grid points distributed equidistantly along the vertical axis. The positions of all grid points can be seen in Fig. 4.21, while the results for the effective irradiance on the grid points are shown in Fig. 4.22, for the back and front row as well as for all the measured tilt angles.

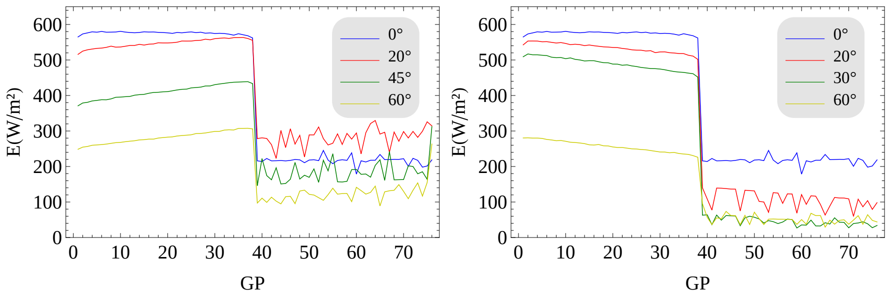

Figure 4.22: The simulated (average) effective irradiances on the PV cells. As each of the two PV planes of the sample has 38 stripes, the grid points (=*GP*) are numbered from 1 to 38 for the front plane of the sample, while the back stripes are counted from 39 to 76 along the abscissa. The back grid points are already the averaged results of 10 grid points each. The numbering sequence changes due to the rotation. Left: results for different tilt angles of the PVShade® sample in the direction of lower optical transmission. Blue: 0°, red: 20°, green: 45°, yellow: 60°. Right: results for different tilt angles in the direction of higher optical transmission. Blue: 0°, red: 20°, green: 30°, yellow: 60°.

The measurements were performed in both rotational directions: in the direction of lower optical transmission and in the direction of higher optical transmission of the PVShade® sample, corresponding respectively to less and more shading of the back cells by the cells of the front plane. Both rotations were made in the same direction with respect to the vertical axis; for the second measurement, the sample was rotated by 180° around a horizontal axis parallel to its surface normal.

As can be seen in Fig. 4.22, the simulation results show a slight variation of the irradiance results for the back sample plane. This may be caused by the low number of grid points; the result depends on the position of the grid points relative to the shading due to the cut-off angle. Nevertheless, as the PV stripes are connected in parallel with each other, the calculation of the sample I–V curve will average this variation, which makes the variation irrelevant. The results for the front sample plane show the inhomogeneity of the irradiance caused by the assumed divergence of the solar simulator.

Simulation of the PV cell temperatures

As shown in Fig. 4.21, the examined sample corresponds to the structure of Fig. 2.6, except that the two back glass panes have not been installed. Instead, a single glass pane has been mounted behind the amorphous silicon layers, leaving a small air gap in between. For the temperature simulation of the PV cells, the absorbed energy has been estimated, and the generated electricity that does not contribute to the PV cell temperature has been subtracted; then, the approach of subsection 2.7.2 has been followed. The larger amount of heat dissipated by the PV stripes of the back plane due to inhomogeneous radiation caused by the gap between the PV stripes in the front plane has been neglected. Four temperature nodes, located at the planes of PV stripes and the inside and outside environments (see Fig. 4.21), have been chosen. The heat transfer coefficients between these nodes can be calculated by Eq. 4.2.

$$h_{01} = \frac{1}{\frac{1}{h_e} + \frac{d_{glass}}{\lambda_{glass}}} \qquad h_{12} = \frac{1}{\frac{d_{PVB}}{\lambda_{PVB}} + \frac{d_{glass}}{\lambda_{glass}}} \qquad h_{23} = \frac{1}{\frac{1}{\Lambda^{air}_{eff}} + \frac{d_{glass}}{\lambda_{glass}} + \frac{1}{h_i}} \tag{4.2}$$

In the present case, the heat transfer coefficient of the air gap, Λ^{air}_{eff}, is the only parameter that is difficult to determine. It is composed of thermal conduction, convection and thermal radiation. Here, however, the heat transfer coefficient of the air gap is surely high enough to be neglected for the calculation of h_{23}, the heat transfer from node 2 to node 3, which is mainly influenced by the heat transfer coefficient to the inside of the chamber, h_i.

Finally, by applying Eqs. 4.3, the system of equations 4.4 has to be solved for the temperatures of the PV cells of both PV stripes.

$$\dot{q}_{01} = (T_a - T_{frontPV}) \cdot h_{01} \qquad \dot{q}_{12} = (T_{frontPV} - T_{backPV}) \cdot h_{12}$$
$$\dot{q}_{23} = (T_{backPV} - T_{int}) \cdot h_{23} \tag{4.3}$$

$$\dot{q}^{frontPV}_{abs} = \dot{q}_{10} + \dot{q}_{12} \qquad \dot{q}^{backPV}_{abs} = \dot{q}_{21} + \dot{q}_{23} \tag{4.4}$$

The measured ambient temperatures and simulated cell temperatures in the state with stabilized temperatures can be found in Tab. 4.5. The given values for the PV cell temperatures are the arithmetic means of the simulated PV cell temperatures of the PV stripe in the front and the back planes, respectively. For the simulation of the I–V curves of the sample, however, the temperatures of each cell is determined and used.

Tilt angle	$T_a[°C]$	$T_i[°C]$	$T_F[°C]$	$T_B[°C]$
0°	19.6	20.5	42.2	47.0
20°	19.5	20.1	43.2	47.6
45°	19.4	19.7	36.3	39.7
60°	19.1	19.3	30.7	33.0
-20°	19.7	20.7	37.8	42.6
-30°	19.3	20.6	34.3	39.0
-60°	19.1	19.4	27.8	30.1

Table 4.5: Measured exterior (T_a) and interior (T_i) temperatures during the electrical measurements at different tilt angles of the PVShade® sample, and simulated average temperatures of the front (T_F) and back (T_B) PV stripes. Negative tilt angles are defined as the rotation in the direction of optical transmission of the sample. Due to a small horizontal shift of the light source, the temperatures at positive tilt angles are slightly higher.

Simulation of the cell I–V curves with the two-diode model

The two-diode model simulates the low-light behavior and the temperature dependence of the cell I–V curve on the basis of a measured STC I–V curve of a PV cell or module, as discussed in subsection 2.5.1. In subsection 4.3.1, it was shown that the results of the two-diode model, especially concerning the low-irradiance behavior, are not satisfying for PV cells based on amorphous silicon. Nevertheless, for the case that the details of the PV module production are not known, the two-diode model is still the best existing model to predict the cell I–V curve. Furthermore, it has been observed that the metastability of a-Si:H PV cells and modules is difficult to handle; the I–V curve under the same measurement conditions can be different even when the PV sample, in between the measurements, has only been stored in the dark. To minimize the errors resulting from metastability issues, an I–V curve that has been measured directly in the g-value laboratory as part of this measurement campaign is applied as a basis for the two-diode model.

Fig. 4.23 shows initial measurements of the I–V curve of the front PV stripes at 25.1°C, shortly after the solar simulator had been started (to guarantee temperatures near STC). The irradiance on the sample (with the assumption of homogeneous irradiation along the vertical axis), measured with the reference cell, was $E = 527$ W/m^2. The spectral distribution of the light generated by the solar simulator is only guaranteed after warming up; this means, the latter irradiance value may need a spectral mismatch correction. However, the spectral power density of the solar simulator while warming up has not been measured.

Before the measurements started, the PVShade® sample had been light-soaked for two weeks. The light soaking was performed with an incidence angle of 30° in the direction of minor light transmission. Therefore, the PV stripes in the front and back planes can be considered to be stabilized. The process of measuring the

PVShade® sample in the g-value laboratory lasted one week, which seems short enough to justify the neglect of metastability effects on the I–V curve of the sample.

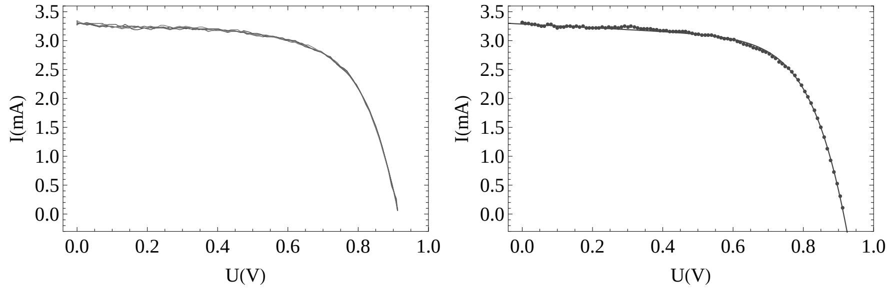

Figure 4.23: The simulation of the cell I–V curves, based on one initial I–V curve measurement in the g-value laboratory. The I–V curve of the PV stripes in the front plane of the sample has been measured. Left: five different quasi-cell I–V curves at a temperature of $25.1°C$ and irradiance of $E = 527\ W/m^2$, showing little variation. Right: one of the I–V curves of the left-hand graph (dotted) with the two-diode model fit (solid line). To perform the fit, the voltage of the measured I–V curve has been divided by the number of cells per PV stripe.

Following the procedure of section 2.5, the fit of the two-diode model parameters to the I–V curve of Fig. 4.23 has been performed. To make the procedure possible for an I–V curve at an irradiance of $E = 527$ W/m^2, a linear relationship between the photocurrent and the irradiance was assumed. The resulting parameters are: $I_{s1} = 1.54 \cdot 10^{-16}$ A, $I_{s2} = 1.79 \cdot 10^{-5}$ A, $R_s = 0.014\ \Omega$, $R_p = 3.14\ \Omega$, assuming $n_1 = 1$ and $n_2 = 3$. As in subsection 4.3.1, the temperature dependence of the I–V curves has been calculated by assuming a constant temperature coefficient for all currents and a constant temperature coefficient for all voltages. It has already been mentioned in subsection 2.5.1 that the only alternative, the two-diode model, shows obviously wrong results for the temperature dependence when applied to thin-film PV cells.

The resulting cell I–V curves for different irradiance and temperature values are shown in Fig. 4.24.

Simulation of the I–V curves of the PVShade® sample

After the simulation of the effective irradiance and the temperature at every PV cell, the I–V curves of the whole PVShade® sample can be simulated. This is done by the methodology described in section 2.6. For every tilt angle, both the I–V curves of the front and the back PV stripes have been measured. The simulated and measured I–V curves are shown in Figs. 4.25, 4.26, 4.27 and 4.28.

The measured I–V curves of the front PV plane and the back PV plane of the PVShade® sample allow an estimation of the simulation quality; however, there are a

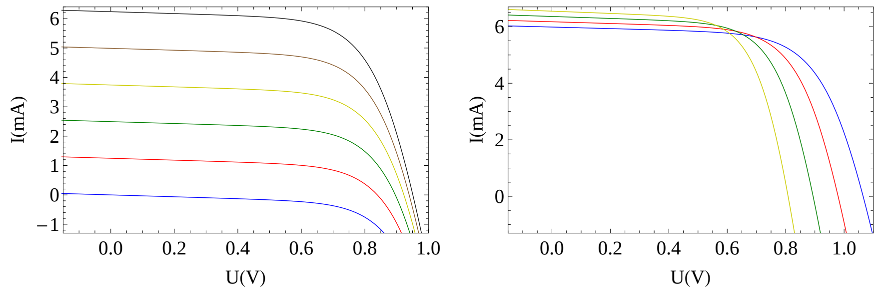

Figure 4.24: The resulting cell I–V curves when the two-diode model is applied. Left: cell I–V curves for one cell of the PVShade® sample for irradiance values from 0 (blue) to 1000 W/m^2 (black), in steps of 200 W/m^2, at 25°C; right: cell I–V curves for different temperatures, from −15°C (blue) to 75°C (yellow), in steps of 30°C, at a constant irradiance of 1000 W/m^2. (The two-diode model is not sufficient for thin-film PV cells at low temperatures. As indicated in Fig. 4.13, the open-circuit voltage of a PV cell based on amorphous silicon almost never exceeds 1 V.)

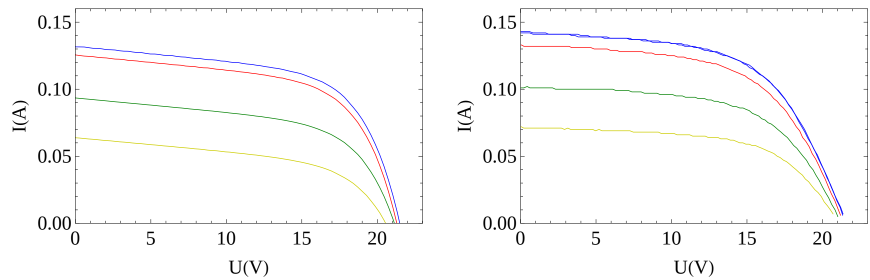

Figure 4.25: Simulated (left) and measured (right) I–V curves for the front PV plane of the PVShade® sample, with the measurement performed in the rotational direction of lower optical transmission. Blue: 0°, red: 20°, green: 45°, yellow: 60° tilt angle.

number of effects that cannot be measured independently of each other, which makes a validation of single simulation steps impossible. First, a validation of the ray-tracing calculation, especially for the reflections inside the PVShade® sample, demands a more detailed knowledge of the divergence of the solar simulator, as discussed earlier in this subsection. With high probability, the wrong sequence of the I–V curves in Fig. 4.26 for the tilt angles 0° and 45° can be traced back to the uncertainty of the divergence simulation for the solar simulator. Second, the I–V curves simulated by the two-diode model are not satisfactory, as described in subsection 4.3.1. The latter is responsible for the incorrect simulation of the PVShade® sample's low-light behavior shown in Fig. 4.28.

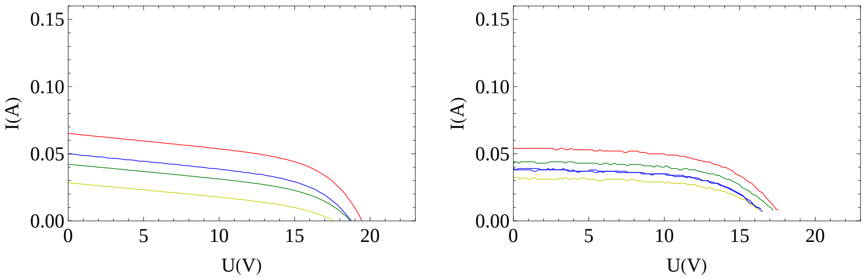

Figure 4.26: Simulated (left) and measured (right) I–V curves for the back PV plane of the PVShade® sample, with the measurement performed in the rotational direction of lower optical transmission. Blue: 0°, red: 20°, green: 45°, yellow: 60° tilt angle.

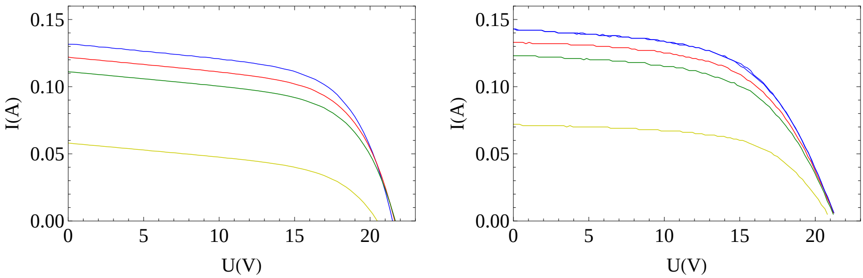

Figure 4.27: Simulated (left) and measured (right) I–V curves for the front PV plane of the PVShade® sample, with the measurement performed in the rotational direction of higher optical transmission. Blue: 0°, red: 20°, green: 30°, yellow: 60° tilt angle.

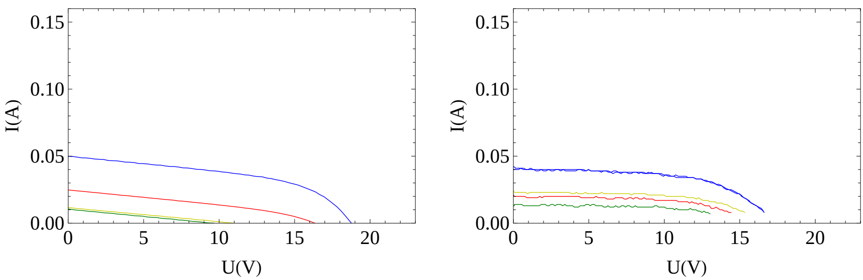

Figure 4.28: Simulated (left) and measured (right) I–V curves for the back PV plane of the PVShade® sample, with the measurement performed in the rotational direction of higher optical transmission. Blue: 0°, red: 20°, green: 30°, yellow: 60° tilt angle.

The DC power can be simulated by MPP tracking of the I–V curves of the PVShade® sample. When comparing the simulation results for the DC power with the measured DC power, the angle-selective behavior is reproduced quite well, as shown in Fig. 4.29. As expected, the power generated by the front PV plane is equal for positive and negative tilt angles of the sample, whereas the DC power of the back PV plane displays angular selectivity. The deviations between the measured and simulated DC powers are larger at higher incidence angles, which may be traced back to incorrect simulation either of the solar simulator irradiation or of the reflections inside the PVShade® sample.

In a future BIPV system made of PVShade® modules, the front and the back PV planes will be connected in parallel. The higher measured power values at high incidence angles show that the mismatch losses due to this parallel electrical connection will be low. Unfortunately, the described experiment does not allow a validation of the DC power simulation because neither the divergence of the solar simulator nor the low-light behavior of the a-Si:H PV cells could be analyzed separately.

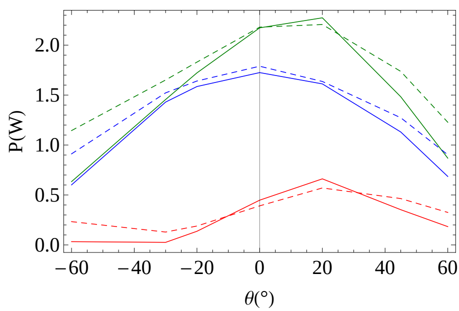

Figure 4.29: MPP values of the PVShade® sample at different tilt angles, measured in the *g*-value laboratory. Negative tilt angles represent the direction of higher light transmission. Blue: front PV plane, red: back PV plane, green: total power, considering each PV plane to be MPP-tracked independently. Dashed lines: measured values, continuous lines: simulation.

4.5 Electricity yield evaluation of photovoltaic systems

4.5.1 The PV roof system in Bad Krozingen

To validate the simulation of the electricity yield under partial shading conditions at the PV system level, the methodology has been applied to a PV system located on a (nearly) horizontal rooftop in Bad Krozingen near Freiburg. The geographical coordinates are: $47.9112°N$, $7.6961°E$. The PV system consists of 192 solar panels. The three PV module rows are divided into four sections with 16 PV modules each. For the investigations of the impact of shading on the time-dependent DC current, voltage and power, only 16 modules of the first and 16 modules of the second row are MPP-tracked, independently of each other. All optical and electrical analyses of the PV system are performed for the time period from March 22^{nd} to November 14^{th}, 2011. The modules of each row are connected in series; the PV system is oriented 57.5° SW, the modules are tilted at 30° relative to the roof, while the roof itself has a tilt angle of 2.6°.

The solar panels were manufactured by Sunways (module name: SM 215 WA63), and each consists of 60 PV cells made of crystalline silicon. Due to its importance for the time-dependent simulation of the DC voltage, current and power, the cell connection within each module is shown on the right side of Fig. 4.30.

Figure 4.30: Left: The *back* row of the two monitored module strings (the front row is not visible in the picture). Six silicon sensors that measure the irradiance in 5-minute steps are installed along the left-hand edge of the back row modules. Source: QPV group of Fraunhofer ISE. Right: The circuit diagram of a standard c-Si PV module made of 60 PV cells (here: Sunways SM 215 WA63). All c-Si cells are connected in series; one bypass diode protects 20 PV cells.

To analyze the shading on the back row caused by the front row, six silicon sensors are placed along the left-hand edge of the back module row as depicted in the photograph of Fig. 4.30. One silicon sensor is placed parallel to the front row to validate the irradiance without shading. Furthermore, the irradiance on the front row plane is also measured with a SPN1 pyranometer from Dynamax and a CMP11 pyranometer from Kipp&Zonen.

As the modules of both rows are installed in a "portrait" configuration, the shading of the lowest cell row of the modules in the back row will result in a significant power loss. Due to the position of the bypass diodes, none of the partially shaded PV module contributes to the system's DC power. In a "landscape" installation of the PV modules in the back row, two thirds of the PV module would still contribute when the lowest PV cells are shaded. For a validation of the shading loss calculation for BIPV systems, a "landscape" installation of the shaded modules would have been more applicable, but nevertheless, the measured data is very useful.

A gap between the PV modules in the front row has been closed with a wooden board, which simplifies the geometrical shading structure on the back PV module row. On this board, the irradiance sensors are installed, as depicted in Fig. 4.31.

Measurement and simulation of the irradiance on a PV module surface

Three different devices to measure the irradiance on the plane of the front PV module row have been installed, as shown on the right side of Fig. 4.31. A silicon sensor and a CMP11 pyranometer measure the total irradiance on the tilted plane, while the SPN1 measures the total and the diffuse fraction of the tilted irradiance at the same time. Due to the different spectral response curves of the devices, which are depicted in Fig. 2.4, the irradiance values measured by the CMP11 and SPN1 pyranometers and the silicon sensor, respectively, are different, as shown for one sunny day on the left side of Fig. 4.31. The differences in the measured irradiance are also caused by the different angular response of the measurement devices. For the validation of the simulated effective irradiance, the measurements with the silicon sensor are especially appropriate. Its spectral as well as its angular response are almost identical to those of the PV modules.

For the validation of the irradiance simulation at partially shaded locations, the irradiance on the silicon sensors depicted in Fig. 4.30 is calculated. As the angular response of the silicon sensor is identical to that of the PV modules, the effective irradiance of subsection 2.4.3 is used for validation. For the angular response function, the Martin/Ruiz model has been applied, using an a_R parameter of 0.157. The value of a_R has been determined for a crystalline PV module by measurements, as described in [36]. A quantitative analysis of the impact of the chosen angular response function on the simulated DC power will be given in subsection 4.5.4. The results of the simulation of the effective irradiance on the partially shaded silicon sensors on the back row for one day are shown in Fig. 4.32.

The most important simulation of the irradiance is the one for the position of the lowest irradiance sensor on the back row. The irradiance at this height of the back row is decisive for the electrical behavior of the PV system. Furthermore, the points of time when shading occurs can be validated. Also the precision of the sky radiance

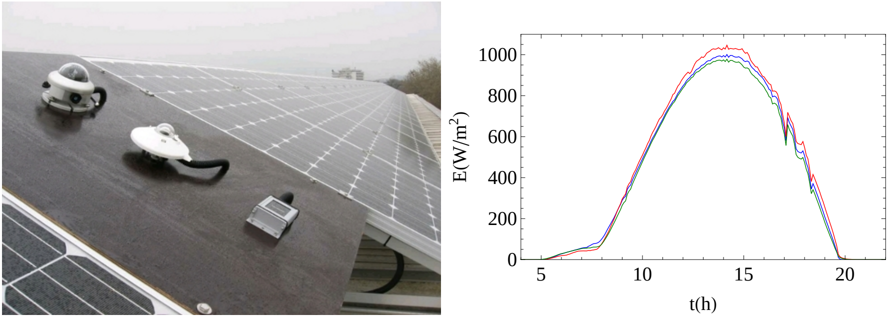

Figure 4.31: Left: the measurement devices installed in the front row of the PV system. From top to bottom: SPN1 pyranometer, CMP11 pyranometer, silicon sensor. The board on which the sensors are mounted ensures that the front row cast only a horizontal shadow onto the back row. Source: QPV group of Fraunhofer ISE. Right: irradiances on May 5^{th}, 2010, measured in 5-minute steps by the CMP11 pyranometer (blue), the SPN1 pyranometer (red) and the silicon sensor (green).

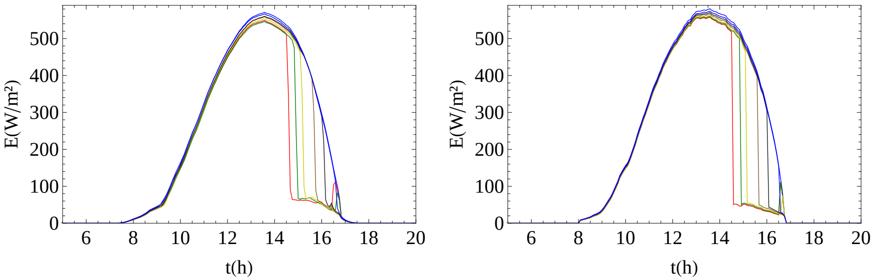

Figure 4.32: Irradiance on the partially shaded silicon sensors on November 12^{th}, 2010. Left: measured, right: simulated curves. The blue envelope curve represents the silicon sensor at the front, whereas the other colors depict the irradiance on the silicon sensors on the back row. The red, interior curve represents the lowest, most shaded silicon sensor on the back row.

distribution model can be validated for cases where only the diffuse light fraction reaches the silicon sensor.

The left side of Fig. 4.33 again shows the irradiance for November 12^{th}, 2011, on the lowest silicon sensor on the back row. The left side shows the agreement between simulation and measurement for the full day, including the small amount of direct sunlight passing through the gap below the wooden board of the front row. On the right side, the commencement of shading is shown in greater detail. As the ray-tracing simulations have been performed with only one grid point, that means with a point-shaped sensor, the irradiance drops completely from one 5-minute time step to the next. To take the dimensions of the silicon sensor into account, the ray-tracing simulation has to be performed with a grid of sensors. Finally, the arithmetic mean of the irradiance results could be derived. For the present case, however, the results are accurate enough with one sensor.

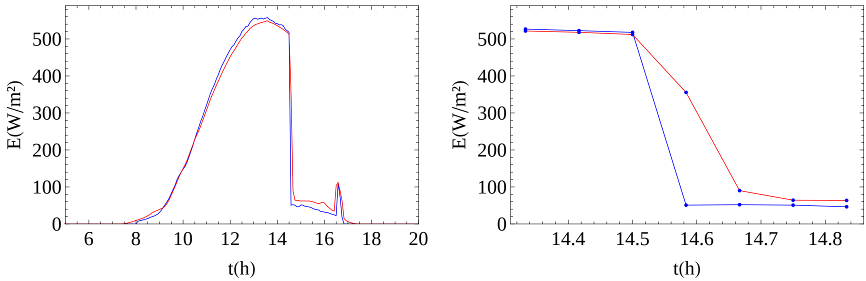

Figure 4.33: Left: Simulated (blue) and measured (red) irradiance on the lowest silicon sensor on November 12^{th}, 2011. The peak at 16:45 comes from the solar radiation through the empty space below the wooden board next to the front module string, depicted in the photograph of Fig. 4.31, that has been considered in the optical simulation. Right: The same curves in more detail around the start of shading. The silicon sensor is shaded partially for over ten minutes before it is fully shaded.

To quantify the performance of the irradiance simulation, Table 4.6 shows the results of the statistical measures described in Appendix A.

Si sensor	**R^2[%]**	**RMSE[W/m^2]**	**MBE[W/m^2]**
front	99.63	12.31	5.26
back, no.1	97.47	32.89	−3.00
back, no.2	98.59	24.83	3.23
back, no.3	97.80	31.62	−0.18
back, no.4	98.48	26.14	0.11
back, no.5	99.04	20.37	3.02
back, no.6	99.60	12.81	2.71

Table 4.6: Statistical measures for the irradiance simulation of the silicon sensors. The sensors for the back module row are counted from the lowest one upwards.

From these results, several conclusions can be drawn. First, the Perez model allows a very good simulation of the irradiance on a shaded silicon sensor. Second, the Perez model includes an implicit spectral correction; the assumption $MM_{spec} = 1$, described in subsection 2.4.1, leads to good results. However, it has to be kept in mind that the examined time period from March 22^{nd} to November 14^{th} excludes the winter months; it can be expected that the inclusion of the winter months would lead to slightly worse statistical results.

Simulation of the PV module temperatures

Three temperatures have been measured for the PV system in Bad Krozingen: the ambient temperature and the back surface temperatures of a PV module in the front row and of one in the back row. To reduce the error in the simulation of the system DC power, the measured PV module back surface temperatures are taken as a basis for the I–V curve modelling. The difference between the PV cell temperature and the back-surface temperature of the PV module is neglected. Nevertheless, the measurements of the PV module temperature can be applied to analyze the simulation accuracy of the linear approach described in Eq. 2.35, using an α value of 0.025 m^2K/W. For an arbitrary week, the measured and simulated PV module temperatures are plotted on the left side of Fig. 4.34. On the right side, the differences between both over the whole considered time period are shown. For the full considered time period, the statistical measures for the front row are: $R^2 = 92.35\%$, $RMSE$=3.40 °C, MBE=1.46 °C, and for the back row: $R^2 = 89.41\%$, $RMSE$=4.02 °C, MBE=2.16 °C. The measures are defined in Appendix A. Again, when interpreting the statistical results, the evaluated time period, from March to November, has to be considered.

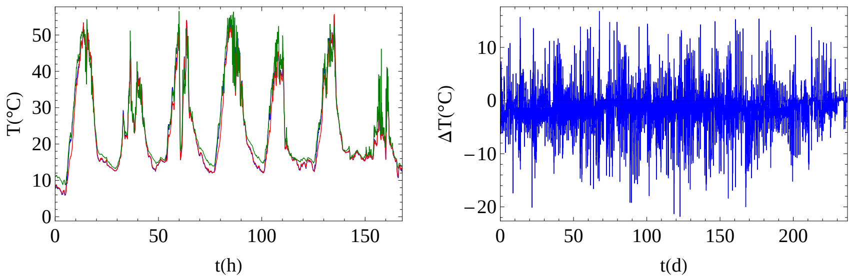

Figure 4.34: Accuracy of the linear temperature mode, validated with the temperature measurements from the PV system in Bad Krozingen. Left: module back surface temperature of the front (blue) and the back row (red), simulated values (green). Values for the time period from June 12^{th} to June 18^{th}. Right: measured temperatures minus simulated temperatures for the front PV module row, for the whole time period from March to November. No seasonal variations of the model accuracy are visible in the considered time period.

If the simulated temperature values had been taken for the simulation of the DC power, and the temperature coefficient of the MPP, γ, is assumed to equal $-0.44\%/K$, an $RMSE$ of approx. $4°C$ results in an error of the DC power of approx. 2%. That means, for free-standing PV plants, the linear temperature simulation can be accurate enough for calculating the DC power. For BIPV systems, the simulation of the temperature of the PV cells has to be performed in more detail.

Simulation of the I–V characteristics

For PV cells and modules based on the monocrystalline silicon technology, the two-diode model allows a very satisfying simulation of the low-light behavior and the temperature coefficients. First, the STC I–V curve of the PV module is measured. Then, the I–V curve of a "quasi-cell" is calculated by dividing the voltage by the number of PV cells connected in series in the module. The resulting I–V curve differs slightly from a "real" cell I–V curve due to the series resistance of the PV module that is higher than the sum of the series resistances of the cells. The two-diode model can be fitted to the resulting I–V curve, and the parameters of the two-diode model can be calculated.

The "quasi-cell" I–V curve and the fitted result of the two-diode model are shown in Fig. 4.35.

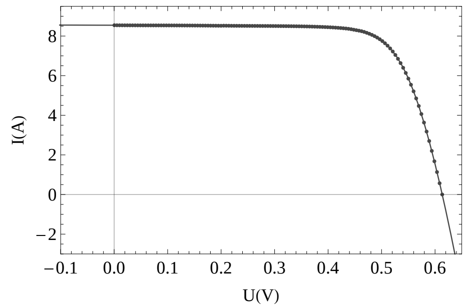

Figure 4.35: A "quasi-cell" I–V curve at standard test conditions that has been taken as a basis for the calculation of the I–V characteristics of the PV system. Dots: the resulting I–V curve when the voltages of the PV module I–V curve are divided by the number of series-connected PV cells per module. Line: the resulting STC I–V curve of the two-diode model after its parameters have been fitted to the "quasi-cell" I–V curve.

However, from the PV modules installed in Bad Krozingen, Sunways SM 215M (with a nominal power of 230 Wp), no STC I–V curve was available. Instead, an STC I–V curve of an unidentified PV module based on crystalline silicon with a similar short circuit current has been taken instead. The resulting parameters when fitting the two-diode model are: $n_1 = 1$, $n_2 = 2.295$, $I_{s1} = 3.146 \cdot 10^{-10}$ A, $I_{s2} = 3.252 \cdot 10^{-5}$ A, $R_S = 5.12 \cdot 10^{-3}\ \Omega$, $R_P = 11.92\ \Omega$. Assuming $\alpha\ [I_{sc}]$ to be 0.07 %/K, the I–V curves can be calculated for different operating temperatures. The resulting PV module specifications based on the simulated module I–V curves can be compared with the data sheet specifications in Tab. 4.7.

Except for the temperature coefficient of the MPP power γ, which has a quite high deviation of $6.8\%_{rel}$, the simulation results for the data sheet specifications suggest that the unidentified PV module and the two-diode model represent the installed Sunways PV module rather well.

SM 215M (230Wp)	Simulation	Data sheet	Error ($\%_{rel}$)
I_{sc} (A)	8.55	8.50	0.6
V_{oc} (V)	36.80	36.90	0.3
I_{MPP} (A)	7.95	7.86	1.1
V_{MPP} (V)	29.4	29.50	0.3
P_{MPP} (P)	233.58	230	1.6
FF (%)	74.22	74.27	0.0
α [I_{sc}] (%/K)	0.07	0.07	0.0
β [V_{oc}] (%/K)	–0.33	–0.34	2.9
γ [P_{MPP}] (%/K)	–0.41	–0.44	6.8

Table 4.7: Comparison of the simulated PV module specifications with those of the c-Si PV module Sunways SM 215M (230Wp) given in the data sheet.

Simulation of the current, voltage and DC power of the front PV module row

The simulation of the current, voltage and DC power of the front PV module row has been performed with the measured module temperatures and the simulated (effective) irradiance on the PV cells, following the approach described in section 2.6 and subsection 2.9.2. The results not only depend on the irradiance on and the temperature of the PV cells and the electrical properties of the PV modules, but also on the inverter that defines the voltage dependent on the exact shape of the I–V curve of the PV system. In general, small deviations of the simulated to the real system I–V curve can lead to rather large deviations in the system voltage and current, whereas the DC power deviations remain quite small at the same time. For three arbitrary days, Fig. 4.36 shows the resulting system voltages and currents for the front row, compared to the measured values. The calculation includes the simulation of the inverter that defines the system voltage.

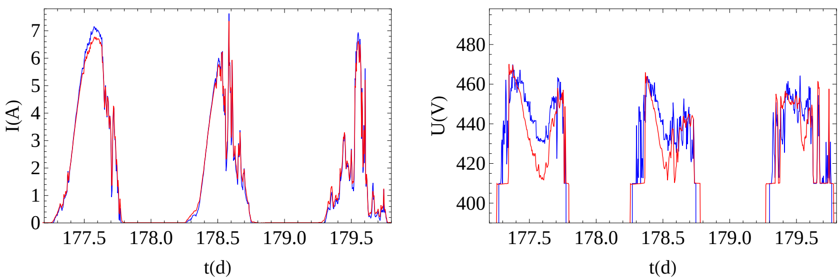

Figure 4.36: Time series of the system DC current and DC voltage for the front PV module row. Left: DC currents, right: DC voltages. Blue: simulated, red: measured.

Over the whole considered time period, the statistical measures for the simulation of the DC system current are: $R^2 = 98.09\%$, $RMSE$=0.32 A, MBE=0.03 A. The same calculation for the DC system voltage leads to the following measures: $R^2 < 0$, $RMSE$=89.61 V, MBE=-12.21 V. The latter statistical values are very poor. This can be traced back to incorrect simulation of the points when the inverter is switching on or off. The starting or stopping point of the inverter is difficult to simulate; first, the points are very sensitive to the simulated system voltage; furthermore, the measured voltages in the morning and in the evening are usually lower than the starting voltage of 410 V that has been specified in the data sheet.

The decisive DC power results for the same arbitrary days are shown in Fig. 4.37.

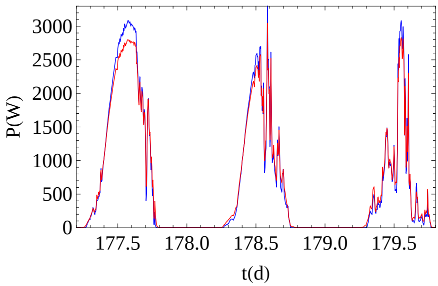

Figure 4.37: Time series of the DC system power of the front row. Blue: simulation, red: measurement.

The statistical measures for the DC power values over the complete time period of almost eight months are: $R^2 = 97.03\%$, $RMSE$=170.27 W, MBE=40.83 W. The results show that the bad statistical values for the DC system voltage can mainly be traced back to the morning and evening hours, when the DC system current is low anyway. However, only the R^2 value can be considered to be satisfying; the $RMSE$ and the MBE are rather high. The $RMSE$ divided by the arithmetic mean of the measured DC power values during the day yields 14.5%. As depicted in Fig. 4.37, the largest deviations appear at noon. The simulated results are higher than the measured ones, for both the DC current as well as the DC voltage. The reasons are: a high series resistance of the PV system (the distance between the PV modules and the inverter is around 100 m), dirt on the PV modules, a variation in the I–V characteristics of the PV modules that are connected in series, the difference in temperature between the PV cell and the PV module, the errors in MPP power and temperature coefficient. All the listed effects contribute to the difference between simulated and measured DC power values at noon. The deviations occur for both the front and the back PV module rows.

Simulation of the current, voltage and DC power of the back PV module row

The same investigations as for the front PV module row have been made for the partially shaded back row. Fig. 4.38 shows the simulated and measured results for the DC system current and voltage.

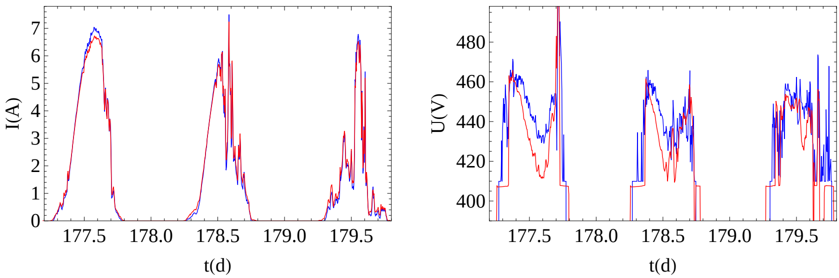

Figure 4.38: Time series of the system DC values for the back row. Left: DC currents, right: DC voltages. Blue: simulated, red: measured.

The statistical measures for the back PV module row are similar to the front row. The simulation of the DC system current results in $R^2 = 99.06\%$, $RMSE$=0.23 A, MBE=0.00 A, while the simulation of the DC system voltage leads to the following statistical values: $R^2 < 0$, $RMSE$=91.21 V, MBE=-8.82 V. Again, the DC system voltage simulation shows bad statistical values. However, these values can be traced back to errors that mainly occur at time periods with low DC current. In the afternoon of sunny days like day no.177 (September 14^{th}, 2011), the partial shading leads to a DC voltage peak, which has been reproduced in the simulation. If one of several PV modules, that are connected in series, is shaded, and the PV modules are protected with a bypass diode, the system I–V curve has a sharp bend in the first quadrant. This leads to two different local power maxima. If the inverter has the ability for shadow MPP tracking (see section 2.9), as it is the case for the installed inverter, the global MPP is tracked. Which of the two local maxima will be the global maximum depends on the number of PV modules connected in series and the level of shading. Here, the local maximum with the higher DC system voltage is the MPP.

The DC power results for the back PV module row, for the same arbitrary three days, are shown in Fig. 4.39. Also these results show deviations at high irradiance levels. The possible reasons have already been listed above.

As expected, compared to Fig. 4.37, the DC current and power of the back PV module row are cut off earlier in the day due to the shading caused by the front row. The resulting statistical measures of the DC power are: $R^2 = 97.98\%$, $RMSE$=140.97 W, MBE=33.83 W. The $RMSE$ divided by the arithmetic mean of the measured DC power values during the day yields 12.7%, which is of the same order of magnitude

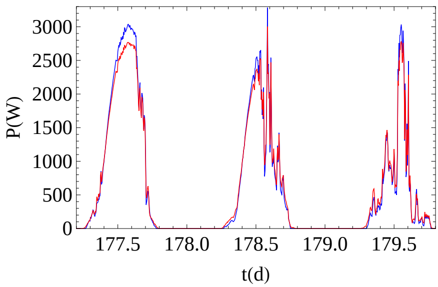

Figure 4.39: Time series of the DC system power for the back PV module row. Blue: measurements, red: simulation.

as the corresponding value for the front PV module row. However, the simulation of the impact of partial shading to the DC power can be considered to be validated.

The inverter efficiency

Both PV subsystems are MPP-tracked by a single inverter from the company Sunways Solar (NT 10000, with HERIC topology and a nominal output power of 10 kW). To simulate the efficiency of the inverter, the advanced Schmidt-Sauer model is applied. The specifications of the data sheet and the resulting efficiency curves are presented in Fig. 4.40. The European efficiency is specified with $\eta_{EUR} = 95.9\%$.

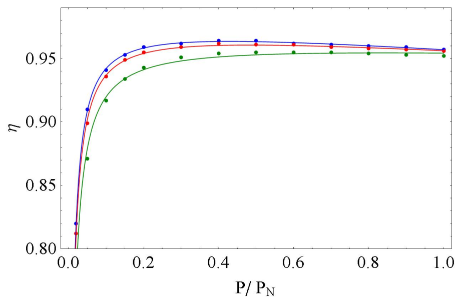

Figure 4.40: The efficiency of the Sunways NT 10000 inverter versus the input power relative to the nominal power, for different input voltages. The dots represent the values from the data sheet, the lines are the results from the Schmidt-Sauer model. Blue: 350 V, red: 415 V, green: 550 V DC voltage.

Applying Eq. 2.51 to the pairs of efficiency and DC input power, specified in the data sheet, for all three DC input voltages, the parameter fit leads to the (unitless) results shown in Tab. 4.8.

DC voltage	p_{self}	v_{loss}	r_{loss}
350 V	$3.99 \cdot 10^{-3}$	$1.92 \cdot 10^{-2}$	$2.17 \cdot 10^{-2}$
415 V	$4.20 \cdot 10^{-3}$	$2.36 \cdot 10^{-2}$	$1.80 \cdot 10^{-2}$
550 V	$5.07 \cdot 10^{-3}$	$3.57 \cdot 10^{-2}$	$0.72 \cdot 10^{-2}$

Table 4.8: Fitting results for the parameters of Eq. 2.51 (Schmidt-Sauer model considering the efficiency dependence on the DC voltage) when the model is applied to the data sheet specifications.

From the values of Tab. 4.8, the dependence of the efficiency on the DC voltage can be calculated by applying Eqs. 2.52 to 2.54. This procedure leads to the following values: $p_{self,0} = 5.23 \cdot 10^{-3}$, $p_{self,1} = -9.26 \cdot 10^{-6}$ V^{-1}, $p_{self,2} = 1.63 \cdot 10^{-8}$ V^{-2}; $v_{loss,0} = 1.26 \cdot 10^{-2}$, $v_{loss,1} = -2.14 \cdot 10^{-5}$ V^{-1}, $v_{loss,2} = 1.15 \cdot 10^{-7}$ V^{-2}; and $r_{loss,0} = 2.33 \cdot 10^{-2}$, $r_{loss,1} = 3.87 \cdot 10^{-5}$ V^{-1}, $r_{loss,2} = -1.24 \cdot 10^{-7}$ V^{-2}.

Finally, as the DC power as well as the AC power has been measured separately, the Schmidt-Sauer model can be tested. The measured DC voltage and DC power values have been taken as a basis for simulating the AC power for the whole time range. For the inverter of the front row, the comparison of the simulation results with the AC power measurements leads to an R^2 of 99.76%, an $RMSE$ of 46.98 W and an MBE of -40.10 W. Similarly, for the inverter of the partially shaded back row, the R^2 is 99.75%, while the $RMSE$ is 48.80 W and the MBE equals -42.00 W. The resulting statistical values represent a very high modeling accuracy which is mainly caused by the detailed data sheet specifications. The high MBE may be traced back to the long distance between the DC and the AC measurement devices (the inverter is located on the ground floor, at around 100 m distance to the PV system; the measurement device for the DC voltage is located on the roof).

A comparison of the extended to the original Schmidt-Sauer model is not possible for the PV roof system of Bad Krozingen. Only 16 modules are connected to the inverter, and there is a lack of measured efficiencies at high percentages of the nominal inverter power. However, the modeling accuracy of the original Schmidt-Sauer model, that does not consider the DC voltage dependence of the inverter efficiency, has been tested with the inverter of the saw-tooth roof BIPV system which is described below.

4.5.2 The BIPV saw-tooth roof of the Fraunhofer ISE main building

The next BIPV system that has been analyzed is the BIPV system in the saw-tooth roof of the Fraunhofer ISE main building in Freiburg, which was installed about twelve years ago. It was monitored for several years; the shading structure is still geometrically straightforward, without any trees or other difficult objects in the surroundings, but the shadow pattern is far more complex than for the PV roof system in Bad Krozingen. A photograph of the BIPV system from the inside of the Fraunhofer ISE main building and a RADIANCE image from a bird's eye perspective are shown in Figs. 4.41 and 4.42. The building is oriented exactly to the south, and the tilt angle of the PV modules is 32.5°; the geographical coordinates are: $48.0087°N$, $7.8347°E$. Due to the balustrade of the roof, the surroundings of the building can be neglected for the simulation of the irradiance on the BIPV modules. The shadow pattern on the BIPV modules is caused solely by the BIPV system itself.

Figure 4.41: A view of the saw-tooth roof BIPV system from the interior of the Fraunhofer ISE main building. The shadow pattern on the interior walls caused by the BIPV system is clearly visible. For lower solar altitude angles, the shadow pattern of one module row can be transmitted through the north-facing windows of the sawtooth structure onto the modules of the next row.

The BIPV system consists of 69 modules with 36 W_p each, installed in seven rows, with the first row consisting of four, the second of seven modules, and further rows as depicted in Fig. 4.42. Every module is made of 36 PV cells based on polycrystalline silicon.

To mitigate the effect of shading by the BIPV modules in front of a given row, the BIPV modules have been electrically divided into three parts. The 18 upper PV cells of every module are connected in series; furthermore, the lower 18 cells are divided again into two strings of 9 PV cells each. The two lower cell strings are both, but independently, connected in series to the corresponding lower cell strings of the other 69 BIPV modules; then, the two lower subsystems are connected in parallel to each other. The uppermost part of each module is connected in series with the uppermost section of the other BIPV modules, but two strings of 34 and 35 BIPV

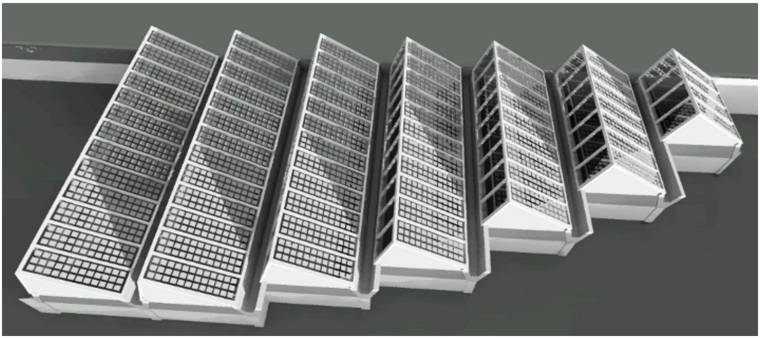

Figure 4.42: An image of the BIPV system from a bird's-eye perspective, rendered with RADIANCE, with January 16^{th}, 2005, 17:00 hours as the chosen point of time. The ray tracing allows the simulation of reflection (front modules of the second row) and transmission (small light spots in the shaded area of the back module rows).

modules, respectively, are formed; afterwards, these module strings are connected in parallel. The chosen electrical connection results in two PV subsystems with a nominal power of 1242 W_p each, the upper one being unshaded at noon throughout the year. A detailed circuit diagram can be found in Fig. 4.46.

The monitoring included the measurement of the global-horizontal and the diffuse-horizontal irradiance, the irradiance on a south-oriented plane at a tilt angle of 45° with a pyranometer[6], the irradiance on the PV module surface at a non-shaded position with a pyranometer, the outdoor air temperature, the back surface temperature of the BIPV modules, the DC voltage, current and power of both subsystems, and the AC power after each of the two inverters.

Simulation of the irradiance on the PV cells

As the simulation of the irradiance on every PV cell is rather time-consuming for this BIPV system, a time period of only one month, November 2005, has been evaluated. The irradiance results for an unshaded PV cell and further selected PV cells at different shaded positions are shown in Fig. 4.43.

In Fig. 4.42, some light spots can be seen on the surface of some BIPV modules. They are caused by the shadow pattern of the front module row due to radiation transmitted through the north-facing windows of the sawtooth structure. These patterns have consequences for the DC power of the whole system and have to be considered within the ray-tracing process. This process is based on pre-selected, individual grid points, as described in subsection 2.2.4. To be able to simulate the consequences of partial shading on a PV cell, every cell has been filled with 6x6

[6] This measurement was used for validation of the Perez sky model for tilt angles of irradiance measurement devices at southern orientations, presented in section 4.2.

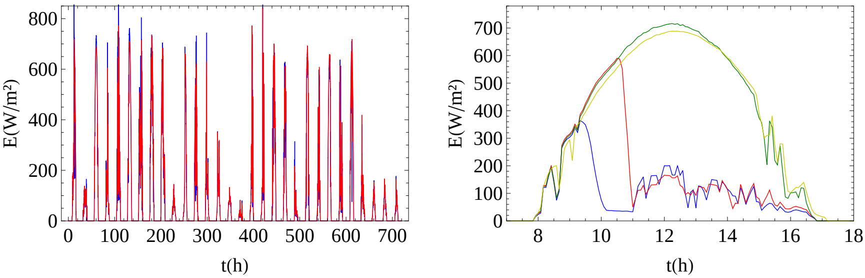

Figure 4.43: The time-dependent irradiance on the PV cells of the saw-tooth roof BIPV system. Left: simulated (blue) and measured (red) irradiance for November 2005 at a location without shading. Right: irradiance on the lower left cell for each sub-module of the first BIPV module in the second module row. Blue: lowest sub-module, red: middle section, green: uppermost section of the PV module. The yellow curve represents the irradiance measured by the pyranometer, which was installed at a different location, but at the same tilt angle as the modules. The rather high values of the blue and red irradiance curve after 11 a.m. can be traced back to the radiation transmitted through the module row in front of the analyzed one.

equidistant grid points each, leading to 2484x36 grid points. For all 5-min time steps in the month November, excluding the time steps during the night, the simulation of the irradiance on every PV cell requires around 350 million ray-tracing simulations; at the moment, the calculation lasts about 48 hours when distributed over 30 computer cores.

Comparing the simulated irradiance values for a non-shaded PV cell to the irradiance values measured by the tilted pyranometer, the statistical values, defined in Appendix A, for the whole month are: $R^2 = 93.12\%$, $RMSE$=56.62 W/m^2 and MBE=-7.14 W/m^2. These results are not as good as those from Bad Krozingen. There are two reasons. First, the measurements were made seven years ago, and the exact location of the pyranometer could not be identified. Second, the green curve on the right side of Fig. 4.43 clearly shows a deviation of the pyranometer from a true southern orientation. Nevertheless, the ray-tracing process has already been validated in subsection 4.5.1, where the silicon sensors and pyranometers were installed with more care.

The variation of the PV module I–V curve at STC

Every single module installed in the BIPV system of the saw-tooth roof was measured before installation; the I–V curves at STC of all three sub-modules of each BIPV module are available. However, the allocation to the installation position has not been documented. Nevertheless, the variation of the I–V curve in the first quadrant at STC can be analyzed. In Fig. 4.44, the STC I–V curves in the first quadrant of the uppermost part of twenty arbitrary BIPV modules are plotted.

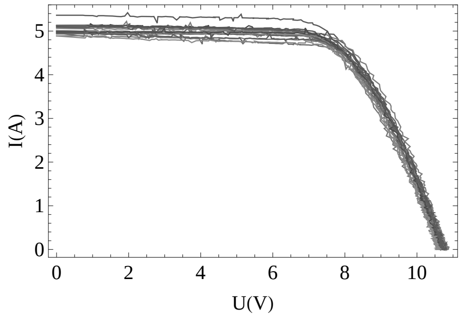

Figure 4.44: The STC I–V curves in the first quadrant for the uppermost part of twenty arbitrary PV modules installed in the BIPV system of the saw-tooth roof. The large variation is clearly visible.

The BIPV modules consist of PV cells produced by Shell Solar. Nowadays, the variation of PV cells based on polycrystalline silicon is much smaller. Mismatch losses due to the variation of the electrical properties of PV cells and modules can be minimized by sorting the modules; nowadays, the variation, at least for wafer-based PV technologies, is low enough to make the sorting process redundant. For PV modules made of thin-film technology, the variation of the electrical properties plays a more important role. In general, the quantitative level of this variation depends on the production process and therefore on the manufacturing company.

For the saw-tooth roof BIPV system, the sorting process has not been documented. Furthermore, with three separate sub-modules, sorting becomes complex.

Simulation of the I–V characteristics

For the simulation of the system I–V curves, the variation of the I–V curve of the BIPV modules has been neglected in general. This applies to both PV subsystems. Instead, it has been assumed that the I–V curves of all "quasi" PV cells, which are calculated by dividing the voltage of the sub-module I–V curve by the number of series-connected cells per sub-module, are identical to the one depicted in Fig. 4.45. The two-diode model was applied to fit this assumed average quasi-cell STC I–V curve. When the quasi-cell I–V curve is chosen as a basis for the calculation of the system I–V curve, the resistance losses within the PV module can be neglected.

With the two-diode model fit of the quasi-cell I–V curve, shown in Fig. 4.45, and the temperature dependences of the saturation currents I_{S1} and I_{S2}, following Eqs. 2.25 and 2.26, the temperature coefficients of the PV module can be calculated. Assuming $\alpha\ [I_{sc}] = 0.054$ %/K as specified in the data sheet, the two-diode model yields the temperature coefficients $\beta\ [V_{oc}] = -0.351$ %/K and $\gamma\ [P_{MPP}] = -0.486$ %/K. Compared to the values $\beta\ [V_{oc}] = -0.34$ %/K and $\gamma\ [P_{MPP}] = -0.46$ %/K specified in the data sheet, the deviations for the temperature dependence of the I–V curve

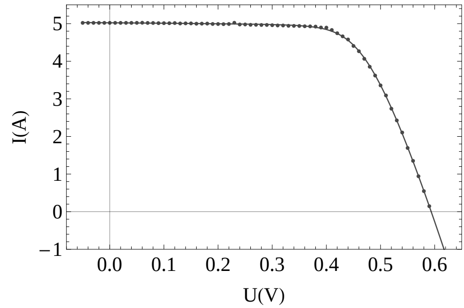

Figure 4.45: Quasi-cell STC I–V curve based on the measured sub-module I–V curve (dots) and fit of the two-diode model (solid line). The parameters of the two-diode model, resulting from the fit, are: $n_1 = 1$, $n_2 = 3$, $I_{s1} = 4.42 \cdot 10^{-10}$ A, $I_{s2} = 7.13 \cdot 10^{-5}$ A, $R_s = 0.019\ \Omega$, $R_p = 8.70\ \Omega$.

are quite low; therefore, also the impact of the error of the temperature-dependent I–V curve on the system I–V curve can be considered to be negligible. However, a validation of the low-light I–V curves given by the two-diode model would be desirable.

Temperature simulation

In section 2.7, the installed BIPV module has been applied as an example to describe a detailed method to calculate the PV cell temperature in a BIPV module. Furthermore, a cross-section of the BIPV module has been shown. The complete "BIPV module" is an insulating glazing unit with the PV module forming the outermost layer.

As has already been mentioned, the monitoring of the saw-tooth roof BIPV system included the measurement of the ambient temperature as well as the temperature of the glass pane at the back of the BIPV modules in a shaded position on the back of layer 6 in Fig. 2.14. For the validation of the temperature analysis, the irradiances measured by the pyranometer installed in the PV module orientation, and not the simulated irradiance, has been applied for the simulation. This avoids propagating the errors in the irradiance simulation to the validation of the temperature simulation. However, it has to be considered that the pyranometer is not oriented correctly.

From the measurement of the irradiance in the PV module orientation, the energy absorbed in the PV cells can be calculated. Applying a module reflectance value of $R = 0.225$ and an efficiency of 14%, taken from the STC I–V curve, for the glass-covered and encapsulated cell, a rough estimation of the absorbed energy contributing to the PV cell temperature can be made. The calculation leads to a factor of $(1-R)\cdot(1-0.14) = 0.682$ between E_{meas} and $(\dot{q}_{abs} + \dot{q}_{el})$. Compared to the linear temperature simulation approach of Eq. 2.35, this result corresponds to κ=0.029 Km^2/W, but with a small offset in the equation.

With the equations of subsection 2.7.2, the temperature of the PV cell and of the glass pane at the back of the BIPV module can be calculated. The latter can be compared to the measured temperatures. The resulting statistical values for the simulated and measured temperatures on the room-facing surface of the back glass pane over the full year are: $R^2 = 93.09\%$, $RMSE$=4.04 °C, MBE=-1.06 °C. The deviations are comparable to those of the PV module temperature simulation of the PV roof system in Bad Krozingen (see subsection 4.5.1).

Simulation of the system I–V curve

With the calculated effective irradiance and temperature for every PV cell, the system I–V curve can be calculated for every time step, as described in subsection 2.6.2. For series connections of PV cells, the voltage values of the quasi-cell I–V curves are added for every current value; for parallel cell connections, the current values are added for every voltage value. Also the electrical behavior of the bypass diodes installed parallel to every PV module is characterized by an I–V curve.

As has already been mentioned earlier in this subsection, the cell and module circuit of the BIPV system in the saw-tooth roof is rather complicated. All the modules are divided into three sections. The lower two sub-modules are each connected in series to the corresponding sub-modules of all the other modules, and these series connections are subsequently connected in parallel. The series connection of the uppermost sub-modules is divided into two module strings of 34 and 35 modules before these sub-module strings are connected in parallel. The DC electricity from the two BIPV subsystems is processed by two inverters. The cell and module connection details can be found in Fig. 4.46.

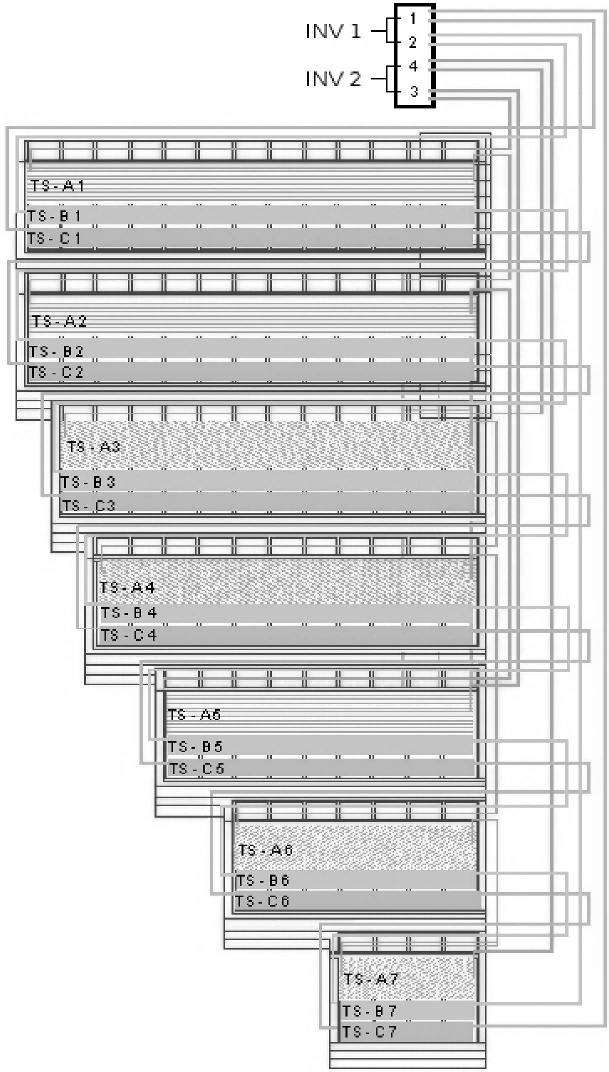

Figure 4.46: Circuit diagram of the saw-tooth roof PV system. There are four different circuits. No. 1 is the result of connecting all of the nine lowest cells per PV module in series. The same applies for no. 2, but with the next nine cells per module. The upper 18 cells per module are connected in circuits no. 3 and 4, with 3 standing for the series connection of the two 13-module rows which are positioned furthest north, combined with the 9-module row, which gives 35 modules altogether, while no. 4 is the result of combining the other 34 modules in series. Before the inverter, circuits no. 1 and 2 are connected in parallel, as well as circuits no. 3 and 4. Adapted from [34].

Simulation of the DC power: upper PV system

Both subsystems, the upper PV system consisting of the 18 uppermost PV cells in every module, and the lower PV system consisting of the 18 lowest PV cells, have been monitored by measuring the DC current, DC voltage and DC power. To calculate these DC values of the upper PV system, the simulated system I–V curve for every time step has to be compared with the voltage range of the inverter. Within this voltage range, MPP tracking leads to the final DC values; outside the voltage range, the inverter maintains the limit voltage, and the DC current is determined to be the current corresponding to this voltage.

The DC current and voltage values found by MPP tracking are quite sensitive to the exact shape of the system I–V curve, while the simulated DC power is much more robust. For this reason, the following validations are restricted to the comparison of measured and simulated DC power.

In Fig. 4.47, the time-resolved measured and simulated DC power during November 2005 is shown. The greatest deviations occur around midday, which can be mainly attributed to the variation of the electrical properties of the installed PV cells. Measurement of the system I–V curve would prove this assumption, as the shape of the I–V curve in the first quadrant would have small sharp bends. However, no measurement of the system I–V curve was performed for the saw-tooth roof BIPV system.

The simulation results for the DC power for the upper PV system show a statistical agreement to the measured DC power values of: $R^2 = 93.55\%$, $RMSE$=142.82 W and MBE=-30.50 W.

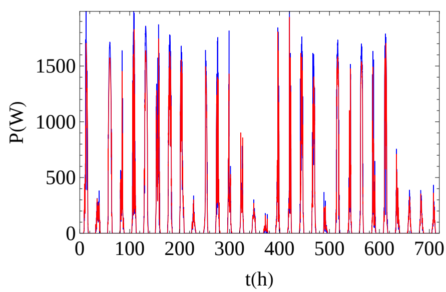

Figure 4.47: The DC power during November 2005 of the upper part of the saw-tooth roof BIPV system. Blue: simulated, red: measured DC power.

Simulation of the DC power: lower PV system

For the lower PV system, the simulation results are not so satisfying. The same analysis as with the upper PV system has been performed, which leads to the DC power results depicted in Fig. 4.48.

Although the simulation results visually seem to be good, the statistical measures are: $R^2 = 78.79\%$, $RMSE = 53.18$ W and MBE=-7.57 W. The combination of good $RMSE$ and bad R^2, compared to the results for the upper PV system, leads to the conclusion that only *some* time steps have very *large* deviations. The time-resolved DC power of one of the days that show large deviations, November 3^{rd}, is shown on the right side of Fig. 4.48.

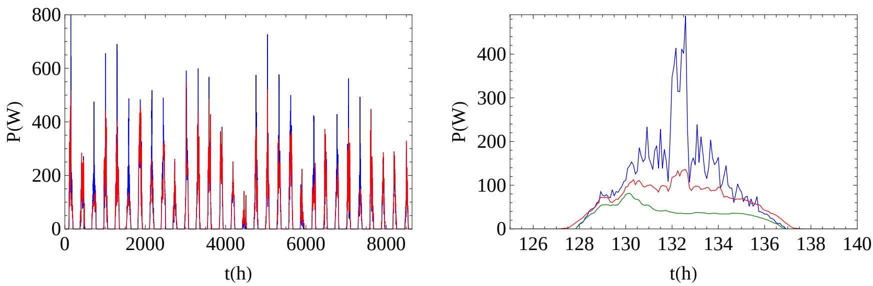

Figure 4.48: Simulated (blue) and measured (red) DC power time series for the lower part of the saw-tooth roof BIPV system. Left: full month November 2005; right: one day, November 3^{rd}, enlarged. The green curve on the right side shows the simulation result for the DC power if the radiation transmitted through each module row onto that behind it is neglected (the modules are simulated with zero transmission).

The right graph of Fig. 4.48 shows the measured (red) and simulated (blue) DC power for November 3^{rd}, where high deviations between both occur. When the north-facing window of every saw-tooth is replaced by a non-transparent material in the simulation, the simulation result of the DC power changes to the yellow curve of the picture. The results show that the light transmission through the PV module rows plays a surprisingly high role for the DC power. They also show that the increase in the DC power caused by light transmission is overestimated in the simulation. There are several possibilities for this error. First, the shape of the transmitted shadow pattern depends on the PV cell position and even on the mechanical deflection of the structures. A slightly asymmetric shadow pattern on the PV cells of the next module row can lead to a significant DC power decrease. Furthermore, for the ray-tracing process, the original plans of the building have been taken. These original plans do not include the installation of automized window openers on the north-facing sections of the saw-teeth. The installation required a thick window frame for stability reasons, which reduces the transmittance of the north-facing segments.

Furthermore, also other simulation errors have an effect on the results for the DC power. For example, the error concerning the low-light behavior simulated by the two-diode model has a higher impact on the lower PV subsystem because low irradiance values are more frequent there compared to the upper PV subsystem.

The inverter efficiency

The two PV subsystems of the saw-tooth roof BIPV system are connected to two inverters, model 20270 manufactured by the "Solwex" company. The nominal output power of the inverters is 2 kW, while the MPP voltage range is 190–350 V. Except for the specified maximum efficiency of 93%, no further information is included in the data sheet. Nowadays, the dependence of the efficiency on the AC power, sometimes additionally its dependence on the DC voltage, is defined in the data sheet. Therefore, for the installed inverters, the efficiency dependence on the output power is fitted to the measured DC and AC power, while the DC voltage dependence is neglected. This is done with the standard Schmidt-Sauer model, described in section 2.9. The fit leads to the following parameters. For the upper PV subsystem, $p_{self} = 1.05 \cdot 10^{-2}$, $v_{loss} = 6.93 \cdot 10^{-2}$ and $r_{loss} = 4.09 \cdot 10^{-2}$; for the lower PV subsystem, $p_{self} = 0.96 \cdot 10^{-2}$, $v_{loss} = 6.54 \cdot 10^{-2}$ and $r_{loss} = 3.26 \cdot 10^{-2}$. The efficiency for both inverters as a function of the output power fraction of the nominal inverter output power resulting from the Schmidt-Sauer model are shown in Fig. 4.49.

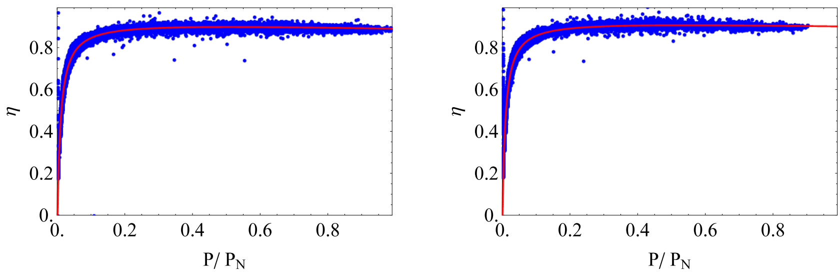

Figure 4.49: The inverter efficiency as a function of the output power fraction of the nominal inverter output power for the BIPV system in the saw-tooth roof. Blue: efficiency values based on the measurements of the DC and AC power of the PV subsystems; red: efficiency dependence on the AC power fraction, resulting from the Schmidt-Sauer model. Left: upper PV subsystem, right: lower PV subsystem.

When comparing the simulated AC power with the measured one, the resulting R^2 is 99.84% and 99.91%, the $RMSE$ is 21.07 W and 12.78 W, and the MBE is -0.21 W and 0.10 W, for the upper and lower subsystems, respectively. These statistical numbers show that, even when neglecting the dependence of the efficiency on the DC voltage, the Schmidt-Sauer model represents the inverter efficiency very well.

4.5.3 The thin-film PV system in Mochau/Dresden

An accurate electricity yield simulation for (BI)PV systems based on thin-film technologies like hydrogenated amorphous silicon (a-Si:H) requires quantitative knowledge of the metastability effect, which has been discussed in section 2.8. For the purpose of gathering this knowledge, the Signet Solar company located in Mochau/Dresden (coordinates: $51.11N, 13.18W$), now insolvent, provided 30 PV modules based on a-Si:H. With these PV modules, a free-standing PV system with a tilt angle of 30° and southern orientation was installed on a site near the factory of the company.

Figure 4.50: The PV system in Mochau, consisting of 30 PV modules based on amorphous silicon. The PV modules were manufactured by the company Signet Solar and are arranged in two rows of 15 PV modules each. Source: SunStrom

As depicted in Fig. 4.50, the PV modules have been installed in a single plane in two rows above each other of 15 PV modules each. A detailed monitoring system was included. The planning, installation, monitoring and analysis were all done within the Solarvalley BIPV project.

Within this subsection of the PhD thesis, the results of the electricity yield simulation are compared with the measurements of the DC power of this free-standing PV system. All analyses are performed on the basis of the measurement data from the period from June 1^{st}, 2010 to March 31^{st}, 2012. The PV system installation was completed before May 1^{st}, 2010; that means, the PV modules already had the time to change their metastability state according to the outdoor conditions before the analyzed period began.

Irradiance simulation

The irradiance was measured in the module plane (oriented south, tilted 30°) with a silicon sensor as well as with a pyranometer. Furthermore, satellite irradiance data (global horizontal, diffuse horizontal) for the investigated period have been bought for the geographical position 51.135° north, 13.193° east. While the satellite data has a 15-minute format, all the performed measurements lead to average values for every 5 minutes. 15-minute averages were calculated from the measured values to allow the data from both sources to be analyzed together.

The simulation of the irradiance on a surface with a tilt angle of 30°, using the Perez model for the sky radiance distribution, has already been validated in subsection 4.5.1 and led to an R^2 value of 99.63% and an $RMSE$ of 12.31 W/m^2. That result was achieved for an orientation of 57.5° SW, which leads to the conclusion that the model should be even better for the exact southern orientation of the PV system in Mochau. The high accuracy of the irradiance simulation with the help of the Perez model provides a good basis for a detailed analysis of the quality of the satellite irradiance data. Therefore, the irradiance on the tilted module surface has been calculated by using the Perez model based on the satellite data. The results of this calculation can be compared with the measured pyranometer values. The results are depicted in Fig. 4.51.

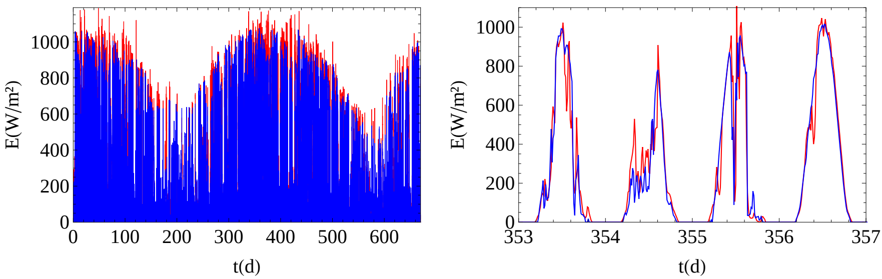

Figure 4.51: The irradiance on the module surface for the period starting on June 1st, 2010. Right: full considered time period, left: four arbitrary selected days. Blue: calculated irradiance on the PV module surface (derived from the horizontal satellite irradiance values), red: irradiance measured with the pyranometer mounted in the module plane.

Comparing both data sets of irradiance values in the module plane, the statistical values yield: $R^2 = 86.01\%$, $RMSE$=112.64 W/m^2 and MBE=0.09 W/m^2. Some of the discrepancy documented by these values may be due to snow lying on the pyranometer; however, the discrepancy is mainly caused by the sattopellite data basis. Hence, for the simulation accuracy, it makes a considerable difference whether horizontal irradiance values have been measured at the location of the PV system or have been derived from satellite measurements. At least, the annual totals are quite similar: 2420 kWh/m^2/a calculated, 2426 kWh/m^2/a measured annual total irradiation on the tilted module surface.

For this reason, it is important to know whether the measurement of a single pyranometer or silicon sensor in the PV module plane is sufficient to calculate the effective irradiance described in subsection 2.4.1. Therefore, the consequences of neglecting the angular response have been calculated with the following method.

For the angular response function of Eq. 2.15, the parameter value $a_R = 0.163$ has been chosen, as determined in the publication of Martin and Ruiz [36] for PV modules based on amorphous silicon. As a next step, the global-horizontal and the diffuse-horizontal irradiance values determined from the satellite measurements are applied for calculating the sky radiance distribution defined by the Perez model. Then, the irradiance on the PV module plane is calculated with the approach of Eq. 2.16, with and without considering the angular response function. The angular correction factor, i.e. the relative deviation between both results, is multiplied by the irradiance values measured by the pyranometer. This approach allows the effective irradiance to be calculated without the uncertainties coming from the satellite data. In Fig. 4.52, the resulting effective irradiance, the irradiance measured by the pyranometer and the difference between both are plotted.

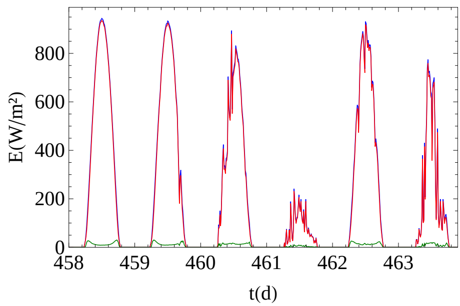

Figure 4.52: The irradiance on the tilted PV module plane of the thin-film PV system in Mochau/Dresden for six arbitrary days (Sept. 1st to Sept. 6th, 2010). Red: irradiance values, measured by the pyranometer; blue: the effective irradiance, calculated by multiplying the pyranometer values with an angular correction factor from the satellite measurements. green: the difference between the two.

As the yellow curve in Fig. 4.52 suggests, early and late in the day, the high incidence angle of the direct irradiance fraction leads to a peak in the deviation between the measured and the effective irradiance. For the annual irradiation, the resulting deviation between the simulated and measured irradiance is **3.23%**. The low value can be traced back to the temporal correlation between high incidence angles and low irradiance values. For orientations different from S/30°, and depending on the K function, the deviation for the annual irradiation can be larger. Detailed analyses of typical BIPV orientations are performed in subsection 4.5.4.

For the calculation of the effective irradiance on the plane of PV modules based on a-Si:H, the spectral mismatch MM_{spec} between a tilted pyranometer and the PV modules has to be considered. As this factor depends on the spectral distribution of the incident radiation, the calculation of this factor dependent on time requires detailed investigations. As has already been mentioned, MM_{spec} has been constantly set to 1 within this PhD thesis. The spectral corrections can be a field of future research.

Temperature analysis

Besides the measurement of the irradiance in the PV module plane by the pyranometer, the monitoring of the thin-film PV system in Mochau also involved the measurement of the ambient temperature as well as the surface temperature of the back glass pane of the PV modules on the upper and the lower module rows. With these measurements, two main aspects of the temperature simulation can be analyzed in detail. First, the measurements of the back surface glass temperature of the PV modules, averaged to 5–min time steps, allow the validation of the linear temperature simulation approach for glass-glass PV modules. Second, the measured ambient temperatures allow a quantitative analysis of the ambient temperatures given by the satellite measurements.

Based on the already determined effective irradiance, Eq. 2.35 has been applied to calculate the PV module temperature. The result has been compared to the measured back surface temperatures of both module rows. On the left side of Fig. 4.53, the differences between the measured ambient and the back surface temperature of the PV modules are plotted versus the calculated effective irradiance.[7] On the right side of Fig. 4.53, the ambient temperatures determined by the satellite measurements and the ambient temperature measured on-site are compared for arbitrary 20 days.

The simulation of the back surface temperature of the PV modules has been performed with the linear temperature model of Eq. 2.35, using a κ value of 0.025 m^2K/W. The comparison of the results with both measured back surface temperatures leads to the following statistical indicators. The back surface temperature measurements of the PV module in the lower row yield $R^2 = 95.45\%$, $RMSE$=2.92 °C, MBE=-0.03 °C, while the comparison to the measured back surface temperatures of a PV module in the upper row yields: $R^2 = 95.63\%$, $RMSE$=2.86 °C, MBE=0.22 °C. If the Pt100 measurements are reliable, the difference in the back surface temperature of the lower and the upper PV module rows is negligible.

Furthermore, the ambient temperatures derived by satellite measurements have been analyzed quantitatively, as depicted on the right side of Fig. 4.53. The resulting

[7] This will be the only graph with a cloud of data points along a linear function within this thesis for one reason. From a certain number of measurements on, the plotted graph does not display any statistical information although it seems to. Neither the simulation quality nor the variance can be read from the graph because the apparent variance depends on the number of points as well as on the dot size. All the information about the simulation quality is defined by the three statistical indicators used.

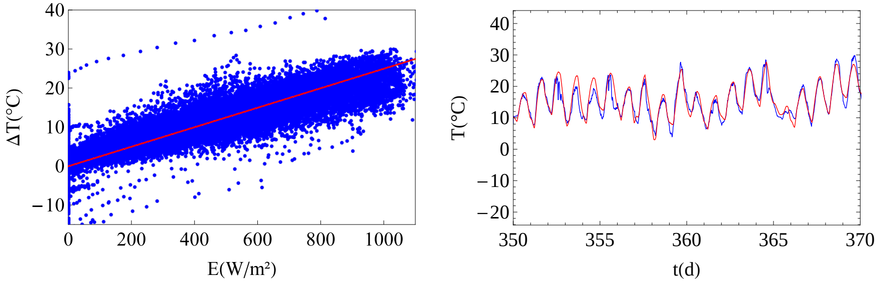

Figure 4.53: Temperatures of the thin-film PV system in Mochau. Left: The difference between the measured ambient and the PV module back surface temperatures plotted versus the calculated effective irradiance; the red line represents the linear function when applying Eq. 2.35. Right: The two ambient temperature data sets, plotted for arbitrary 20 days; blue: on-site measured ambient temperature, red: ambient temperature given by the satellite calculations.

statistical measures are: $R^2 = 92.83\%$, $RMSE$=2.42 °C, MBE=-1.21 °C. The satellite values are too high on average but reproduce the daily and annual temperature trends that were measured on site quite well. A reason for the large deviation may be that the ambient temperature measurements performed on-site in Mochau do not conform to measurement regulations of the official meteorological stations.

Simulation of the cell I–V curve

The cell I–V curve of the Signet Solar SI S4–95.A2 PV module has already been analyzed in association with the PVShade® test sample in subsection 4.4.2. The I–V curve of the test module at a temperature of 25.1°C and an irradiance of 527 W/m^2, measured in the g-value laboratory, has been applied for the calculation of the two-diode model parameters. This has been done by calculating the quasi-cell I–V curve from the measured one. Therefore, the open circuit voltage of the PV module can be calculated by multiplying the voltages of the cell I–V curve with the total cell number of 106. The module short circuit current can be determined by adapting the cell size.

The temperature dependence is assumed to be linear over the whole voltage and current scale of the first quadrant. The PV module properties resulting from the simulation with the two-diode model can be compared to the data sheet specifications in Table 4.9.

Most parameters in the table are within 3% of the datasheet specifications; the temperature coefficients show good agreement. The module voltage values are slightly too low, while the module current values are slightly higher than the given specifications. Besides the systematic errors, a possible variation of the material

SI S4–95.A2	Simulation	Data sheet	Error ($\%_{rel}$)
I_{sc} (A)	1.54	1.54	0.0
V_{oc} (V)	92.06	95.0	–3.1
I_{MPP} (A)	1.32	1.28	3.1
V_{MPP} (V)	72.08	74.2	–2.9
P_{MPP} (P)	95.15	94.98	0.2
FF (%)	67.1	64.9	3.4
α [I_{sc}] (%/K)	0.103	0.1	3.0
β [V_{oc}] (%/K)	–0.284	–0.3	5.3
γ [P_{MPP}] (%/K)	–0.201	–0.2	0.5

Table 4.9: Comparison of the simulated electrical values with the data sheet specifications for the PV module SI S4–95.A2. The power variation of the PV module at MPP is specified on the data sheet to be 3%.

parameters from PV module to PV module, which has not been investigated, may play an important role for the measured voltages and currents of the PV system.

Simulation of the DC power

The analysis of light soaking and annealing can be done by neglecting both effects in the simulation and comparing the simulated DC power results with the measured ones. Both DC power sequences, the simulated one based on the calculated effective irradiance and the simulated PV module temperatures, are depicted in Fig. 4.54.

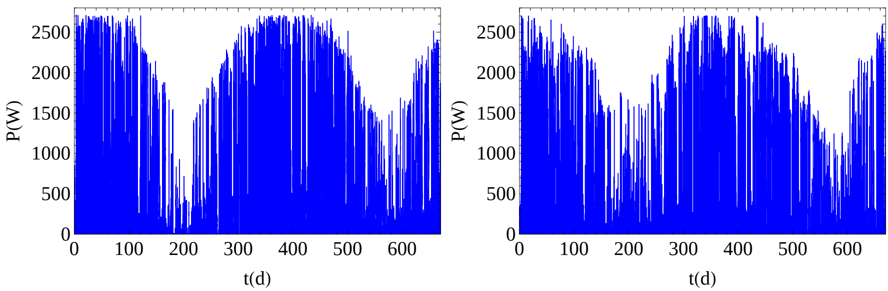

Figure 4.54: DC power of the thin-film PV system in Mochau for the whole time period from June 1st, 2010, to March 31st, 2012. Left: measured, right: simulated DC power. On both sides, inverter cut-offs are visible at approx. 2700 W as the inverter does not allow higher DC power values. The total energy yield of the considered time period is: 6038.2 kWh measured, 5176.15 kWh simulated. The difference can be attributed to the metastability effect.

Without considering light soaking and annealing, the statistical agreement of the system DC power is not good: R^2=84.55%, $RMSE$=300.58 W, MBE=-58.76 W. Especially the offset, represented by the MBE, is high, as is evident in Fig. 4.55, where the difference between measured and simulated DC power over the whole time period is depicted.

Independent of the instantaneously lower DC power due to high temperatures, the constantly higher temperatures during the summer months improve the a–Si material properties. It is only possible to analyze the metastability effect if the temperature-dependent and irradiance-dependent PV module behavior can be separated.

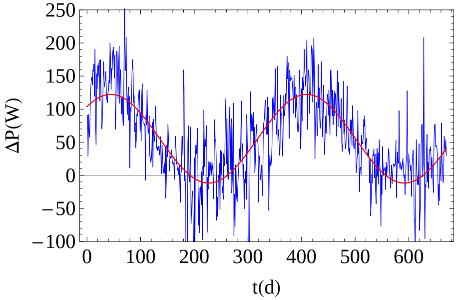

Figure 4.55: Difference between measured and simulated values of the daily mean DC power of the thin-film PV system in Mochau. Red: fitted curve of Eq. 4.5 with the parameters: $a = 67.02$ W, $b = 0.805$, $c = 55.29$ W.

The variation of the DC power difference with time can be fitted with Eq. 4.5, where x is the number of days since June 1^{st}, 2010.

$$\Delta P(x) = a \cdot \sin[x \cdot \frac{2\pi}{365} + b] + c \tag{4.5}$$

The most decisive resulting parameter is the amplitude $a = 67.02$ W. For a maximum DC power of 2700 W, this corresponds to a peak-to-peak-fluctuation of **5.0%**. Although the consequences of the metastability effect on the module I–V curve have not been investigated, Eq. 4.5 can be applied as a correction function for the electricity yield simulation of future PV system simulations. However, the precondition is the constant behavior of PV modules based on a-Si:H for different production lines.

Furthermore, also the change of spectral distribution of the incident radiation can play a role for the amplitude. In summer, the irradiation is generally blue-shifted, which increases the ratio between measured DC power and measured irradiance.

The inverter efficiency

An SMA SunnyBoy 2500 inverter was installed in the thin-film PV system in Mochau. The simulation of the inverter can be divided into two subtopics. First, the losses due to the restricted MPP voltage range may be simulated. Second, the efficiency dependence on the DC power, and optionally its dependence on the DC voltage, can be calculated.

For the thin-film PV system in Mochau, the simulation of the system I–V curves do not consider the metastability effect, which leads to high deviations for the system voltage. Therefore, the first subtopic cannot be simulated here; even the correction of the DC power with Eq. 4.5 will not be sufficient for this purpose, as the power correction does not automatically allow a voltage correction.

However, with the measured DC power and voltage and the AC power of the system, the second subtopic, the inverter efficiency, can be simulated. First, the data sheet specifications for the inverter efficiency have to be applied to calculate the parameters of the Schmidt-Sauer model; then, the AC power can be simulated on the basis of the measured DC power and DC voltage.

Fig. 4.56 shows the results. The data sheet specification for the inverter efficiency, dependent on the AC power and the DC voltage, lead to the following parameters of the advanced Schmidt-Sauer model described in section 2.9: $p_{self,0} = 8.59 \cdot 10^{-3}$, $p_{self,1} = -7.76 \cdot 10^{-6}$ V^{-1}, $p_{self,2} = 2.82 \cdot 10^{-8}$ V^{-2}; $v_{loss,0} = 2.35 \cdot 10^{-2}$, $v_{loss,1} = -2.16 \cdot 10^{-5}$ V^{-1}, $v_{loss,2} = 6.56 \cdot 10^{-8}$ V^{-2}; and $r_{loss,0} = 4.60 \cdot 10^{-2}$, $r_{loss,1} = -2.46 \cdot 10^{-5}$ V^{-1}, $r_{loss,2} = 3.63 \cdot 10^{-8}$ V^{-2}.

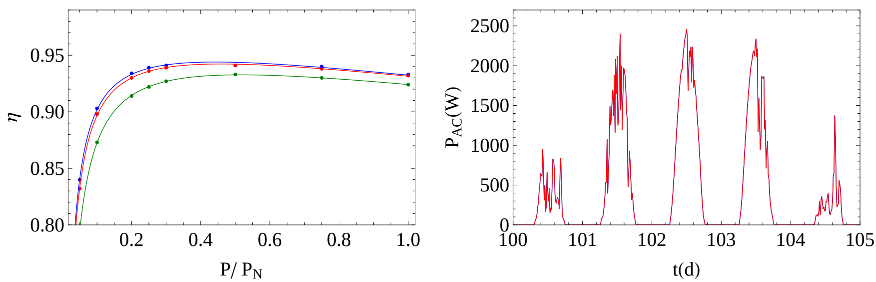

Figure 4.56: The simulation of the inverter efficiency. Left: The efficiency versus the output power fraction of the nominal AC power of the inverter, for different DC voltages. Dots: data sheet specifications, continuous lines: fitted results from the Schmidt-Sauer model. Blue: $U_{DC} = 224$ V, red: $U_{DC} = 300$ V, green: $U_{DC} = 480$ V. Right: measured (blue) and simulated (red) AC system power for arbitrary five days.

For the installed inverter, the comparison of the measured and simulated results for the AC power lead to the statistical values of: $R^2 = 99.9975\%$, $RMSE$=3.58 W and MBE=0.63 W. It can be concluded that the inverter works exactly as defined in the data sheet, and the model represents the efficiency dependence on the AC power for all DC voltages very well. That means, if future simulations show significantly poorer statistical values than the given ones, the conclusion may be taken that the inverter behavior does not correspond to the data sheet specifications.

4.5.4 The PV system at Ichtershausen/Erfurt

Within the Solarvalley BIPV project, also the parallel connection of differently oriented modules is analyzed. For BIPV systems that cover more than one side of the building, it is not immediately obvious whether differently oriented strings of BIPV modules should be connected in parallel, which leads to mismatch losses, or MPP tracked independently, which requires special inverters. An analysis of this situation is performed with the PV system at Ichtershausen/Erfurt with the geographical coordinates $55.88N, 10.97E$. The PV system consists of a-Si–μ-Si tandem PV modules manufactured by Masdar PV and started operation in July 2012. The circuit diagram of the whole PV system is shown in Fig. 4.57.

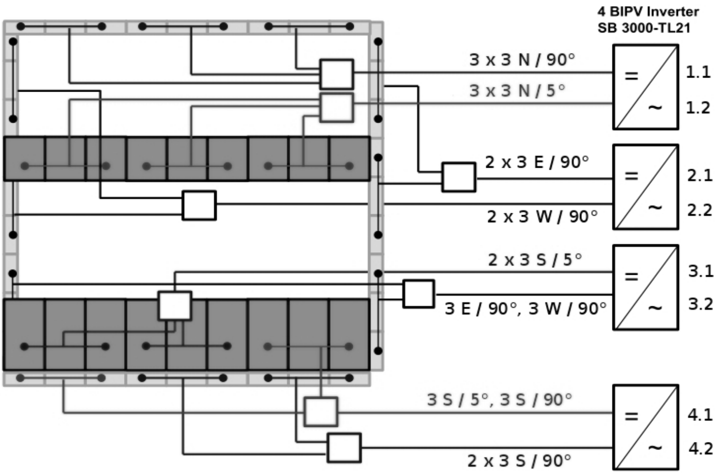

Figure 4.57: Schematic circuit diagram of the PV system in Ichtershausen. The MPP tracking is performed by four identical inverters, each with two independently MPP-tracked inputs. The structure of the PV system allows the comparison of the orientations $E/90°$ and $W/90°$ with their parallel connection (the inputs 2.1, 2.2 and 3.2) as well as the comparison of the orientations $S/5°$ and $S/90°$ with their parallel connection (the inputs 3.1, 4.2 and 4.1). There are no shading objects; the modules with the orientations $S/5°$ and $N/5°$ are installed above the vertical modules. Source: SunStrom

One aim of installing and monitoring this PV system is the analysis of electrical mismatch losses due to parallel connection. Within this PV system, the parallel connection of $W/90°$[8] and $E/90°$ is analyzed as well as the parallel connection of $S/30°$ and $S/90°$. Each orientation also exists as a separate PV system to allow a detailed analysis. The inverter no. 1 is not of high priority for the mismatch analysis,

[8]The PV subsystems are abbreviated according to their orientation and inclination. $W/90°$ is the abbreviation for the west-vertical PV subsystem.

but the installation of these north-facing module rows was of interest to other partners in the project consortium. The installed glass-glass modules have the same size as the modules in Mochau (1.1 x 1.3 m^2).

Irradiance simulation

The PV system has not yet been monitored for a sufficiently long time period to allow the simulation results to be validated. Furthermore, as the future weather cannot be predicted in detail, average global-horizontal and diffuse-horizontal irradiance values from the years 1981–2000 from the Meteonorm database [37], measured 11km away in Erfurt, were used for the calculation. Also the ambient temperatures have been acquired from the database.

In subsection 4.5.3, the difference between the irradiance on the tilted plane measured by a pyranometer and the effective irradiance, that considers the angular response curve, has been calculated. For the $S/30°$ orientation, the deviation of the annual irradiation was low (3.23%). The same analysis is performed in the simulation of the irradiance on the four main vertical module orientations. In Table 4.10, both annual irradiation and the percentual deviation between them are listed for all module orientations of the PV system.

In Figs. 4.58 and 4.59, the time-resolved simulated irradiance over the whole year and over arbitrary days is shown for the module orientations relevant for the following mismatch analysis.

Orientation	**E (kWh/m^2/a)**	**E$_{eff}$ (kWh/m^2/a)**	Dev. (%)
N/90°	331.0	313.2	5.7
N/5°	945.6	898.3	5.3
E/90°	639.5	615.6	3.9
W/90°	635.1	609.5	4.2
S/5°	1032.8	989.1	4.4
S/90°	834.0	797.6	4.6

Table 4.10: Annual irradiation on PV module surfaces of different orientations, with and without considering the angular response curve, and the deviation between the two quantities, for the orientations of the PV system of Ichtershausen. The orientations are: north-vertical (N/90°), northern with a tilt angle of 5° (N/5°), east-vertical (E/90°), west-vertical (W/90°), southern with a tilt angle of 5° (N/5°), and south-vertical (S/90°). For the chosen K curve, the losses due to the angular response are low even for vertical module orientations.

For the simulation of the effective irradiance values (Eq. 2.16) given in Tab. 4.10, an angular response curve has to be assumed. PV modules based on a-Si/μ-Si consist of two stacked PV cells that are connected in series to each other, which leads to a high open circuit voltage of a tandem PV cell. The disadvantage of tandem PV cells is the electrical mismatch between the two PV layers if the conditions are different from STC. Due to the increasing electrical mismatch between the two cell types

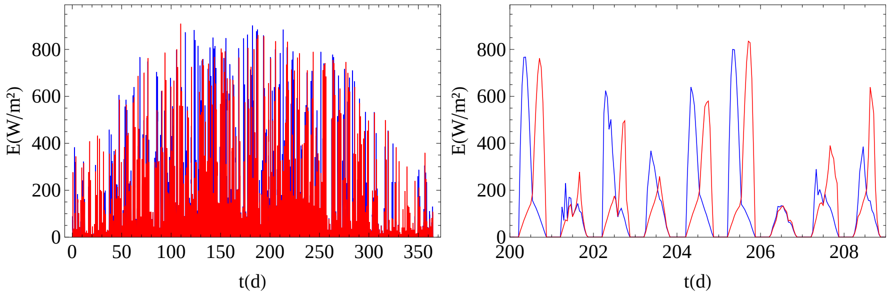

Figure 4.58: The simulated irradiance on the module surfaces of east-vertical (blue) and west-vertical (red) orientation, based on the Meteonorm data set. Left: full year, right: detail showing results for arbitrary days (July 19^{th} to July 27^{th}).

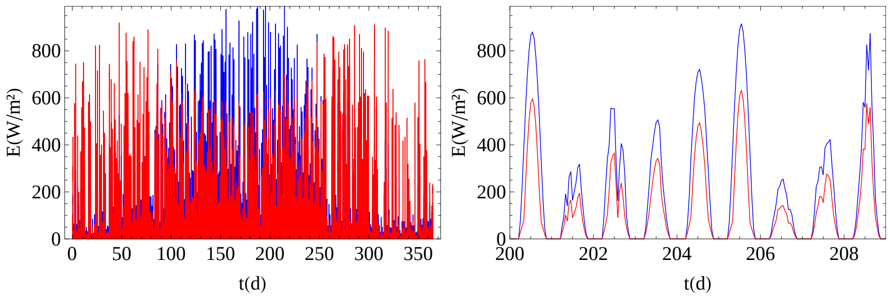

Figure 4.59: The simulated irradiance on the module surfaces with southern orientation and tilt angles of 5° (blue) and 90° (red). Left: full year, right: detail showing results for arbitrary days (July 19^{th} to July 27^{th}).

with higher incidence angles, it can be assumed that the K curve of Eq. 2.12 will drop more steeply at large incidence angles (see subsection 2.3.4) compared to the K curve of PV modules based on a-Si:H. However, as information on the angular response curve of PV modules based on a-Si/μ-Si was lacking, the same parameter of the Martin/Ruiz model as for PV modules based on a-Si:H has been assumed ($a_R = 0.163$), and the electrical mismatch between the two PV layers of the tandem cells has been neglected. Besides the annual irradiations given in Tab. 4.10, the time-resolved effective irradiance with and without considering the angular response curve, including the difference of the two, is shown for the western orientation and arbitrary days in Fig. 4.60.

Temperature analysis

The simulation of the PV module temperatures has been performed according to Eq. 2.35, assuming the standard proportionality factor of κ=0.025 Km^2/W for free-

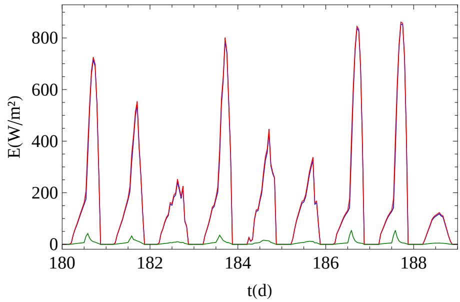

Figure 4.60: Time-resolved irradiance on the PV module plane at west-vertical orientation, with (blue) and without (red) consideration of the angular response curve, and the difference between the two curves (green). For the west-vertical module orientation, high irradiance values and large incidence angles are synchronous. As expected, the deviations are highest on sunny days near noon.

standing PV systems. The back surfaces of the PV modules are not thermally insulated, so the linear assumption from free-standing modules is assumed to be applicable. The results for the temperatures of the PV modules relevant for the mismatch analysis can be read in Fig. 4.61. Again, the time-resolved temperatures for the full year and for arbitrary days are depicted.

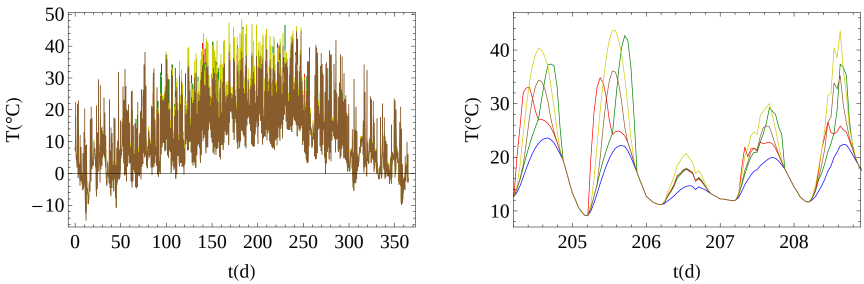

Figure 4.61: Simulated temperatures of the four vertical PV module rows of the PV system in Ichtershausen. Left: the time-resolved temperature results for the whole year; right: the same for arbitrary five days (July 23^{rd} to July 27^{th}). Blue: ambient temperature; other colors: temperatures for the east-vertical (red), west-vertical (green), S/5° (yellow), south-vertical (brown) PV module orientation.

Simulation of the module I–V curves

The basis for the simulation of the irradiance-dependent and temperature-dependent module I–V curves is a measured STC module I–V curve supplied by MasdarPV. The measurement was made immediately after production, meaning that no light-soaking has taken place. For the simulation, it is assumed that all the installed PV modules have the same electrical properties. Light soaking and annealing effects are neglected as their consequences for the irradiance-dependent module I–V curve are still unknown. Fig. 4.62 shows the two-diode model fit of the quasi-cell STC curve.

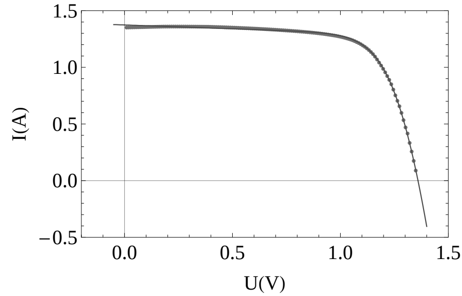

Figure 4.62: Quasi-cell STC I–V curve from the STC measurement of a PV module from MasdarPV (a-Si/μc-Si tandem PV technology, with an area of 1.4 m^2). Dots: measured STC I–V curve, with the voltage divided by the number of PV cells; solid line: two-diode model fit.

Due to the series connection between the a-Si:H and the μc-Si p-i-n junction, PV cells based on this tandem PV technology have a high cell open circuit voltage. For the PV modules of MasdarPV, the open circuit voltage of one quasi-cell is 1.381 V. The parameters of the two-diode model that result from fitting are: $I_{s1} = 1.88 \cdot 10^{-24}$ A, $I_{s2} = 2.4 \cdot 10^{-8}$ A, $R_S = 0.061\ \Omega$, $R_P = 14.84\ \Omega$. The ideality factors are assumed to equal $n_1 = 1$ and $n_2 = 3$.

The two-diode model leads to the low-light behavior shown in Fig. 4.63. Again, the temperature dependence of the quasi-cell I–V curve cannot be calculated with the two-diode model; obviously, Eqs. 2.25 and 2.26 are not valid for thin-film PV technologies in general. However, as has already been described in subsection 4.4.2, the assumption of a constant temperature coefficient for all voltage values and another constant temperature coefficient for all current values can be taken. The resulting temperature coefficients $\alpha\ [I_{sc}] = 0.103$ %/K, $\beta\ [V_{oc}] = -0.373$ %/K and $\gamma\ [P_{MPP}] = -0.297$ %/K are sufficiently similar to the three temperature coefficients $\alpha\ [I_{sc}] = 0.1$ %/K, $\beta\ [V_{oc}] = -0.37$ %/K and $\gamma\ [P_{MPP}] = -0.3$ %/K given in the data sheet. This linear approach of simulating the temperature dependence of the module I–V curves is valid as long as the temperature coefficients themselves are not temperature-dependent. On the right side of Fig. 4.63, the quasi-cell I–V curves at different module temperatures are depicted.

Simulation of the DC power and analysis of the electrical mismatch

With the significant assumptions of neglecting the metastability and accepting the low-light behavior of the PV modules given by the two-diode model, the DC power of all six PV subsystems can be simulated, and the mismatch losses due to the parallel

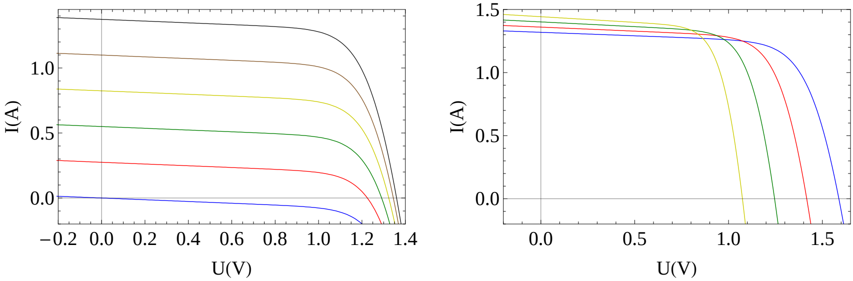

Figure 4.63: The quasi-cell I–V curves resulting from the fitted parameters of the two-diode model, based on the STC module I–V curve measurement supplied by MasdarPV. Left: I–V curves for variable irradiance values from 0 (blue) to 1000 W/m^2 (black) in steps of 200 W/m^2 at a constant temperature of 25°C; right: I–V curves at variable temperatures from −15°C (blue) to 85°C (yellow) in steps of 30°C at a constant irradiance of 1000 W/m^2.

connections of PV module strings, according to Eq. 2.34, can be calculated. Besides the mentioned assumptions, also the variation between the I–V curves of different PV modules or even PV cells is neglected; all simplifications influence the resulting electrical mismatch loss. However, the result of the mismatch calculation gives an impression of its order of magnitude.

The annual DC energy yield is summarized in Tab. 4.11. For the comparison of the annual energy yield of the PV subsystems, it should be noted that some PV subsystems consist of six, others of nine PV modules.

System	Orientation	Yield (kWh/a)
1.1	3x3 N/90°	199.1
1.2	3x3 N/5°	919.1
2.1	2x3 E/90°	391.3
2.2	2x3 W/90°	381.0
3.1	2x3 S/5°	690.3
3.2	3 E/90° + 3 W/90°	375.6
4.1	3 S/5° + 3 S/90°	614.5
4.2	2x3 S/90°	544.3

Table 4.11: Simulated annual energy yield for the eight subsystems on the DC side (before the inverter). Note the different module numbers while comparing. The orientations are: north-vertical (N/90°), northern with a tilt angle of 5° (N/5°), east-vertical (E/90°), west-vertical (W/90°), southern with a tilt angle of 5° (N/5°), and south-vertical (S/90°).

For the whole year as well as for arbitrary days, the time-resolved DC power for the eastern and western PV subsystems 2.1, 2.2 and 3.2 is depicted in 4.64. Furthermore, the time-resolved mismatch loss of subsystem 3.2 is shown in the figure, which equals the difference in DC power between subsystem 3.2 and the sum for subsystems 2.1 and 2.2. Fig. 4.65 shows the same results for the time-resolved DC power of the south-oriented PV subsystems 3.1, 4.2 and 4.1.

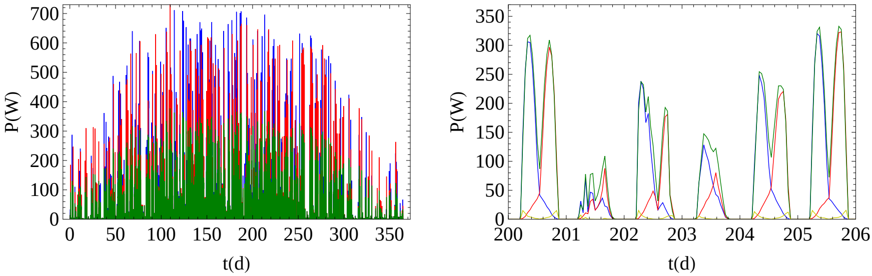

Figure 4.64: DC power results for the PV subsystems 2.1, 2.2 and 3.2; left: for the full year and all installed PV modules; right: for arbitrary days (July 20^{th} to 25^{th}) and three PV modules per orientation, simplifying the comparison. Blue: subsystem 2.1 (east-vertical orientation), red: 2.2 (west-vertical orientation), and green: 3.2 (parallel connection of eastern and western orientation); yellow: time-dependent mismatch (difference between the sum of the blue and red curves and the green curve).

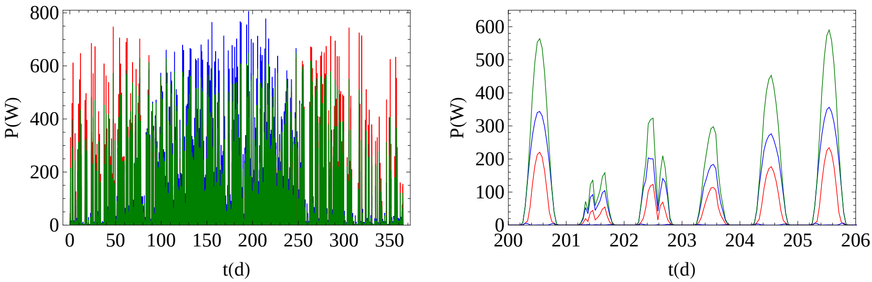

Figure 4.65: DC power results for the PV subsystems 3.1, 4.2 and 4.1; left: for the full year and all installed PV modules; right: for arbitrary days (July 20^{th} to 25^{th}) and three PV modules per orientation, simplifying the comparison. Blue: subsystem 3.1 (southern orientation with 5° tilt angle), red: 4.2 (south-vertical orientation), and green: 4.1 (parallel connection of the different tilt angles of the southern orientation); yellow: time-dependent mismatch (difference between the sum of the blue and red curves and the green curve).

With the DC power results, the annual mismatch loss can be calculated. For the PV subsystem 3.2 that combines the PV module strings of west-vertical and east-vertical orientation, the annual mismatch loss is **2.8%**. The PV subsystem 4.1, combining the orientations S/5° and S/90°, yields a mismatch loss of **0.5%**.

Due to the asynchronous course of the irradiance on the two strings of subsystem 3.2, its higher mismatch loss is understandable. Despite the simplifications made for the simulation, the result indicates that parallel connections of PV modules that are oriented in very different directions do not lead to severe DC power losses. As long as a higher ratio of DC current to DC voltage can be handled by the inverter, the parallel connection seems to be a good alternative to installing an inverter with two MPP trackers.

In general, the mismatch loss strongly depends on the low-light behavior of the V_{MPP}. This behavior again depends on the series resistance of the PV module as well as on its fill factor.

The parallel connection of PV module strings of two different orientations may lead to a reverse current through the PV modules exposed to less irradiation. This reverse current has also been calculated, resulting in a maximum negative value of $-0.047A$ for subsystem 3.2 and $-0.0041A$ for subsystem 4.1. The reverse currents are negliglible in this case, assuming that the inverter tracks the MPP reliably. Larger negative values of the reverse current may occur if the inverter is switched off! The reverse current will be larger at open circuit voltage than for the system MPP voltage.

Furthermore, blocking diodes are not necessary for the two PV subsystems. They even should be avoided due to their series resistance, which leads to rather high losses in the DC system power.

Inverter analysis

The installed inverter SMA SunnyBoy 3000TL-21 has two independent MPP trackers; this concept aims to enhance the total PV system power by reducing losses due to electrical mismatch.

First, it is examined whether the MPP voltage range of the inverter fits the PV subsystems. The data sheet of the inverter specifies a minimum MPP voltage of 150 V, a maximum DC voltage of 440 V and a maximum DC power of 3200 W. The maximum DC current is 17 A. In the PV system in Ichtershausen, the latter two limits are not exceeded by any of the six PV subsystems.

For all the PV subsystems, the losses due to the limited MPP voltage range can be calculated. For system DC voltages that are outside the MPP voltage range, no MPP tracking is performed. Instead, the voltage is kept at the limit value, which also defines the system DC current. However, the simulations show that the system DC power loss due to the limited MPP tracking is less than **0.83%** for all subsystems and highest for subsystem 1.1.

The dependence of the inverter efficiency on the AC power is simulated with the Schmidt-Sauer model. The data sheet specifications and the simulation results for the inverter efficiencies are shown in Fig. 4.66.

The resulting parameters of the advanced Schmidt-Sauer model (see section 2.9) are: $p_{self,0} = 7.63 \cdot 10^{-3}$, $p_{self,1} = -1.76 \cdot 10^{-5}$ V^{-1}, $p_{self,2} = 3.35 \cdot 10^{-8}$ V^{-2}; $v_{loss,0} = 6.28 \cdot 10^{-2}$, $v_{loss,1} = -2.42 \cdot 10^{-4}$ V^{-1}, $v_{loss,2} = 3.38 \cdot 10^{-7}$ V^{-2}; and $r_{loss,0} = -1.69 \cdot 10^{-2}$, $r_{loss,1} = 1.36 \cdot 10^{-4}$ V^{-1}, $r_{loss,2} = -2.09 \cdot 10^{-7}$ V^{-2}.

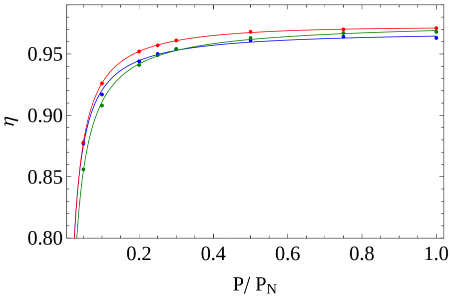

Figure 4.66: The inverter efficiency dependence on the AC power and the DC voltage for the SMA SunnyBoy 3000TL-21 inverter. Dots: data sheet specifications, lines: resulting efficiency curves of the Schmidt-Sauer model. Blue: $V_{DC} = 175$ V, red: $V_{DC} = 400$ V, green: $V_{DC} = 500$ V.

Surprisingly, the standard as well as the advanced Schmidt-Sauer model fail for inverters with more than one MPP tracker. The abscissa of Fig. 4.66 is the ratio of the total AC power processed by the inverter to the nominal AC power. As the total AC power again depends on the inverter efficiencies of both MPP inputs according to $P_{AC} = P_{DC,1} \cdot \eta_1 + P_{DC,2} \cdot \eta_2$, the model leads to a third-degree polynomial function and to four positive and four negative results. A further extension of the Schmidt-Sauer model is required for the case of two or more independent MPP trackers.

It can be concluded that for BIPV systems, the losses in the system DC power due to parallel connection have to be weighed against possible losses due to a lower inverter efficiency at lower DC power values, as inverters with a low minimum MPP voltage, combined with small efficiency losses, are not easy to find. For small BIPV systems, parallel connections may be the optimal solution, while for larger BIPV systems, the inverter efficiency will be at a high level, and inverters with several MPP input connections may be preferred, instead of parallel connections of PV module rows with different module orientations.

5 Conclusions and outlook

5.1 Summary of the results

In this PhD thesis, the simulation of the electricity yield of building-integrated PV systems has been discussed and implemented. First, the physical principles that are relevant for the electricity yield have been summarized. Compared to commercially available PV electricity yield simulation programs, the simulation of the irradiance has been extended with the help of a ray-tracing procedure. It has been shown that the angular definition of surrounding objects may lead to large deviations in the resulting irradiance on the module surface. With the ray-tracing procedure, not only surrounding objects, but also the ground albedo can be precisely simulated, including partial shading of the ground. The ray-tracing procedure also allows complex BIPV façades to be optically simulated.

For building-integrated PV systems, also the simulation of the temperature of the components of the PV system is an important issue. It has been shown that the linear temperature approach that is commonly applied for free-standing PV plants can lead to major deviations for the simulated temperature of the PV cells in a building-integrated photovoltaic system. For this reason, the layer structure of the BIPV modules, often consisting of several glass panes, has to be considered. A node model has been applied to simulate the temperature gradient in the BIPV modules, considering heat conduction, heat convection and thermal radiation.

For the purpose of accurate simulation of the consequences of inhomogeneous irradiance on the PV modules' surfaces, caused by shading or by different orientations of the PV modules, the I–V curve of every PV cell has been taken into consideration. To simulate the dependence of the I–V curve on the irradiance and temperature, the two-diode model as well as the detailed simulation of semiconductor devices with the software ASA have been applied. With the two-diode model, the I–V curves of PV cells based on mono- or polycrystalline silicon can be simulated with sufficient accuracy; for a PV cell based on amorphous silicon, it has been proven that the application of the two-diode model leads to large deviations from the results of the detailed semiconductor simulation performed with the software ASA.

With the I–V curves of all PV cells calculated, the I–V curves can be combined to a system I–V curve for every time step of the simulation. Combined with the simulation of the inverter that fixes the value of the system voltage, the operation points of all PV cells can be calculated for every time step. This offers the possibility to optimize the number of bypass diodes or blocking diodes installed in the system, to choose the optimal PV cell interconnection or to calculate the dependence of the electricity yield on the chosen inverter. With the system I–V curve available for every time step, the inverter efficiency can be easily calculated with the help of the Schmidt-Sauer model, and also the consequences of the limited MPP voltage range of the inverter to the electricity yield of the BIPV system can be calculated.

A detailed validation process has been performed to ensure the correctness of the simulation results. With the PV roof system in Bad Krozingen, the simulation of the consequences of partial shading to the PV electricity yield has been analyzed. The simulation of the DC power leads to an agreement with the measurements of $R^2 = 97.03\%$ for the unshaded and $R^2 = 97.98\%$ for the partially shaded PV subsystem. The second PV system that had been monitored over years, the BIPV system in the saw-tooth roof of the main building of Fraunhofer ISE, consists of PV modules based on polycrystalline silicon that unfortunately have degraded and do not correspond to the datasheet specifications anymore. Despite this error source, the simulated DC power still leads to an agreement with the measurements of $R^2 = 93.55\%$. With two further PV systems, other research topics have been covered. The PV system in Mochau/Dresden consists of PV modules based on amorphous silicon. With the DC power measurements of this PV system, the seasonal consequences of the metastability effect on the electricity yield were estimated by comparing the measurements with the simulation results of the DC power, leading to a sinusoidal curve fit. The electricity yield simulation was finally applied to calculate the consequences of connecting PV modules of different orientations in parallel. It was shown that even vertically installed PV modules of different cardinal directions can be connected to only one inverter with an acceptably low loss in the annual electricity yield.

5.2 Future research on the topic

Research on the electricity yield simulation of BIPV systems can be extended in the direction of improving the accuracy of the models presented in this PhD thesis or in the direction of accelerating or simplifying the simulation process. For the simulation of the irradiance, research may be necessary for the spectral distribution of incident light on vertical surfaces, as the results gained with the Perez sky distribution model and the ray-tracing procedure are not perfectly satisfying. The method of separating the simulation of the sky radiance distribution from the optical simulation of the geometrical configuration could be reanimated by applying other discretisation methods, maybe dependent on the cardinal direction of the BIPV system (if installed vertically). The simulation of the temperature of BIPV façades can certainly be improved by calculating the dependence of the external heat coefficient on the wind speed and wind direction, if these values are available from measurements. Furthermore, the simulation of the temperature of the PV cells can be extended to curtain walls where the simulation of the heat transfer coefficient from the BIPV module to the building is rather difficult. For PV modules based on thin-film technologies, research on diode models is desirable. This especially applies to the temperature dependence of the saturation currents. For PV technologies with metastable electrical properties, a diode model for the I–V curve at different metastability states would enable an electricity yield simulation of BIPV systems that includes seasonal variation. Also models for the long-term degradation of the I–V curve of PV modules would increase the accuracy of electricity yield simulations, not only for BIPV systems.

For a commercial application of the presented simulation method, the calculation speed has to be increased, either by simplified models or by general IT development. The statistical measures allow comparison of the current simulation method with simplified simulation procedures and help to decide whether the simplification leads to results of acceptable accuracy. They also allow comparison of the simulation method presented in this PhD thesis to other simulation approaches and programs that may arise in the future.

A Statistical measures

For the comparison of two time-dependent data arrays, like simulated and measured ones, statistical values are needed to quantify the degree of accordance between the two data sets. This appendix summarizes the statistical measures that have been applied in this thesis.

The coefficient of determination, abbreviated R^2, is the best-known statistical measure for quantifying the agreement between two data sets. It equals the square of Pearson's correlation coefficient; in other words, it indicates the quality of the simulation approach after fitting its parameters to measurement data with the Gaussian least-squares algorithm. It is defined by Eq. A.1.

$$R^2 = 1 - \frac{\sum_{i=1}^{N} (x_{sim}^i - x_{meas}^i)^2}{\sum_{i=1}^{N} (x_{meas}^i - \bar{x}_{meas})^2} \tag{A.1}$$

x_{sim}^i are the simulated, x_{meas}^i the measured values at time step i, and $\bar{x}_{meas}$ represents the mean value of the measured values over time. The numerator of the fraction is the residual sum of squares whereas the denominator represents the total sum of squares. R^2 is given in percent; 100% means perfect agreement of measured with simulated data, 0% means no agreement. For special cases, which are not important here, the R^2 value can even be negative. It has been observed that the R^2 value rarely indicates offsets, which is, in the context of this thesis, especially relevant for cable losses or spectral changes of the irradiance.

Although the coefficient of determination is the most frequently used measure to quantify the simulation performance, it is nevertheless important to evalulate more than this one statistical measure. Within this PhD thesis, the distribution of differences between simulation and measurement has been analyzed in more detail, which is done with the statistical measures *RSME* and *MBE*.

The root mean square error, abbreviated *RMSE*, corresponds to the standard deviation in the one-dimensional case, and can be calculated with Eq. A.2.

$$RMSE = \sqrt{\frac{1}{N} \sum_{i=1}^{N} (x_{sim}^i - x_{meas}^i)^2} \tag{A.2}$$

x_{sim}^i are the simulated, x_{meas}^i the measured values at time step i, while N is the number of points in time. The *RMSE* is given in the same units as the results and quantifies the standard deviation in the distribution of differences between simulated and measured values for the same time step.

The shift of the distribution of differences to the zero value is calculated with the mean bias error MBE, according to Eq. A.3.

$$MBE = \frac{1}{N} \cdot \sum_{i=1}^{N} (x_{sim}^{i} - x_{meas}^{i}) \tag{A.3}$$

Again, x_{sim}^{i} are the simulated, x_{meas}^{i} the measured values at time step i, while N is the number of points in time. The MBE is also given in the same units as the results. The MBE is valid for a clear evaluation of the offset in the simulation, where the R^2 is not sufficient. As the result can be either positive or negative, the MBE indicates whether the simulated values are too high or too low on average.

For the calculation of the statistical measures, it is important to define the data range. Within this PhD thesis, only the simulated and measured data during the day have been taken for evaluation. The presence of global irradiance ($> 5W/m^2$) has been chosen as the criterion for “during the day”. This rule has been retained for temperature simulations, meaning that the temperature simulation during the night are not included in the statistical investigation.

B List of symbols

B.1 Physical constants

h	Planck constant ($6.626 \cdot 10^{-34}$ m^{2}kg/s)
k_B	Boltzmann constant ($1.38 \cdot 10^{-23}$ J/K)
σ	Stefan-Boltzmann constant ($5.67 \cdot 10^{-8}$ Jm^{-2}s^{-1}K^{-4})

B.2 Physical quantities

A	absorptance
A	(module) surface area (m^2)
AM_0	air mass at sea level
AM_h	air mass at altitude h
a_R	Martin/Ruiz coefficient
a, b, c, d, e	Perez coefficients
b_0	incidence angle modifier constant (ASHRAE model)
C_{s1}	temperature coefficient for the reverse saturation current no.1
C_{s2}	temperature coefficient for the reverse saturation current no.2
d	distance (m)
d	(layer) thickness (m)
E	thermal radiation exchange parameter
E	irradiance (W/m^2)
E_{dir}	direct fraction of the irradiance on a surface (irradiance coming from a two degree cone around the sun) (W/m^2)
E_{glob}	total irradiance onto the module surface (W/m^2)
E_{diff}	difference between the global and the direct irradiance (W/m^2)
E_{eff}	effective irradiance (irradiance that has to impinge on the module surface to cause the same electrical behavior as under STC) (W/m^2)
E_{GP}	irradiance on a grid point (W/m^2)
E_a	annual energy total (e.g. kWh/m^2/a or kWh/a)
E_{spec}	total energy of a solar spectrum (J)
E_{FN}, E_{FP}	quasi-Fermi potentials (J)
f	contribution function of the sky region

f	focal length of the camera (m)
G	generation rate (s^{-1})
g_b, n_b, V_b	Bishop parameters (-, -, V)
h	heat transfer coefficient ($W/m^2/K$)
h	altitude (m)
H_R, H_T	haze factors
I	electric current (A)
I_s	reverse saturation current (A)
I_{ph}	photocurrent (A)
I_{sc}	short circuit current (A)
J	current density (A/m^2)
K	angular response
L	radiance ($W/m^2/sr$)
L_Z	radiance in zenith direction ($W/m^2/sr$)
MM_{spec}	spectral mismatch factor
MM_{el}	electrical mismatch
N	number of photons
$\tilde{n}$	refractive index
n	refractive index (real part)
n	density of negative charge carriers (m^{-3})
Nu	Nusselt number
NU	Non-uniformity of the irradiance
p	pixel of a rendered image
p	density of positive charge carriers (m^{-3})
p_{loss}, p_{self}, v_{loss}, r_{loss}	Schmidt-Sauer coefficients (W, -, V^{-1}, V^{-2})
P	power (W)
q	charge (Q)
$\dot{q}$	heat flux per surface area (W/m^2)
$\dot{q}_{abs}$	heat flux due to photon absorption (W/m^2)
$\dot{q}_{el}$	heat flux due to the electrical operation point of the PV cell (W/m^2)
$\dot{Q}$	heat flux (W)
r	distance of a pixel to the center of the image (m)
$\tilde{r}$, $\tilde{t}$	Fresnel coefficients
R	electrical resistance (Ω)
R	recombination rate (s^{-1})
R	reflectance
SR	spectral response
T	transmittance
T	temperature (K)
t	time (s)

TF	transfer function (sr) (see Eq. 3.3)
U	voltage (V)
V_T	thermal voltage (V) (see Eq. 2.19)
V_{oc}	open circuit voltage (V)
x	position (m)
α	absorption coefficient (m^{-1})
α	temperature coefficient for the short circuit current (%/K)
β	temperature coefficient for the open circuit voltage (%/K)
γ	temperature coefficient for the MPP power (%/K)
δ	phase of an electromagnetic wave
ε	relative permittivity (As/Vm)
ε	emissivity factor
η	mobility (m^2/Vs)
θ	zenith angle (=θ_Z) (angle measured from the sky zenith)
θ_H	elevation angle ($\theta_H = \pi/2 - \theta_Z$) *[avoided]*
θ_M	zenith angle in the module reference system (angle of incidence on the module)
θ_{GP}	incidence angle of the ray that reaches a grid point
θ_p	incidence angle of the radiation coming from a pixel of the image
κ	refractive index (imaginary part)
κ	linear factor of Eq. 2.35 (K m^2/W)
λ	heat conductivity (W/m/K)
λ	wavelength (m)
μ	mobility of charge carriers (m^2/(V·s))
ν	photon oscillation frequency (s^{-1})
ρ	charge density (m^{-3})
Φ_s, Φ_m	spectral distribution (standard, measured) (W/m^3)
Φ	radiant flux (W)
ϕ	azimuth angle ($S = 0°$, $W = 90°$)
ϕ_M	azimuth angle in the module reference system
ψ	electric potential (V)
Ω	solid angle (sr)

Curriculum vitae

Wendelin Sprenger was born in 1984 in Hall i.T., Austria. He studied physics at the universities of Innsbruck, Austria, and Freiburg i.B., Germany. After receiving his university degree in February 2009 with a Master's Thesis on ultracold Rydberg molecules, he started his PhD thesis at the Fraunhofer Institute of Solar Energy Systems (ISE). The research topic of the PhD thesis, the electricity yield simulation of complex BIPV systems, required the combination of many research topics. Most of them were covered at the institute. For the ray-tracing program RADIANCE, he improved the subprogram *gendaylit* for applications with meteorological data sets. However, to gain knowledge also in the challenges of modeling thin-film solar cells, he joined the PVMD group of the Delft University of Technology, where the well-established software program ASA was developed. Within the German Solarvalley BIPV project and the institute-internal research project on BIPV concepts, he was able to create a software program that is capable of calculating the time-dependent AC power of building-integrated photovoltaic systems. The program is currently being disseminated within the institute and can also be applied for the simulation of free-standing PV plants with partial shading. The simulation program is being used for research purposes in several follow-up projects on building-integrated photovoltaics.

Acknowledgments

The work presented in this PhD thesis has been partially funded by the German Federal Ministry of Education and Research within the research cluster Solarvalley Mitteldeutschland and partially by an internal research project of the Fraunhofer Institute for Solar Energy Systems in Freiburg i.B., Germany. The large number of researchers in the institute provided the ideal environment for the multidisciplinary topic of this PhD thesis. I would like to thank Tilmann Kuhn and Helen Rose Wilson for their excellent supervision on-site. Jan Wienold introduced me to the world of RADIANCE, shell programming and multi-core cluster simulations; contrary to all expectations, we finally managed to eliminate the errors in gendaylit. I profited a lot from the experience of the BIPV guru Christof Erban, who turned out to be the perfect discussion partner, especially for predictions of the PV cell's operation points. Merlin Mittelbach wrote an incredible number of Python programs with amazing features during his time as a research assistant; without his help, I would not have been able to extend the simulations of this PhD thesis to the system level. I would like to thank the whole group Solar Façades for the conductive working conditions. I thank Heribert Schmidt for his quick and comprehensive feedback on the simulation of the inverter efficiency. Many thanks to Nils Reich who organized a simulation competition for the partially shaded PV rooftop system in Bad Krozingen; the resulting discussions with Thomas Reis and Anton Driesse have been very helpful.

The institute provides clustered scientific knowledge, which necessarily makes these acknowlegments incomplete.

For the simulation of the I–V curves of solar cells based on thin-film PV technologies, it was necessary to look beyond the Institute. The reputation of the ASA program lead to a cooperation with the PVMD group of TU Delft. I would like to thank prof.dr. Miro Zeman for supervising my PhD thesis despite the large distance and the rather small overlap of the research fields. Rudi Santbergen and Serge Solntsev were always open to answer questions, of which I had many; I hope the questions were of help for the further development of the ASA program. Many thanks also to Klaus Jaeger and Jimmy Melskens for the long and interesting discussions we had. Finally, I would like to thank all the members of the defence committee for their time to review the PhD thesis.

The research projects allowed cooperation with many external scientists. I especially would like to thank Markus Muench from the company Solarion and Meinhard Stalder from the company SMA for sharing their experiences. I also thank Juergen Huepkes and Bart Pieters for the discussions we had in the SOPHIA project. Last but not least, I would like to thank Helen Rose Wilson additionally for proofreading the English.

Bibliography

[1] A. Angstrom. “The Albedo of Various Surfaces of Ground”. In: *Geografiska Annaler* 7 (1925), pp. 323–342.

[2] A. Appel. “Some techniques for shading machine renderings of solids”. In: *AFIPS Spring joint computer conference*. Atlantic City, 1968.

[3] *ASA (Advanced Semiconductor Analysis)*. http://ewi.tudelft.nl/en/the-faculty/departments/electrical-sustainable-energy/photovoltaic-materials-and-devices/asa-software/.

[4] R. Bird and C. Riordan. “Simple solar spectral model for direct and diffuse irradiance on horizontal and tilted planes at the earth’s surface for cloudless atmospheres”. In: *J. Climate Appl. Meteor.* 25 (1986), pp. 87–97.

[5] J.W. Bishop. “Computer simulation of the effects of electrical mismatches in photovoltaic cell interconnection circuits”. In: *Solar Cells* 25.1 (1988), pp. 73–89.

[6] M. Born and E. Wolf. *Principles of Optics*. 7th ed. Cambridge: Cambridge University Press, 1999.

[7] A.P. Brunger and F.C. Hooper. “Anisotropic sky radiance model based on narrow field of view measurements of shortwave radiance”. In: *Solar Energy* 51.1 (1993), pp. 53–64.

[8] *Concerted Action: Energy Performance of Buildings.* www.epdb-ca.eu.

[9] *Cost-Effective – Convert facades into multifunctional, energy gaining components*. http://www.cost-effective-renewables.eu/.

[10] *Daysim – Advanced Daylight Simulation Software*. www.daysim.com.

[11] J.A. Duffie and W.A. Beckman. *Solar engineering of thermal processes*. New York: Wiley, 1991.

[12] D. G. Erbs, S. A. Klein, and J. A. Duffie. “Estimation of the diffuse radiation fraction for hourly, daily and monthly-average global radiation”. In: *Solar Energy* 28.4 (1982), pp. 293–302.

[13] L. Fanni et al. “Investigation of annealing and degradation effects on a-Si PV modules in real operating conditions”. In: *24th EU-PVSEC*. Hamburg, 2009.

[14] F. Fertig et al. “Impact of Junction Breakdown in Multi-Crystalline Silicon Solar Cells on Hot Spot Formation and Module Performance”. In: *26th EU-PVSEC*. Hamburg, 2011.

[15] F. Frontini. “Daylight and solar control in buildings”. PhD thesis. Politecnico di Milano 2011.

[16] F. Frontini, T.E. Kuhn, and W. Sprenger. “Eine neue winkelselektiv-teiltransparente BIPV-Fassadenkonstruktion”. In: *Gebäudeintegrierte Photovoltaik (OTTI)*.
Bad Staffelstein, 2011.

[17] *GeoModel Solar*. www.geomodelsolar.eu.

[18] R.A. Goldstein and R. Nagel. “3-D Visual simulation”. In: *SIMULATION* 16.1 (1971), pp. 25–31.

[19] M. Gostein and L. Dunn. “Light Soaking Effects on Photovoltaic Modules: Overview and Literature Review”. In: *37th IEEE PVSC*. Seattle, 2011.

[20] M.A. Green. *Solar Cells*. University of New South Wales, 1982.

[21] *Guardian SunGuard*. www.sunguardglass.com.

[22] C. Gueymard. “Parameterized transmittance model for direct beam and circumsolar spectral irradiance”. In: *Solar Energy* 71.5 (2001), pp. 325–346.

[23] J. E. Hay and D.C. McKay. “Estimating Solar Irradiance on Inclined Surfaces: A Review and Assessment of Methodologies”. In: *International Journal of Solar Energy* 3.4-5 (1985), pp. 203–240.

[24] E. Hecht. *Optik*. München: Oldenbourg, 2001.

[25] N. Igawa et al. “Models of sky radiance distribution and sky luminance distribution”. In: *Solar Energy* 77.2 (2004), pp. 137–157.

[26] A. Jacobs. *Understanding rtcontrib*. http://www.jaloxa.eu/resources/radiance/documentation/docs/rtcontrib_lesson.pdf.

[27] F. Kasten and A.T. Young. “Revised optical air mass tables and approximation formula”. In: *Appl. Opt.* 28.22 (1989), pp. 4735–4738.

[28] R. Kind. “Dark Current Characteristics of Amorphous Silicon Solar Cells”. Master thesis. TU Delft 2010.

[29] D. L. King, J. A. Kratochvil, and W. E. Boyson. “Measuring solar spectral and angle-of-incidence effects on photovoltaic modules and solar irradiance sensors”. In: *26th IEEE PVSC*. New York, 1997.

[30] S.A. Klein and J. C. Theilacker. “An Algorithm for Calculating Monthly-Average Radiation on Inclined Surfaces”. In: *Journal of Solar Energy Engineering* 103.1 (1981), pp. 29–33.

[31] A.M. Kovach. “Effect of Partial Shading on the Energy Performance of Photovoltaic Arrays Integrated onto Buildings”. PhD thesis. Düsseldorf 1995.

[32] W. Kwapil. “Alternative materials for crystalline silicon solar cells - Risks and implications”. PhD thesis. Konstanz 2010.

[33] G.W. Larson and R.A. Shakespeare. *Rendering with RADIANCE*. San Francisco: Morgan Kaufmann Publishers, 1998.

[34] H. Laukamp. *Die PV-Anlagen am Neubau Fraunhofer ISE. Beschreibung des elektrischen Aufbaus (Implementation report)*. Freiburg i.B., 2002.

[35] B.Y.H Liu and R.C. Jordan. "A rational procedure for predicting the long-term average performance of flat-plate solar-energy collectors". In: *Solar Energy* 7 (1963), pp. 53–74.

[36] N. Martin and J.M. Ruiz. "Calculation of the PV modules angular losses under field conditions by means of an analytical model". In: *Solar Energy Materials and Solar Cells* 70.1 (2001), pp. 25–38.

[37] *Meteonorm Software*. www.meteonorm.com.

[38] H. Müllejans et al. "Spectral mismatch in calibration of photovoltaic reference devices by global sunlight method". In: *Measurement Science and Technology* 16.6 (2005), p. 1250.

[39] D.R. Myers and C.A. Gueymard. "Description and availability of the SMARTS spectral model for photovoltaic applications". In: *SPIE*. Glasgow, 2004.

[40] R. Perez, R. Seals, and J. Michalsky. "All-weather model for sky luminance distribution. Preliminary configuration and validation". In: *Solar Energy* 50.3 (1993), pp. 235–245.

[41] R. Perez et al. "A new simplified version of the perez diffuse irradiance model for tilted surfaces". In: *Solar Energy* 39.3 (1987), pp. 221–231.

[42] I. Pola, D. Chianese, and A. Bernasconi. "Flat roof integration of a-Si triple junction modules laminated together with flexible polyolefin membranes". In: *Solar Energy* 81.9 (2007), pp. 1144–1158.

[43] R. Preu. "Der Einfluss der Strahlungsdichteverteilung und der optischen Eigenschaften der Kapselung photovoltaischer Module auf den Jahreswirkungsgrad der Energiekonversion." PhD thesis. Freiburg i.B. 1995.

[44] D. Prukop. "Zur Modellierung großflächiger Photovoltaik-Generatoren". PhD thesis. Aachen 1997.

[45] *PVSOL Expert (from Valentin Software)*. http://www.valentin.de/.

[46] *PVsyst: Software for Photovoltaic Systems*. www.pvsyst.com.

[47] V. Quaschning. "Simulation der Abschattungsverluste bei solarelektrischen Systemen". PhD thesis. Berlin 1996.

[48] V. Quaschning and R. Hanitsch. "Influence of shading on electrical parameters of solar cells". In: *25th IEEE PVSC*. Washington, 1996.

[49] *RADIANCE synthetic imaging system*. http://radsite.lbl.gov/radiance/.

[50] R.Kind et al. “Thermal ideality factor of hydrogenated amorphous silicon p-i-n solar cells”. In: *Appl. Phys.* 110 (2011).

[51] *Samyn and Partners, Architects and Engineers*. www.samynandpartners.be.

[52] *Satel-Light – The European Database of Daylight and Solar Radiation. Based on Meteosat.* http://www.satel-light.com.

[53] E.U. Schlünder. *Einführung in die Wärmeübertragung*. Braunschweig / Wiesbaden: Vieweg, 1981.

[54] H. Schmidt. “Von der Solarzelle zum Solargenerator”. In: *OTTI Photovoltaikanlagen*. Freiburg i.B., 1994.

[55] H. Schmidt and D.U. Sauer. “Praxisgerechte Modellierung und Abschätzung von Wechselrichter-Wirkungsgraden”. In: *Sonnenenergie* 11 (1995).

[56] H. Schmidt et al. “Modellierung der Spannungsabhängigkeit des Wechselrichterwirkungsgrades”. In: *23. Symposium Photovoltaische Energieversorgung*. Bad Staffelstein, 2008.

[57] A. Skartveit and J. A. Olseth. “The probability density and autocorrelation of short-term global and beam irradiance”. In: *Solar Energy* 49.6 (1992), pp. 477–487.

[58] *SMARTS – Simple Model of the Atmospheric Radiative Transfer of Sunshine*. http://www.nrel.gov/rredc/smarts/.

[59] *SolarOr*. www.solaror.com.

[60] D. L. Staebler and C. R. Wronski. “Reversible conductivity changes in discharge-produced amorphous Si”. In: *Applied Physics Letters* 31.4 (1977), pp. 292–294.

[61] *The RAL colour standard*. www.ral-farben.de.

[62] P.R. Tregenza and I.M. Waters. “Daylight coefficients”. In: *Lighting Research and Technology* 15.2 (1983), pp. 65–71.

[63] A. Virtuani and L. Fanni. “Seasonal power fluctuations of amorphous silicon thin-film solar modules: distinguishing between different contributions”. In: *Progress in Photovoltaics: Research and Applications* (2012).

[64] A. Wagner. *Photovoltaik Engineering: Handbuch für Planung, Entwicklung und Anwendung*. Berlin: Springer, 2009.

[65] P. Wuerfel. *Physics of Solar Cells*. Weinheim: WILEY-VCH Verlag, 2009.

[66] M. Zeman and J. Krc. “Optical and electrical modeling of thin-film silicon solar cells”. In: *Journal of Materials Research* 23.4 (2008), p. 10.

[67] M. Zeman et al. *Advanced Semiconductor Analysis. Opto-electronic simulator for amorphous and crystalline semiconductor devices*. Vol. 5.3. Delft University of Technology, 2012.